DOE/ER/12900--T2

EXPERIMENTAL OBSERVATIONS OF THE BREAKUP OF MULTIPLE METAL JETS IN A VOLATILE LIQUID

BY

MICHAEL JAMES MARCINIAK

B.S., Milwaukee School of Engineering, 1990

THESIS

Submitted in partial fulfillment of the requirements
for the degree of Master of Science in Nuclear Engineering
in the Graduate College of the
University of Illinois at Urbana-Champaign, 1993

Urbana, Illinois

DISCLAIMER

Portions of this document may be illegible in electronic image products. Images are produced from the best available original document.

UNIVERSITY OF ILLINOIS AT URBANA-CHAMPAIGN

THE GRADUATE COLLEGE

JANUARY 1993

WE HEREBY RECOMMEND THAT THE THESIS BY

MICHAEL JAMES MARCINIAK

ENTITLED EXPERIMENTAL OBSERVATIONS OF THE BREAKUP OF MULTIPLE METAL JETS IN A VOLATILE LIQUID

BE ACCEPTED IN PARTIAL FULFILLMENT OF THE REQUIREMENTS FOR THE DEGREE OF MASTER OF SCIENCE

Barclay G. Jones
Director of Thesis Research

Barclay G. Jones
Head of Department

Committee on Final Examination†

Chairperson

Thomas J Hanratty

† Required for doctor's degree but not for master's.

O-517

ACKNOWLEDGEMENTS

This project was supported by DOE contract DE-FG07-89ER12900, and was conducted in cooperation with Dr. B. W. Spencer, Manager, Engineering Development Laboratories, Reactor Engineering Division, Argonne National Laboratory (ANL). Laboratory space, equipment, and technical assistance were provided by ANL.

Much appreciation is extended to J. P. Schneider for his considerable guidance and support throughout this project.

The academic advisor for this project was Dr. B. G. Jones, whose support is gratefully acknowledged.

TABLE OF CONTENTS

1. INTRODUCTION 1

1.1 Motivation 1

1.2 Objective 5

2. LITERATURE REVIEW 6

2.1 Isothermal Jets 6
2.1.1 Turbulent Regime 7

2.2 Boiling Jet Breakup 8
2.2.1 Prototype Experiments 9
2.2.2 Simulant Experiments 10

3. EXPERIMENTAL INVESTIGATION 12

3.1 Experimental Apparatus 12
3.1.1 Components 12
3.1.2 Instrumentation 17
3.1.3 Data Acquisition Equipment 17
3.1.4 Simulant Materials 19

3.2 Experimental Procedure 20
3.2.1 Control Systems 21

3.3 Experimental Data 23
3.3.1 Test Matrix 23
3.3.2 Pre-Melt Injection Data 25
3.3.3 Melt Injection Data 27

4. DATA ANALYSIS 34

4.1 Test Matrix Review 34

4.2 Experimental Observations 35
4.2.1 Motion Picture 35
4.2.2 Radiograph 36
4.2.3 Oscillograph Trace 39

4.3 Data Reduction 40
4.3.1 Breakup Length 40
4.3.2 Melt Streams 41
4.3.3 Vapor Generation 45

5. RESULTS 49

5.1 Discussion 54

6. SUMMARY 57

7. RECOMMENDATIONS FOR FURTHER WORK 58

REFERENCES 59

APPENDIX

A. Design Specification for Furnace/Pour Assembly 61
B. Experimental Procedure Checklist 70
C. Oscillograph Traces 78
D. Selected Frames from High Speed Motion Picture Films 96
E. Selected Radiographs 111
F. Hycam #1 Films Data Reduction 119

LIST OF TABLES

Table 3-1: Relevant Properties of Simulant Materials used in MFSBS-MJ Experiments [20, 21] 19

Table 3-2: MFSBS-MJ Experimental Test Matrix Including Development Details 24

Table 3-3: Pre-Test Apparatus Data from MFSBS-MJ Experiments 28

Table 3-4: Pre-Melt Injection Data from MFSBS-MJ Experiments 29

Table 4-1: MFSBS-MJ Dimensional Breakup Length Estimates (cm) and Time to Breakup from Coolant Surface 42

Table 4-2: Melt Stream Velocity and Diameter at Coolant Surface for MFSBS-MJ Experiments 46

Table 4-3: Melt Energy Distribution in MFSBS-MJ Experiments 48

LIST OF FIGURES

Figure 1-1: Babcock and Wilcox Pressurized Water Reactor (1970), Oconee Nuclear Power Station [1] 2
Figure 3-1: Photograph of MFSBS-MJ Experimental Apparatus 13
Figure 3-2: Schematic Diagram of Experimental Apparatus 14
Figure 3-3: Photograph of Multiple Jet Piping System (3.8 cm Spacing; 0.64 cm Diameter Nozzles) 16
Figure 3-4: Schematic Diagram of X-Ray Flash System 18
Figure 3-5: Schematic Diagram of Apparatus Control Systems 22
Figure 3-6: Photocopy Reproduction of High Quality Radiograph (from MFSBS-MJ17) 26
Figure 3-7: Sample Oscillograph Trace (from MFSBS-MJ4) 31
Figure 3-8: Selected Frames from Hycam #1 Film (from MFSBS-MJ16) . . . 32
Figure 4-1: Sketch of an Idealized Molten Metal Jet Breakup in a Volatile Liquid [10] 37
Figure 4-2: Multiple Jet Leading Edge Penetration vs. Time (from MFSBS-MJ1) 43
Figure 4-3: Multiple Jet Leading Edge Penetration Velocity vs. Penetration Depth (from MFSBS-MJ1) 44
Figure 5-1: MFSBS-MJ Breakup Length Data 50
Figure 5-2: Geometric Spacing Influence on MFSBS-MJ Breakup Lengths 51
Figure 5-3: MFSBS-MJ Test Data Identification 52
Figure 5-4: Proportionality Constant for MFSBS-MJ Data Fit to Saito Correlation 53

1. INTRODUCTION

A postulated severe loss of coolant accident in a nuclear reactor can lead to significant core damage due to residual heat generation. Subsequently, melted core materials (i.e.; corium) could migrate downward and impinge upon the lower head of the reactor pressure vessel (RPV). During this relocation, the complexity of the reactor structure could segregate the molten corium into various flow paths. A perforated flow plate (e.g.; see Figure 1-1) could readily provide the mechanism to segregate the molten corium. The resulting small (a few cm) diameter melt streams, driven by gravity, could then penetrate the remaining coolant in the RPV and cause any of the following events: impingement of the high temperature melt streams on the lower head could breach the RPV [see Reference 2]; re-agglomeration of the corium melt on the lower head could influence the coolability of the debris bed [3]; 'pre-mixing' of the melt streams with the coolant could lead to a vapor explosion [4, 5]; or, sufficient quenching of the melt streams by the coolant could produce a stabilized debris bed. An overview of the thermo-science issues related to core-melt accidents is presented by Theofanous [6]. Thus, insight into the melt stream breakup mechanisms (i.e.; interfacial conditions, fragmentation, and geometric spacing) during the melt-coolant interactions is necessary to evaluate the plausibility, and characteristics, of these events.

1.1 Motivation

The present experimental investigation was motivated by the recent Molten Fuel Stream Breakup Simulation (MFSBS) experiments conducted by Schneider at Argonne National Laboratory (ANL) [7], and the uncertainty in the influence of multiple jet configurations on the breakup mechanisms of corium-water interactions as briefly discussed in [8].

In the MFSBS experiments, simulant materials were used to determine a 'boiling' jet breakup length correlation and to visualize the melt fragmentation mechanisms during the penetration of a

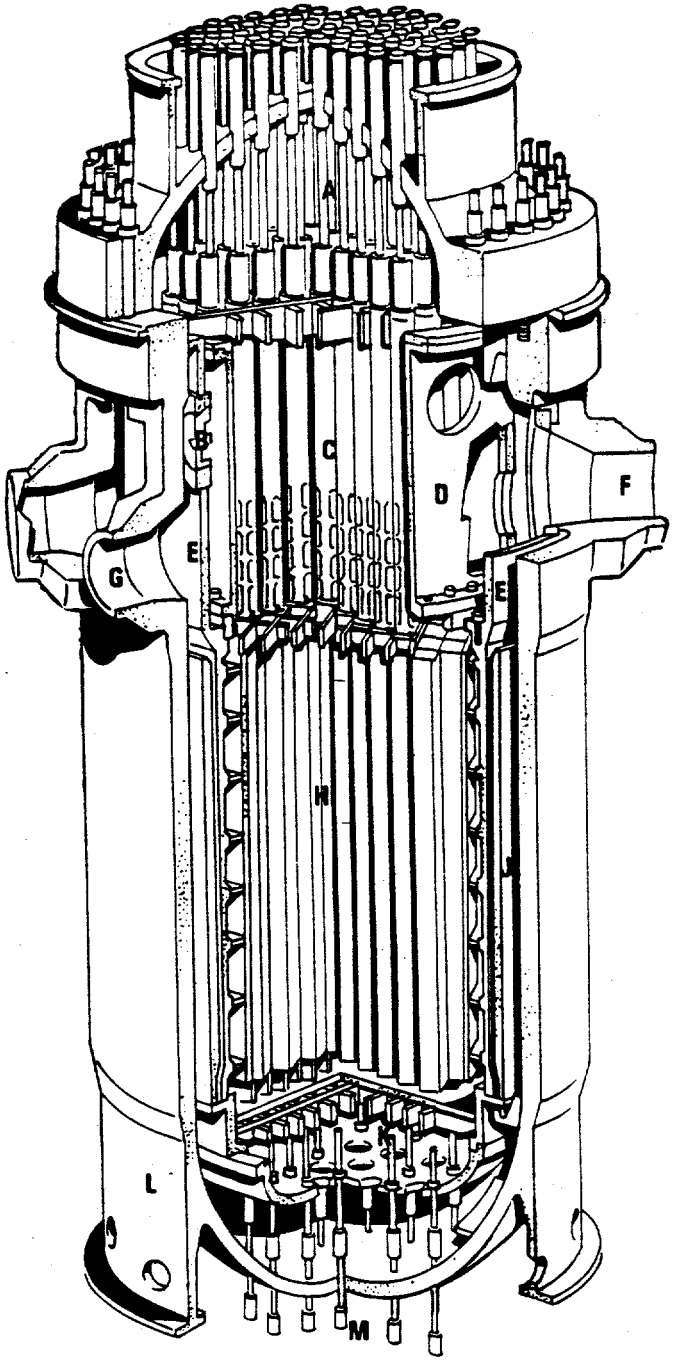

Key to reactor

A. Control rod drive actuators
B. Internals vent valve
C. Control rod guide tubes
D. Upper plenum
E. Core support shield
F. Outlet nozzle
G. Inlet nozzle
H. Fuel assembly
J. Thermal shield
K. Flow baffle
L. Support skirt
M. In-core instrumentation nozzles

Figure 1-1: Babcock and Wilcox Pressurized Water Reactor (1970), Oconee Nuclear Power Station [1]

single molten metal jet into a volatile liquid. Here, the term 'boiling' described the interfacial condition between the melt and the coolant (i.e.; vapor is generated upon leading edge interaction and the jet column is essentially penetrating a vapor counterflow). The goal was to characterize the hydrodynamics of the corium-water interactions in a postulated core melt accident. Motivation for this came from the absence of a relevant, conclusive database for molten metal-coolant interactions and from the experimental investigation by Saito et. al. [9], where a very well correlated expression for 'penetration length' was given for materials of similar densities (see Section 2.2.2). The extreme accuracy of the correlation to the experimental data provided motivation to investigate its applicability to other simulant materials (i.e.; Cerrobend metal and Freon 11), whose density ratio more closely approximated that of reactor materials, to provide insight into the jet breakup mechanisms (i.e.; breakup length, fragmentation, debris) of postulated severe core melt accidents.

The MFSBS data fit the correlation by Saito well and Schneider proposed a physical model to explain the 'boiling' jet breakup correlation [10]. The breakup length was defined by the steady state depth at which all the segments/drops from a dense, inviscid jet have acquired some radial momentum (i.e.; are diverging from the jet axis). The model assumed that the force exerted by the counter-axial vapor flow on the jet column/segments be equal to the weight of the coolant displaced. Basic conservation laws were used along with this assumption to derive a 'boiling' breakup length expression for an ideal jet penetrating a vapor flow under a hydrostatic pressure gradient:

$$\frac{L}{D_0} = \frac{Fr}{2}\left(\left(\frac{1}{\beta}+1\right)^{\frac{8}{5}}-1\right) \qquad (1)$$

where

$$\beta = \frac{2}{5}\sqrt{\frac{Fr}{\rho_j/\rho_l}} \qquad (2)$$

Neglecting gravitational acceleration of the fragmenting jet, the breakup length model reduced to:

$$\frac{L}{D_0} = 2\sqrt{\frac{\rho_j}{\rho_l} Fr} \qquad (3)$$

This relation is essentially that determined empirically by Saito et. al. (see Section 2.2.2). A fundamental idea underlying this model was that the vapor flow is driven by the displacement of the coolant, and the force exerted on the jet is equal to the weight it displaces. If the boundary layer due to shear is thin (compared to the jet diameter), then the jet column approximately displaces its own volume [7]. This model implied that the 'boiling' jet breakup length of a single jet should be negligibly influenced by the simultaneous penetration of adjacent jets in the presence of a continuous column of coolant. The uncertainty in the influence of the multiple jet configurations on the breakup mechanisms is evident in the currently available computer models that simulate corium melt stream penetrations into water for the purpose of predicting the onset of a steam explosion in a reactor vessel. A brief review of these models is presented by Fletcher and Thyagaraja [11]. Each model considers jet penetration and fragmentation uniquely, including complete omission of the fragmentation process, a jet modelled as spherical drops dispersed under saturated conditions, jet fragmentation by leading edge Rayleigh-Taylor instability theory, and jet leading edge penetration by the formation of a ball-vortex with stripping from the jet column due to Kelvin-Helmholtz instability. These competing jet fragmentation theories and the uncertainty in multiple jet effects are possibly due to the lack of applicable experimental observations.

The extension of the MFSBS experiments to include multiple jet penetration into a volatile liquid was motivated by several objectives: (1) to test the implications of the model proposed by Schneider [10] describing the physical basis of the Saito correlation; (2) to assess the geometric spacing parameter thought to influence the boiling jet breakup length; (3) to produce relevant

experimental data for the advancement of computer modelling of molten corium migration during postulated core melt accidents.

1.2 Objective

The objective of the present experimental investigation is to determine the influence of adjacent jets on the breakup length of a central jet in a one-dimensional array of molten metal jets simultaneously penetrating a volatile liquid. This will be accomplished by performing a matrix of tests encompassing a range of nozzle spacing-to-diameter (i.e.; aspect) ratios. Data on the melt-coolant interactions will be generated by motion picture photography and flash radiography. The data will be reduced for comparison to the 'boiling' jet breakup model by Saito et.al. [9], and for verification of the physical model proposed by Schneider [10]. Also, a relation between the geometric spacing ratio and the jet breakup length will be investigated to determine the influence of the multiple jet configurations.

The present experimental investigation closely follows the procedure established in [7] and differs primarily by the use of a multiple jet piping system in lieu of a single nozzle. The same simulant materials, slightly modified test apparatus and procedure, and the same data acquisition equipment are used to ensure compatibility to the MFSBS experiments. The similarity to the MFSBS experiments qualifies the use of the acronym MFSBS-MJ (Molten Fuel Stream Breakup Simulation - Multiple Jet) in the present experimental investigation.

2. LITERATURE REVIEW

During a core melt accident, it is anticipated that the molten corium will be segregated into small diameter streams during its migration to the lower plenum. A review of the literature revealed no work dedicated to the geometric spacing effects on jet breakup. To provide base information, a review of the relevant literature was done on current experimental work applicable to predicting the jet breakup mechanisms for the molten corium-water interactions.

2.1 Isothermal Jets

A comprehensive review of the literature was done by Ginsberg [12] to characterize liquid jet breakup mechanisms and to determine their implications on molten corium-water interactions. In this study, the jet breakup mechanisms were categorized into four regimes; Rayleigh, transition, turbulent, and atomization, and the breakup length was described as the distance downstream at which continuity was lost. A plot of normalized breakup length vs. ambient Weber number (We_a) was developed to ascertain the trends in each regime. The data analyzed was for liquid jets issuing into stagnant, or constant velocity, gas (i.e.; air).

The Rayleigh regime was characterized by a low velocity jet ($We_a < 1$) that grew axisymmetric, varicose deformations due to capillary instability. For a low viscosity fluid, Weber modeled the breakup length in this regime as:

$$\frac{L}{d} = C\left(\sqrt{We_j} + 3\frac{We_j}{Re_j}\right) \qquad (4)$$

where the constant has been approximated by Grant [13] as 12 to 13.

In the transition regime ($We_a \sim 1$), the breakup mechanisms were characterized by the Rayleigh regime with the effects of higher jet velocities, or jet-gas relative velocities, increasing the rate of the instability growth, thereby decreasing the breakup length.

The flow in the turbulent regime ($We_a \gg 1$) was characterized by stripping of droplets from the surface of a coherent jet and the growth of large scale helical, or sinuous, waves, whose crests erode by the ejection of small droplets. Further review of this regime is discussed below.

The atomization regime ($We_a > 100$) was characterized by a spraying phenomenon, resulting from the ejection of droplets from the surface of the jet, possibly in the presence of a liquid core region. Since atomization has only been observed using very small (< 1 mm) diameter nozzles, nozzle geometry may possibly influence this result (e.g.; via cavitation). An expression for the breakup length of an atomizing jet was derived by Taylor [14]:

$$\frac{L}{d} = B\sqrt{\frac{\rho_j}{\rho_a}} \qquad (5)$$

The experimental data reviewed by Ginsberg indicated that the range of B was 3.3 - 15.8.

Ginsberg assumed that the We_a would be high for corium penetration of water, due to high velocity steam counterflow, and predicted that breakup would be in the atomization regime. Taylor's jet breakup expression (Eqn. 5) was used with B equal to 3.3 and reactor material properties to estimate the breakup length of corium in water under postulated reactor conditions as over 100 jet diameters. However, Schneider [7] has noted that Eqn. 5 is applicable only for a jet issuing into a stagnant fluid.

2.1.1 Turbulent Regime

In the present investigation, the melt streams are characterized by high relative velocities ($We_a \gg 1$) and large diameters ($\gg$ 1 mm), which probably discards breakup mechanisms described in the extreme flow regimes (i.e.; Rayleigh and atomization). Therefore, further characterization of the turbulent flow regime was deemed necessary to the present experimental investigation.

Hoyt and Taylor [15] provided excellent visualization of the breakup mechanisms for isothermal high speed (i.e.; beyond the Rayleigh and transition regimes) jets issuing into stagnant, co-axial, and counter-axial air. Axisymmetric instabilities culminated in the ejection of spray droplets near the origin of the jet. Further downstream, this seemed to diminish and long wavelength helical instabilities propagated. The effects of co- or counter- axial air flow about the jets suppressed or increased the growth rate of the helical instabilities, respectively. Ultimately, the breakup appeared to be due to aerodynamic form drag on the helical segments of the jet.

De Jarlais, Ishii, and Linehan [16] conducted experiments on breakup of isothermal water jets in the presence of a confined co-axial annular air flow. 'Roll wave entrainment' was initially observed at relatively high speed flows on the crests of the sinuous waves, and at higher velocities appeared to cause jet breakup. The jet breakup length was correlated by:

$$\frac{L_B}{D_j} = 685\,(Re_j)^{-0.53}\sqrt{We_j}\left(\frac{We_{G,rel}}{\alpha^2}\right)^{-0.645} \qquad (6)$$

Interestingly, the quantity in brackets is roughly the ambient We and the product of the last two quantities form an expression similar to that of Taylor (see Eqn. 5) when the gas is stagnant. The dependence on Re was apparently due to the jet turbulence [7], since it was also observed for Rayleigh breakup.

2.2 Boiling Jet Breakup

The phenomenon of molten corium jet breakup in water differs from the isothermal jet studies since boiling of the continuous phase causes an unknown and non-constant velocity of the counter-axial vapor flow under a constant pressure gradient, which prevents the direct application of breakup length relations having relative velocity as an independent variable [10].

Epstein and Fauske [17] did a linear Kelvin-Helmholtz instability analysis on a two-interface

plane geometry (i.e.; corium/steam and steam/water) and developed the following expression for jet breakup length:

$$\frac{L}{d} = \frac{\sqrt{3}}{2}\left(1+\frac{\rho_s}{\rho_j}\right)\sqrt{\frac{\rho_j}{\rho_s}} \qquad (7)$$

They concluded that the vapor column encompassing the corium would be large enough to preclude any influence of the water on the corium breakup.

2.2.1 Prototype Experiments

In the Corium Water Thermal Interaction (CWTI) experiments conducted at ANL [18], thermite corium (UO_2-ZrO_2-Steel) was used to investigate ex-vessel corium ejection into the reactor cavity, and subsequent blowdown, for various conditions in a scaled model of the Zion plant containment. Of particular interest was CWTI-9 and -10 where a single corium jet ($\sim$ 2 cm dia.) was injected into a saturated water pool ($\sim$ 30 cm deep) at an initial rate of about 9.5 m/s. Observations from CWTI-9 indicated that large vapor generation occurred, and the jet breakup was largely incomplete. In CWTI-10, highly subcooled water was used and no vapor generation occurred during the corium injection. The jet breakup was incomplete.

In the Corium-Coolant Mixing (CCM) experiments conducted at ANL [8], similar apparatus and materials were used to investigate the pour stream mixing modes of corium into water under reactor conditions. The penetration rates were estimated in each test by responses from thermocouples located along the axis of the penetrating melt stream, and the breakup lengths were measured as the location at which the penetration rate decreased significantly. In CCM-2, multiple melt streams produced a strong steam crossflow as indicated by the deflection of the streams, and, from debris bed observations, it appeared that the corium quench was limited during the pour. Pool

swell, recorded in two CCM tests, indicated that a significant vapor annulus developed about the jet [7]. The CCM breakup lengths were much less than that predicted by breakup correlations given by Epstein and Fauske (Eqn. 7) and Saito et. al. [9]. Insufficient melt mass in the CCM experiments may have prevented the achievement of a quasi-steady state, which is necessary to estimate the breakup length. It was concluded that the most important parameters affecting the corium stream breakup were geometry (i.e.; single jet vs. multiple jet) and water subcooling.

2.2.2 Simulant Experiments

The difficulty in handling prototypic materials has limited the development of jet breakup mechanisms related to core melt interactions. The use of simulant materials provides a more tractable means to achieve these goals.

The Jet Coolant (JC) experiments performed at ANL [19] considered the penetration of large diameter pour streams of molten Wood's metal and tin into subcooled and saturated water. Variations in the melt temperature and the degree of subcooling allowed for liquid-liquid (no boiling) penetration, nucleate boiling penetration, and sustained film boiling penetration. Detailed observations of the jet breakup mechanisms were given. The breakup lengths in several of the JC tests were determined from leading edge penetration rates and compared to various models previously developed. It was concluded that the non-boiling penetration was in reasonable agreement with Taylor's model (Eqn. 5). Tests involving steam generation showed that interfacial boiling strongly affects breakup; breakup lengths for transition or film boiling jet penetration were more than twice that for non-boiling penetration.

Saito, Sato, and Imahori [9] conducted experiments on the penetration of hot water jets into ambient Freon 11, and liquid nitrogen, to characterize penetration length, which was defined as the length of the vapor chimney (taken from high speed video), and interpreted as the depth where the

jet had lost all axial momentum. For tests with liquid nitrogen, the water jets were at room temperature. Large diameter opaque vapor chimneys were generated and, due to the comparable densities of the interacting materials, the jet fluid was always entrained in the counter-axial vapor flow. Thus, a 'penetration length' was observed as the steady state depth sustained by the jet. The experimental results were correlated very well by:

$$\frac{L}{D_j} = 2.1\sqrt{\frac{\rho_j}{\rho_c} Fr} \tag{8}$$

where

$$Fr = \frac{V_j^2}{gD_j} \tag{9}$$

It was noted that two breakup lengths recorded by Spencer et. al. [8] (for Wood's metal and water) were well predicted by this correlation.

3. EXPERIMENTAL INVESTIGATION

The experimental work conducted in the present investigation involved the use of the test apparatus and procedure previously developed in the MFSBS experiments [7]. Modifications were incorporated to advance the test apparatus and procedure to encompass multiple jet experimentation. A photograph of the multiple jet experimental apparatus is shown in Figure 3-1. In the present section, a detailed description of the experimental apparatus and the test procedure is given. This is followed by the development of the test matrix and a presentation of the experimental data.

3.1 Experimental Apparatus

In the present section, the apparatus components, instrumentation, and data acquisition equipment are reviewed. A schematic diagram of the multiple jet experimental apparatus, depicting the components and instrumentation locations, is shown in Figure 3-2.

3.1.1 Components

The primary components of the apparatus were the melt furnace, the interaction vessel, the multiple jet piping system, the cutter assembly, and the condenser.

A detailed design of the melt furnaces is included in Appendix A. The volume capacity of the lower furnace was 0.8 liters, which held 7.5 kg of liquid Cerrobend metal. The bottom flange of this furnace was countersunk to accept a 2-3 mil metal shim stock diaphragm. The volume capacity of the upper furnace was 2.9 liters. The spool section of each furnace was wrapped with tubular heater element(s) (Omega TSSM-70) and secured by Omegabond 400 electrically resistive cement. A layer of Wetpak thermal insulation was formed around each furnace. Each furnace was fed by a separate 110 Vac Variac controlled power circuit.

The interaction vessel was unchanged from that used in [7], and its volume measured 50.8 cm wide, 10.2 cm deep, and 137.2 cm length. It had a 10 cm (4") aluminum C-channel frame and

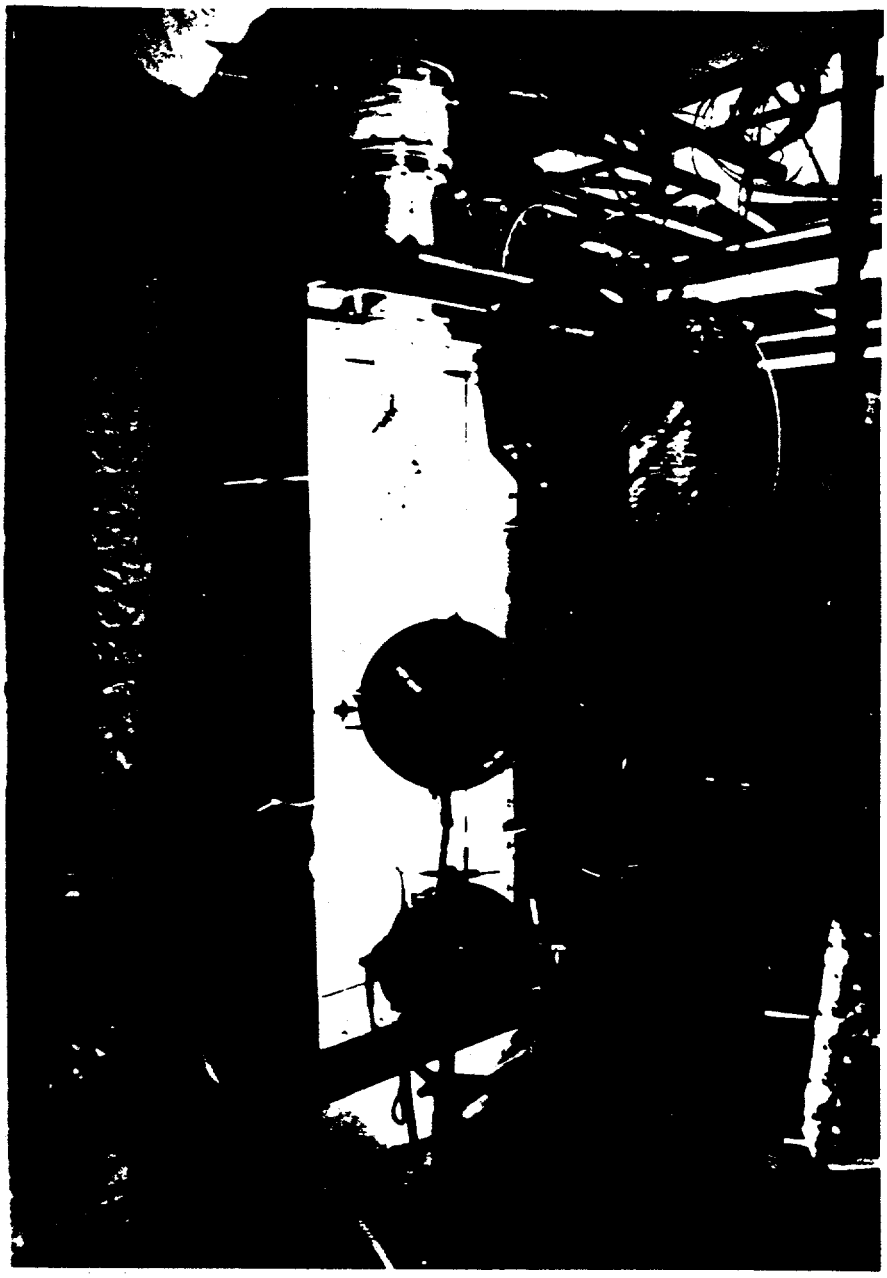

Figure 3-1: Photograph of MFSBS-MJ Experimental Apparatus

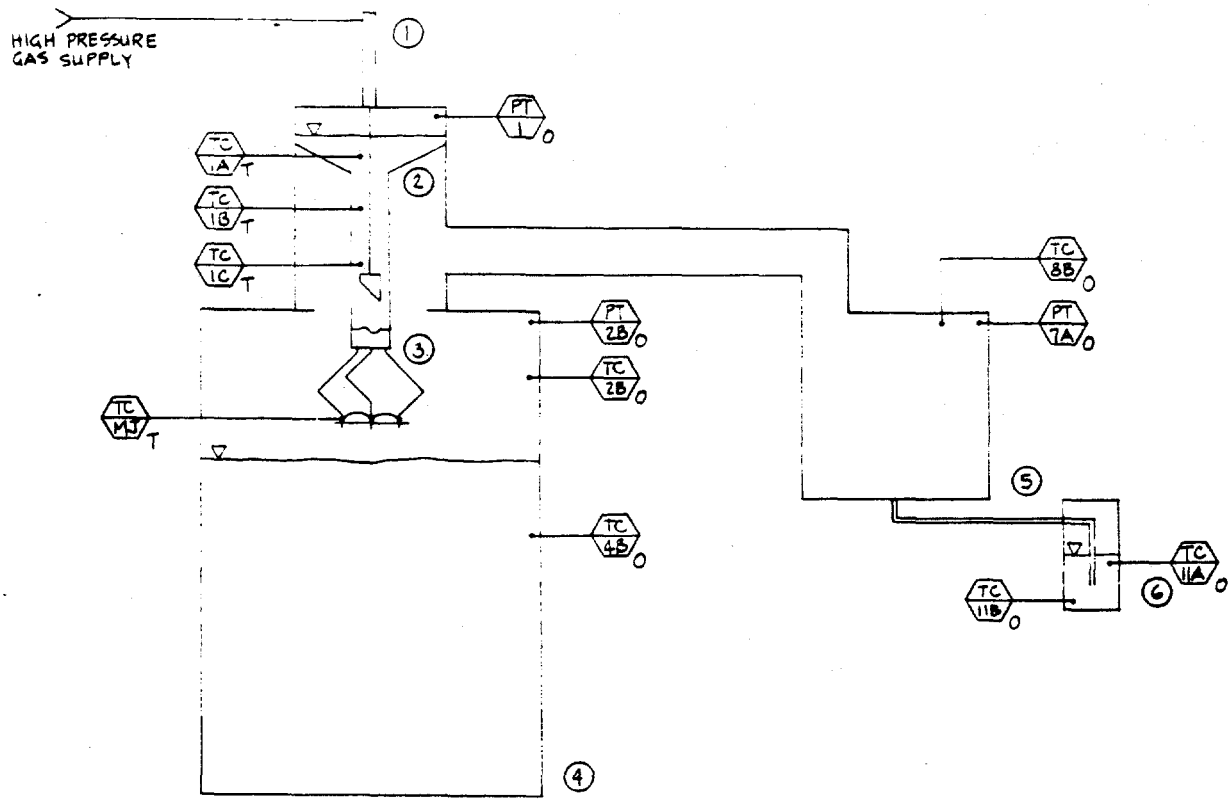

LEGEND

(1)	CUTTER ASSEMBLY
(2)	MELT FURNACES
(3)	MULTIPLE JET PIPING SYSTEM
(4)	INTERACTION VESSEL
(5)	EXPANSION VOLUME
(6)	CONDENSER
TC-x	THERMOCOUPLE LOCATION (-x DESIGNATION)
PT-x	PRESSURE TRANSDUCER (-x DESIGNATION)
O	RECORDED ON OSCILLOGRAPH
T	RECORDED ON TRENDICATOR

Figure 3-2: Schematic Diagram of Experimental Apparatus

1 cm (3/8" nominal) thick plexiglass walls on the front and back faces for internal viewing. A white cloth sheet was placed behind the back wall to diffuse light from the incident high wattage light sources (see Figure 3-1).

The multiple jet piping system was designed to evenly disperse the melt flow into three independent paths. Figure 3-3 shows a multiple jet piping system in the test apparatus. The system was made from 1.9 cm (3/4") copper tubing and elbows, and extended from an aluminum base plate that attached to the bottom of the diaphragm holder. Each path terminated at predetermined centerline spacings in a thin aluminum plate. Furthermore, each path used the same length of straight tubing and the same amount, and type, of elbows to ensure similar flow losses. Flow straighteners (roughly 2 cm length, 10 mil Br) were inserted, generating a four quadrant flow path, into the final straight segment of each path to reduce swirl in the melt flow. Four multiple jet piping systems were constructed corresponding to the specific nozzle centerline spacings: 12.7 cm (5"), 7.6 cm (3"), 3.8 cm (1.5"), and 1.9 cm (3/4"). Three sets of copper nozzles (outlet diameters: 1.3 cm (1/2"), 0.95 cm (3/8"), 0.65 cm (1/4")) were used interchangeably to achieve various nozzle-spacing-to-diameter ratios. The 1.9 cm spaced multiple jet piping system was constructed with 1.27 cm copper tubing and elbows and utilized a separate set of same outlet diameter copper nozzles. Heating tape (Omega SRT-051 series) was used to uniformly heat each system above the melt temperature of the metal. One 110 Vac Variac controlled circuit supplied power to the multiple jet piping system in the interaction vessel.

The cutter assembly included a piston/cylinder (Bimba 094-DP) mounted on a stainless steel furnace cover plate, a stainless steel rod and cutter, and a high pressure gas line that connected to the upper chamber of the cylinder. The design specification for these components is given in Appendix A. The stroke of the piston was 10.8 cm and the leading edge of the cutter sat about 5

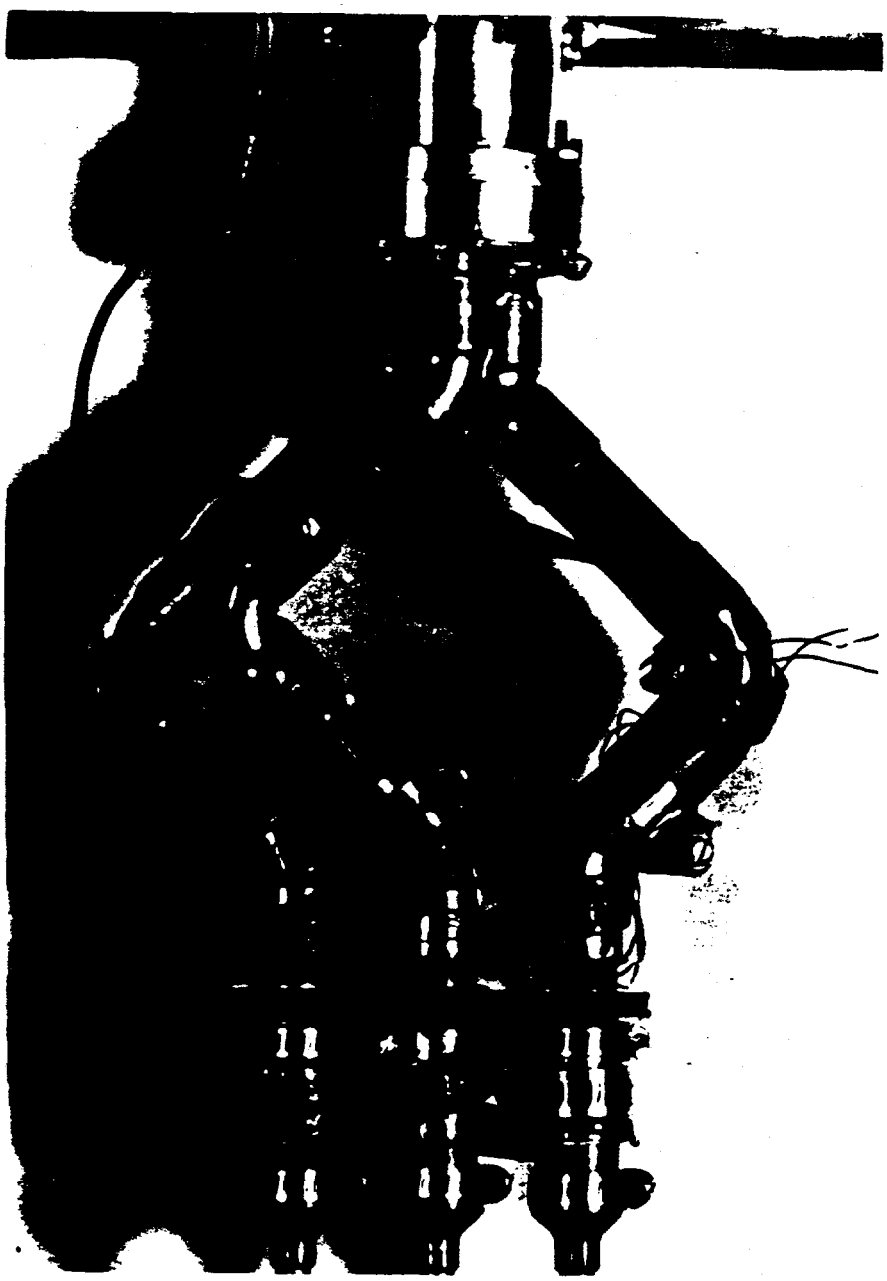

Figure 3-3: Photograph of Multiple Jet Piping System
(3.8 cm Spacing; 0.64 cm Diameter Nozzles)

cm above the diaphragm prior to the melt injection.

The condenser was used in series with the expansion volume to collect the vaporized coolant generated by the melt-coolant interaction. The condenser's volume was about 1.5 liters, and was half filled with subcooled coolant prior to each experiment.

3.1.2 Instrumentation

Ungrounded type K thermocouples (Omega CAIN series) and 0-25 psia rated pressure transducers (Omega model PX102, energized from an externally balanced circuit) were used to extract data during the multiple jet experiments. The instrumentation used to record this data was a Honeywell model 1858-079HG visicorder oscillograph and a Thermo-Electric °C type trendicator. Figure 3-2 shows the thermocouple and pressure transducer locations, which are symbolized by a hexagonal box with the designations TC- and PT-, respectively.

3.1.3 Data Acquisition Equipment

During the multiple jet experiments, two high speed motion picture cameras (Red Lake Laboratories, Inc. model K2004E-115 Hycams with Angenieux zoom lenses) were used to record the melt-coolant interactions. This information was recorded on Eastman 7250 High Speed Tungsten Ektachrome film at 500 frames per second.

Also, a Sanyo CCTV camera (model VDC 3950 with a Variogon lens) was used to record the melt-coolant interactions. This information was recorded by a Sharp VHS video cassette recorder (model VC-797U) at 30 frames per second.

An x-ray flash system (Hewlett-Packard model 43731A) was used to produce a radiograph during the melt-coolant interactions. Figure 3-4 shows the location of the radiography equipment. The radiographic film was placed in a Kodak X-Omatic cassette with Lanex Fast Screens and positioned behind a stationary x-ray grid. The radiograph was produced on Kodak 8*10 inch TMH-

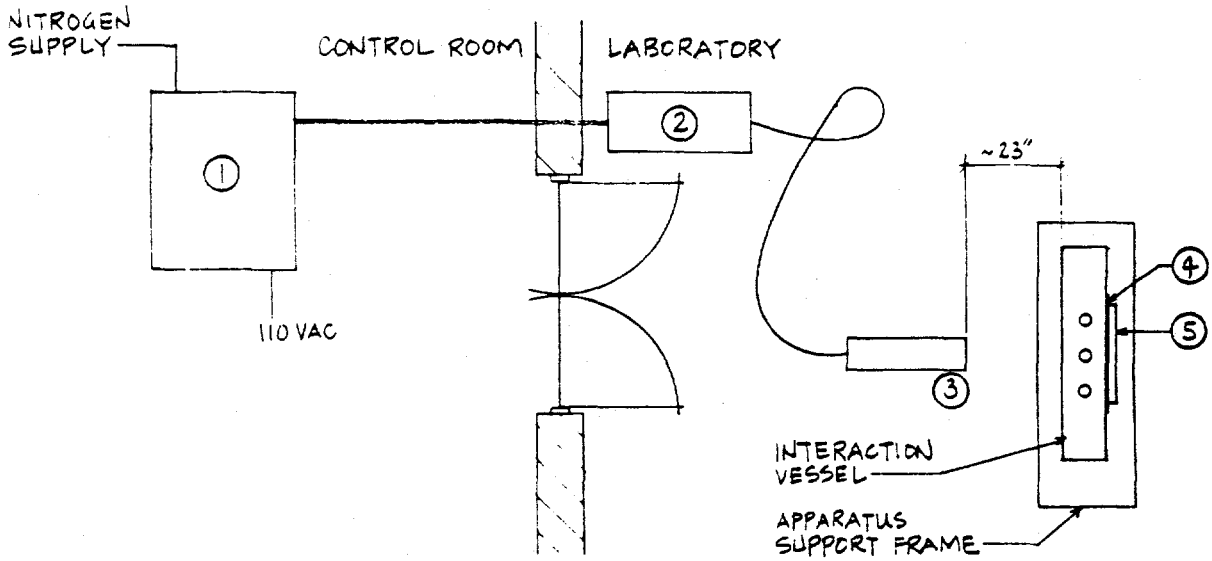

LEGEND

(1) X-RAY CONTROL CABINET
includes: HV POWER SUPPLY
DIGITAL DELAY GENERATOR
NITROGEN REGULATOR PANEL
TRIGGER AMPLIFIER

(2) X-RAY PULSER (100 keV)

(3) STRAIGHT LINE X-RAY TUBEHEAD

(4) STATIONARY X-RAY GRID (6:1)

(5) X-RAY FILM CASSETTE

Figure 3-4: Schematic Diagram of X-Ray Flash System

1 Diagnostic film.

3.1.4 Simulant Materials

The same simulant materials (Cerrobend metal alloy, weight % composition: 50.0 Bi, 26.7 Pb, 13.3 Sn, 10.0 Cd; Freon 11, saturation: 23 °C and 1 atm) were used in the MFSBS-MJ experiments as in [7]. Table 3-1 summarizes the relevant properties of the simulant materials. The selection of the simulant materials is discussed in [7]. Basically, these materials were selected to hydrodynamically simulate the interaction characteristics of reactor materials. This included insuring continuous phase boiling during the melt-coolant interactions, and providing a simulant material density ratio ($\sim$6:1) close to that of reactor materials. Also, these materials were easily obtained and readily usable.

Relevant Material Properties	Cerrobend	Freon 11 (liq/vap)
Density (kg/m3)	9200	1477/5.8
Surface Tension (N/m)	0.4	0.019
Melting Point (°C)	70	-
Boiling Point (°C)	-	23.8
Heat of Vapor. (kJ/kg)	-	180.2
Heat of Fusion (kJ/kg)	33	-
Heat Capacity (kJ/kg/°C)	0.17	0.87/0.50

Table 3-1: Relevant Properties of Simulant Materials used in MFSBS-MJ Experiments [20,21]

3.2 Experimental Procedure

To consistently capture the transient nature of the MFSBS-MJ experiments, a detailed procedure was followed throughout the test matrix. In the present section, a general description of the experimental procedure is given, along with a review of the instrumentation control systems. The procedure form used in the multiple jet experiments, a schematic diagram of the experimental apparatus, depicting manually operated valves (MV-) and gas/coolant sources, and a listing of equipment connections is given in Appendix B.

The experimental procedure is summarized as follows:

- make line voltage power connections
- calibrate oscillograph
- position Hycams; load film
- position VCR camera; cue VHS tape
- secure metal diaphragm
- fill furnaces with metal particulate
- melt metal; remove metal oxide
- secure piston/cylinder assembly
- position x-ray tube and film cassette
- fill interaction vessel with coolant
- partially fill condenser with subcooled coolant
- turn on lights
- charge x-ray generator
- remotely trigger oscillograph and high speed cameras
- remotely trigger piston/cylinder solenoid and x-ray generator

- record melt-coolant interaction process

- turn off all power; reset switches

- drain interaction vessel

The general dynamics of the experiment were as follows: Low pressure Argon gas was used to cover the melt in the furnace (to prevent oxidation) and the coolant in the interaction vessel (to suppress boiling during filling/draining). The cover gas in the interaction vessel was vented prior to the melt injection. The melt flow was initiated by the cutting of the diaphragm and was driven, by gravity, through each path of the multiple jet piping system. Upon exiting the nozzles, the flow penetrated the liquid coolant in the interaction vessel, producing significant boiling of the coolant. The coolant vapor was collected in the condenser.

3.2.1 Control Systems

Each melt injection was initiated by the successive, remote, manual closing of the oscillograph circuit, the Hycam circuit, and the timer circuit, which signalled the piston/cylinder solenoid and the x-ray generator. Figure 3-5 shows a schematic diagram of these control systems.

The closing of the oscillograph low voltage control circuit signalled the activation of a twenty second timed trace recording from the oscillograph.

The closing of the Hycam control circuit signalled the start of the film recording in each camera.

The closing of the 110 Vac timer circuit signalled the timer to complete the 110 Vac circuit controlling the piston/cylinder solenoid. The energized solenoid, which remained energized until the timer setting time elapsed, opened a pneumatically operated valve, releasing high pressure Argon gas into the piston/cylinder forcing the cutter through the diaphragm.

The second function of the timer was to close a delayed 25 Vdc circuit that signalled the

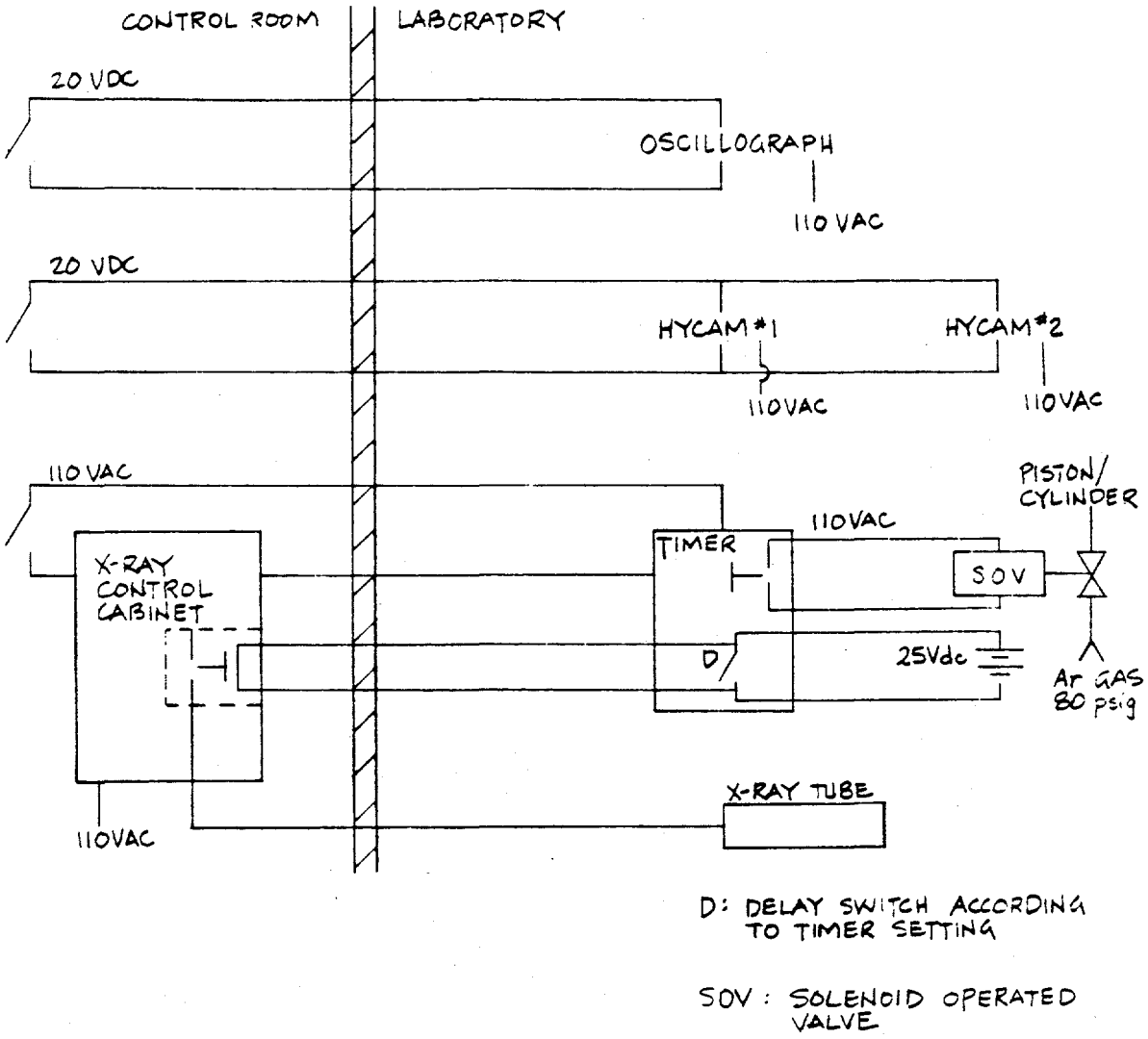

Figure 3-5: Schematic Diagram of Apparatus Control Systems

activation of the x-ray generator. The control circuit was delayed according to the timer setting.

An interlock control system (not shown) was provided as part of the Experimental Safety Plan to shut down the HV power supply in the x-ray control cabinet if any of the (3) doors opening to the lab were not secured during the melt injection.

3.3 Experimental Data

To achieve the objectives of the MFSBS-MJ experimental investigation the data generated was necessarily of the same nature as in the MFSBS experiments. In the present section, the development of the test matrix is given, followed by a summary of the data recorded in the MFSBS-MJ experiments.

3.3.1 Test Matrix

The test matrix used in the MFSBS-MJ experiments is shown in Table 3-2. The development of the test matrix was based on a geometric scaling parameter and the procedural successes of each experiment. The resulting test matrix accomplished an encompassing variation of spacing ratios ranging from vapor channel independence to minimal jet separation.

The geometric parameter that governed the development of the test matrix was the nozzle spacing-to-diameter (S/d) ratio. This ratio was varied to home in on a nozzle configuration that produced noticeable interactions between adjacent jets. The range of this ratio was 20:1 to 1.5:1. The first multiple jet piping system was designed for a nozzle-to-nozzle centerline spacing dimension of 12.7 cm to allow the vapor channels of adjacent jets to roughly approach interaction (the limiting case of interest). The 50.8 cm width of the interaction vessel ensured that a continuous column of liquid coolant would be maintained during any melt-coolant interaction. Successive multiple jet piping systems were designed to induce vapor channel (and possibly jet) interactions via a systematic reduction of the nozzle spacing-to-diameter ratios.

MFSBS-	Nozzle			X-ray		Comments
	S (cm)	d (cm)	S/d	Quality	Position	
MJ1	12.7	0.64	20	-	high	scoping; new spacing
MJ2	12.7	1.27	10	poor	high	scoping; new spacing insufficient melt
MJ3	7.6	1.27	-	high	high	scoping; single jet comparison
MJ4	7.6	0.95	8	-	high	new spacing diaphragm cutoff
MJ5	7.6	1.27	6	good	high	new spacing diaphragm cutoff
MJ6	3.8	0.95	4	poor	low	new spacing diaphragm cutoff
MJ7	3.8	1.27	3	-	low	new spacing diaphragm cutoff
MJ8	3.8	1.27	3	poor	low	repeat MJ7(mechanical) diaphragm cutoff
MJ9	3.8	1.27	3	high	high	repeat MJ8(mechanical)
MJ10	3.8	1.27	3	poor	low	reliability MJ9
MJ11	3.8	0.64	6	-	low	repeat MJ5(mechanical)
MJ12	1.9	1.27	1.5	poor	low	new spacing diaphragm cutoff
MJ13	1.9	0.95	2	good	high	new spacing
MJ14	1.9	0.95	2	good	low	reliability MJ13
MJ15	3.8	0.95	4	good	low	repeat MJ6(mechanical)
MJ16	1.9	0.64	3	-	-	new spacing pressurized furnace
MJ17	3.8	0.64	6	high	high	repeat MJ5(mechanical) pressurized furnace

Table 3-2: MFSBS-MJ Experimental Test Matrix Including Development Details

In all MFSBS-MJ experiments (except MJ16), the production of a radiograph was attempted. The test matrix was influenced by the desire to repeat some experiments to achieve a high quality radiograph. The results are shown in Table 3-2. The quality of each radiograph was rated as high, good, or poor. A high quality radiograph showed excellent definition of the multiple metal jets, the jet fragments, and an outline of the vapor channel. A high quality radiograph is shown in Figure 3-6. Similarly, a good quality radiograph showed moderate refinement of the same details, and the poor quality radiograph was illegible. In the tests with no x-ray quality rating, the x-ray system did not trigger or triggered prematurely, resulting in a radiograph of undisturbed liquid.

Furthermore, the test matrix was influenced by the desire to generate a set of radiographs that captured successive segments of the multiple jets at the quasi-steady state. Two tests, of similar geometry, were run with different x-ray cassette locations; one in the *high* position, and the other in the *low* position. This is summarized in Table 3-2. The *high* x-ray position corresponded to the film cassette being seated at 110 cm above the laboratory floor. Similarly, the *low* position was 77 cm above the lab floor.

Finally, the development of the test matrix was influenced by the successes and malfunctions of each experiment. The decision to run a particular experiment was based on one or more of the following: scoping purposes; new nozzle spacing-to-diameter ratio; repeat to correct a mechanical malfunction; repeat to establish the validity of the MFSBS-MJ data; repeat with a relocated x-ray film cassette. The objective of each experiment, along with the type of malfunction or special condition, are summarized in Table 3-2.

3.3.2 Pre-Melt Injection Data

During the pre-melt injection portion of the procedure, data was collected to verify the readiness of the apparatus and to provide base data for each MFSBS-MJ experiment.

Figure 3-6: Photocopy Reproduction of High Quality Radiograph (from MFSBS-MJ17)

The readiness of the apparatus was determined by the following conditions: The x-ray timer delay was set according to the anticipated time needed for the melt injection to reach its breakup length. This time represented the delay between the initial motion of the cutter to the firing of the x-ray tube (see Figure 3-5). The average multiple jet piping system temperature was necessarily higher than the melting temperature of the metal to prevent freezing during the melt injection. These conditions are summarized in Table 3-3.

The data on the static conditions of the melt and coolant are presented in Table 3-4. The metal particulate mass was measured in all experiments except those shown as approximations. The melt temperature was measured as the average reading of the (3) thermocouples in the melt furnaces. This temperature was required to be in the range of 100 to 110 °C. The coolant depth in the interaction vessel (at room pressure) was measured to verify that it was greater than the expected jet breakup length and to determine the nozzle-to-coolant surface distance. A volume of coolant vapor was captured in the condenser during the melt-coolant interactions and was measured at its pretest subcooled temperature (about -20 °C). This was recorded in all experiments except those indicated by a dash. Also, it was suspected that the condensed vapor volume measurement in MJ17 was stated incorrectly and should have been 75 ml.

3.3.3 Melt Injection Data

In each MFSBS-MJ experiment, the melt-coolant dynamics were captured by an oscillograph, high speed video cameras, VCR, and x-ray flash system. A presentation of this data is prevented due to its recording media, but a general description of the type of data is given. The results of this report are largely based on analysis of this data (see Section 4).

An oscillograph trace was generated to quantify the variations in the furnace pressure, interaction vessel pressure, expansion volume pressure, coolant temperature in the interaction vessel,

MFSBS-	X-ray Timer(sec)	MJ System Ave T(°C)	Lab Ave T(°C)
MJ1	1.0	98	22
MJ2	0.8	106	21
MJ3	1.0	106	23
MJ4	0.9	110	25
MJ5	1.0	108	24
MJ6	0.8	103	23
MJ7	0.7	109	25
MJ8	0.9	107	24
MJ9	0.9	110	21
MJ10	0.95	108	22
MJ11	1.0	111	24
MJ12	0.95	111	22
MJ13	0.75	109	23
MJ14	0.75	110	19
MJ15	0.75	110	21
MJ16	-	107	22
MJ17	0.75	107	21

Table 3-3: Pre-Test Apparatus Data
from MFSBS-MJ Experiments

MFSBS-	Melt		Coolant	
	Mass (kg)	Temp.(°C)	Depth(cm)	Vapor(ml)
MJ1	~8	98	88.0	80
MJ2	~8	106	87.5	-
MJ3	7.43	106	95.0	-
MJ4	13.68	110	90.0	110
MJ5	~16	108	91.0	-
MJ6	~16	103	89.0	130
MJ7	~17	109	94.0	-
MJ8	~19	107	94.5	-
MJ9	21.73	110	93.0	130
MJ10	21.35	108	94.5	160
MJ11	16.00	111	84.0	225
MJ12	18.60	111	90.5	120
MJ13	14.78	109	94.0	130
MJ14	14.87	110	94.0	90
MJ15	14.33	110	90.5	155
MJ16	8.07	107	92.5	65
MJ17	10.25	107	91.0	25(75)

Table 3-4: Pre-Melt Injection Data
from MFSBS-MJ Experiments

and the subcooled coolant temperature in the condenser. Figure 3-7 shows a sample trace. Appendix C contains photocopied reproductions of portions of the oscillograph traces produced in the MFSBS-MJ experiments (scales: time - 1 second per 10 increments; pressure - 1.25 psia per division; temperature - 12.5 °C per division).

High speed video camera #1 and the VCR camera recorded an overall view of the melt-coolant interactions which captured the dynamics of the opaque vapor channel and the trajectory of the melt particles once outside the vapor channel. Selected frames extracted from Hycam #1 film are shown in Figure 3-8. Hycam #1 recorded information at a greater rate (about ten fold) and at higher resolution than the VCR recording. The VCR recording provided instant and accessible reviewing of the melt-coolant interactions. High speed video camera #2 recorded a close-in view of the melt injection from the nozzles to the coolant surface. Selected frames from Hycam #1 and #2 films for various tests are presented in Appendix D.

The x-ray flash system was used to generate a single frame radiograph during the melt-coolant interactions. This provided a visualization of the jets interactions with the coolant/vapor at a selected position. A sample radiograph was shown in Figure 3-6, depicting a portion of the metal jets and fragmentation within the vapor channel. Appendix E contains photocopied reproductions of the good and high quality radiographs produced in the MFSBS-MJ experiments.

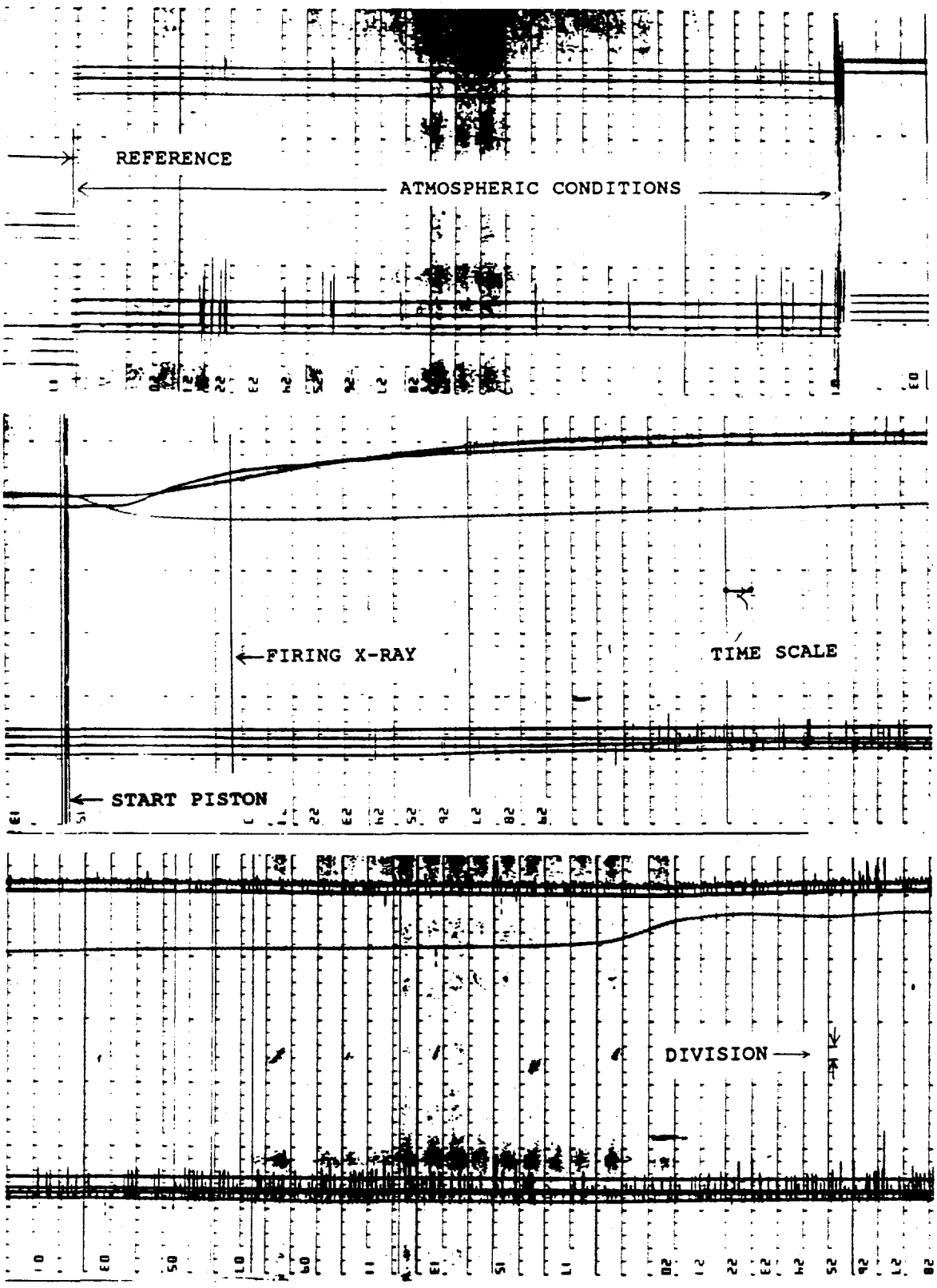

Figure 3-7: Sample Oscillograph Trace (from MFSBS-MJ4)

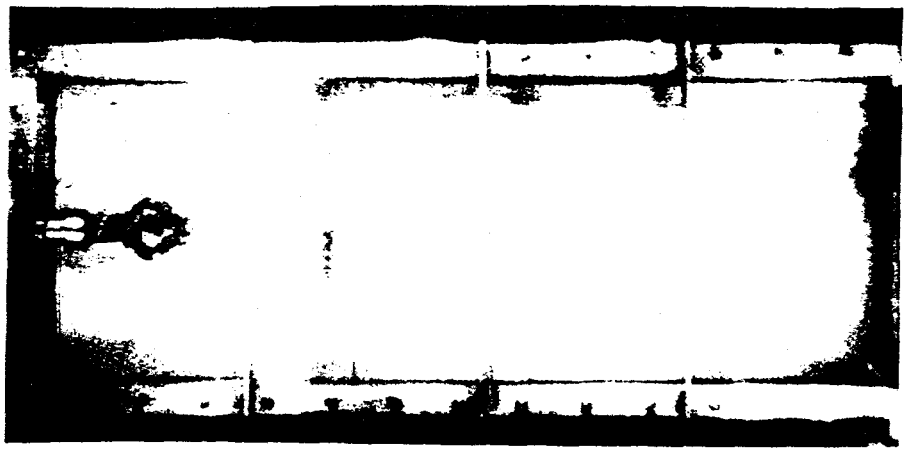

(Solenoid - 0 ms)
Contact - 350 ms

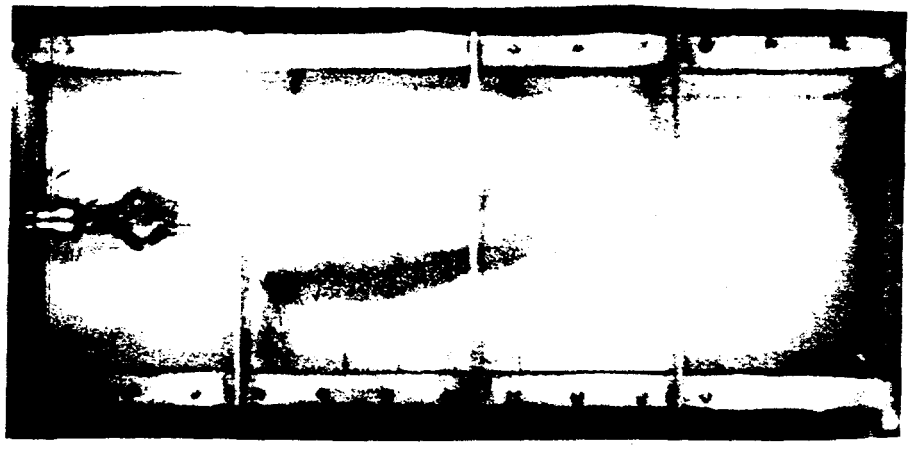

Time - 446 ms

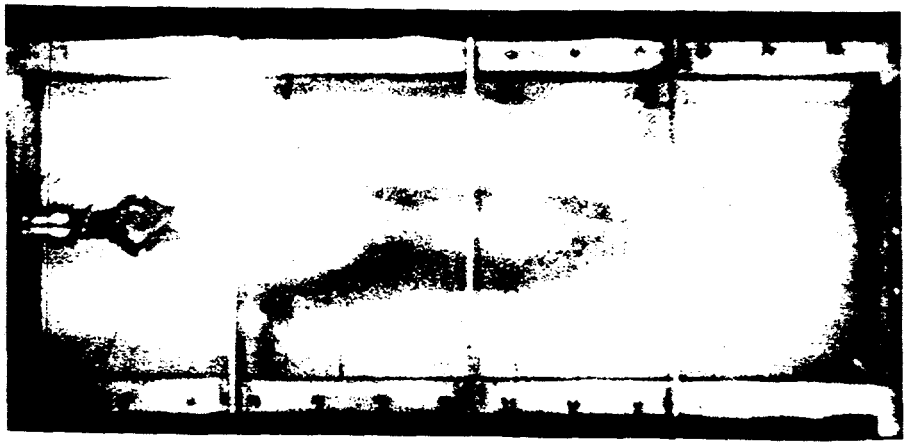

Time - 534 ms

Figure 3-8: Selected Frames from Hycam #1 Film (from MFSBS-MJ16)

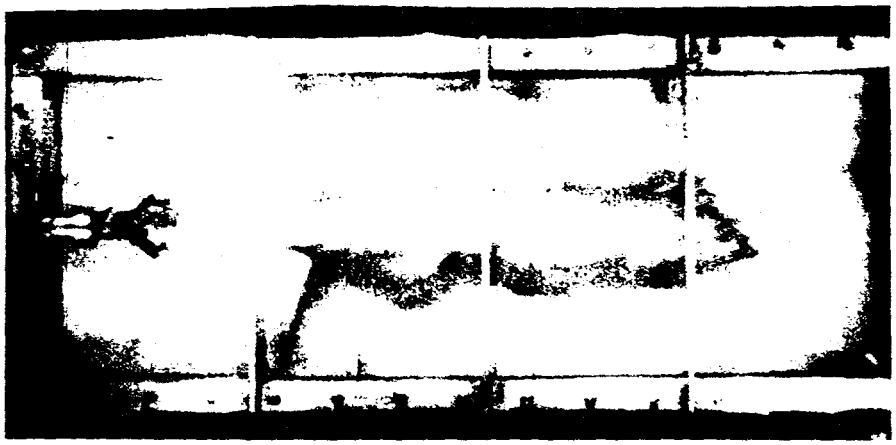

Breakup - 640 ms

Time - 1268 ms

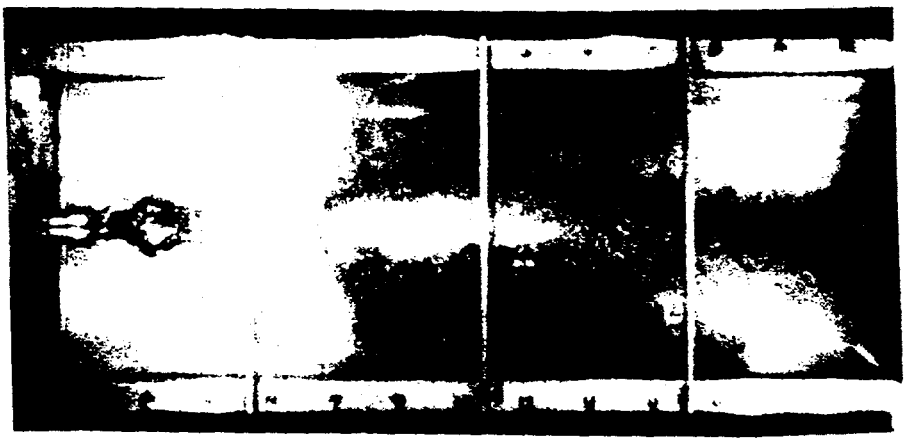

Time - 2308 ms

Figure 3-8 (Continued): Selected Frames from Hycam #1 Film (from MFSBS-MJ16)

4. DATA ANALYSIS

An analysis of the MFSBS-MJ experimental data was performed to characterize the melt-coolant interactions. This included a detailed description of the experimental observations and comparison to the 'boiling' jet breakup correlation presented in [9].

In the present section, an overview of the MFSBS-MJ test matrix is given to qualify the conditions under which the data was generated. This is followed by experimental observations and an analysis of the data to achieve the above mentioned goals.

4.1 Test Matrix Review

The MFSBS-MJ test matrix was shown in Table 3-2. The first three experiments were conducted for scoping reasons (i.e.; to achieve proper apparatus operation, to assess (and modify) the procedure form, and to achieve consistent melt pours). In MJ1, the initial melt streams had significant radial momentum as they exited the nozzles. This was attributed to temporary freezing in the multiple jet piping system and contiguous streams prevailed. In MJ2, an insufficient amount of melt was used so that a breakup length was not achieved. MJ3 verified that the melt stream characteristics (breakup length and fragmentation) were similar to those established in the MFSBS experiments. Only the center nozzle of the 7.6 cm multiple jet piping system was used in this test. This was the first test run with flow straighteners in the apparatus. The remaining tests (MJ4 through MJ17) were run in the production mode and the data generated was analyzed. In MJ4 through MJ8, a common malfunction was the complete severing of the diaphragm, which caused partial blockage of each pipe entry and reduced the melt velocity in each path. When it was determined that the diaphragm was being pulled off during the cutter stroke due to high shear stress, the cutter and diaphragm were modified. Cutter modifications were tried in MJ7 through MJ9 and various diaphragm materials were used throughout the tests. From initial reviews of the VCR

recording, it appeared that the 3:1 spacing produced melt stream interactions near the breakup length. Therefore, this spacing was repeated (MJ7 through MJ10) until proper operation of the experimental apparatus was achieved. No x-ray was attempted in MJ16. In MJ16 and MJ17, the furnace was pressurized to about 10 psig and isolated from the Argon gas supply prior to the melt injection to increase the melt stream velocity.

4.2 Experimental Observations

The data from the MFSBS-MJ experimental investigation was generated by high speed motion picture cameras, single flash radiography, and oscillograph trace outputs.

4.2.1 Motion Picture

High speed motion pictures from Hycams #1 and #2 were used in the MFSBS-MJ experiments to estimate the collective jet breakup lengths and the jet velocity at the coolant surface, respectively (see Appendix D). The large spacing ratio in MJ1 prevented the interaction of adjacent vapor columns, while all other tests run in the production mode had significant interaction with adjacent vapor columns. The collective observations of the overall melt-coolant interactions, recorded by Hycam #1, are presented.

The initial penetration of the molten metal jets produced significant vaporization of the continuous phase. The vapor was generated primarily at the jets' leading edge with an opaque vapor column expanding to the coolant surface. A sinuous boundary existed between the vapor and the liquid coolant, and 'bulges' of vapor propagated toward the coolant surface. The time needed for the jets to achieve a quasi-steady state condition (i.e.; the time to reach the breakup length from initial coolant contact) was about one-quarter second. During the time of significant velocity head (about one-quarter second), small metal drops and filaments were entrained in the counter-axial vapor/liquid flow, carried to the coolant surface, and then fell, under gravity, to the floor of the

interaction vessel. Near the breakup length, some spreading of the large drops occurred as they penetrated the coolant, solidified (at least on the surface), and fell to the bottom of the vessel. The distribution of particles in the debris bed verified these observations; very small spherical droplets were dominant at the side walls, while the centrally located main pile was characterized by much larger irregularly shaped globules.

To help visualize the breakup phenomenon, a sketch of an ideal jet penetrating a volatile liquid is presented in Figure 4-1, where the jet diameter represents the equivalent average diameter of the sinuous/segmented jet flow. The breakup length is shown as the depth at which the jet core no longer exists.

The standard video recording offered a much coarser view of the same event. Prior to the melt injection, moderate boiling occurred near the coolant surface, which was influenced by the hydrostatic pressure gradient and the pressurization of the interaction vessel. During the melt injection, the vapor channel developed to about twice the distance between the outer nozzles and was maintained through the breakup length, and, thereafter, became quite sinuous. Also, the debris bed, largely contained near the center of the interaction vessel, generated significant amounts of vapor for a long period of time (order of minutes) after the melt injection. Near the end of the melt injection, rising vapor pinched the falling melt particles toward the center of the vessel. This competition for flow area was observed to be due to size limitations of the interaction vessel.

4.2.2 Radiograph

The opaque nature of the vapor channel restricted visualization of the jet breakup mechanisms by conventional photography. In the MFSBS-MJ experiments, this was overcome by the use of an x-ray flash system that produced single flash radiographs of the melt stream breakup phenomenon (see Appendix E). It is noted that interpretation of radiographs is subjective, since a radiograph is

a two-dimensional projection of a three-dimensional event. Thus, the projection of several masses may superimpose to give the appearance of a single mass on the radiograph.

Upon collective observation of the radiographs, large scale (of order of the jet diameter) deformations and discontinuities of the melt streams were apparent, as was small scale (of order

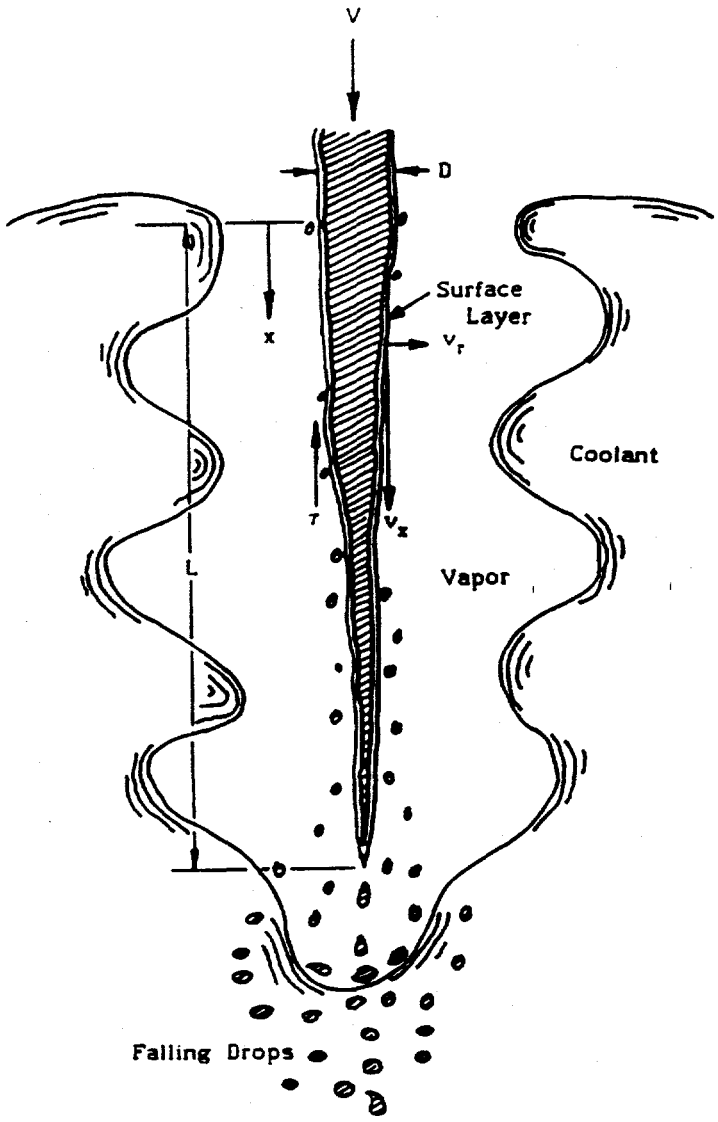

Figure 4-1: Sketch of an Idealized Molten Metal Jet Breakup in a Volatile Liquid [10]

very much smaller than the jet diameter) erosion. Also, the sinuous boundaries of the local vapor channel and particle entrainment were evident.

From review of the Hycam #2 film, varicose deformations developed on the melt stream columns prior to their penetration of the coolant (see Appendix D, p.103). Within the vapor channel, long wavelength helical deformations grew with the penetration depth and led to the ejection of globules from the crests and segmentation of the melt streams (see MJ3, MJ5, MJ9, MJ17). This phenomena was observed well above the breakup length and the globules and segments appeared to maintain significant axial motion. Near the breakup length, further segmentation was observed, indicating that the melt achieved some radial momentum (see MJ14). The physical progression of the melt streams breakup in the coolant vapor appeared to follow observations by Hoyt [15] for a high speed water jet in a comparable velocity counter-axial air flow.

There was evidence of coagulation between adjacent jets for some of the small spacing ratios (see MJ9, MJ13, MJ15). It appeared that the large amplitude helical deformations of adjacent jets impinged upon one another and the merged jets continued to deform in the manner described above (see MJ13, MJ15). There was no apparent effect on the breakup length estimates for these cases.

Of comparable importance to the large scale segmentation was the small scale fragmentation and erosion of the melt surfaces. Melt droplets and filaments appeared to be stripped from the vertical surfaces of the contiguous melt columns and globules/segments along the entire penetration depth (see MJ9, MJ13, MJ17). The ejected particles appeared to be swept upward in the counter-axial flow of the coolant vapor/liquid, where further fragmentation was possible. These particles later appeared to be entrained in the liquid coolant as they fell to the bottom of the interaction vessel in a solidified state (see Figure 3-8). Droplet entrainment in the counter-axial vapor flow ejecting from the coolant surface was not observed.

4.2.3 Oscillograph Trace

The oscillograph traces were reviewed to illustrate the test dynamics (see Appendix C). The trends of each test were similar and a representative trace is discussed here.

The mechanics of the test procedure recorded on the oscillograph trace were: pre-test calibration of the oscillograph included an output of the reference state and the atmospheric conditions; the oscillograph was remotely started just prior to the activation of the piston/cylinder solenoid, which initiated the pour; and, a delayed signal triggered the x-ray tube at the approximate time of the breakup length.

The melt furnace was pressurized by a low pressure gas supply provided to cover the melt. The furnace pressure was constant prior to the melt injection and decreased rapidly with the initiation of the melt flow. The pressure stabilized due to increased gas flow resulting from the pressure drop change between the pressure regulator and the increasing furnace volume. In MJ16 and MJ17 the supply gas was shut off prior to the test. Well beyond the transients of the test, a path between the furnace and the interaction vessel opened, due to depletion of the melt, and gas/vapor flow was induced until the pressures stabilized.

The interaction vessel pressure increased rapidly with the melt injection, causing significant vapor production and pool swell. Pressure fluctuations were observed to be caused by the unsteady vapor production and rising vapor bulges. These fluctuations dampened near the breakup length time, corresponding to reduced melt flow and observed reduction in vapor generation. The pressure asymptotically increased to a steady state shortly thereafter (about 1-2 seconds).

The vapor flow travelled from the interaction vessel to the expansion volume/condenser, and the corresponding pressure readings tracked each other well. The relatively large volume of the expansion volume dampened any pressure fluctuations present in the interaction vessel.

Minor increases in the condenser temperature were observed long after the breakup length was reached. Heating of the highly subcooled coolant by the ambient air may have caused this variation. Also, the low quality vapor and the large heat capacity of the condenser coolant support the negligible temperature change. Similarly, the expansion volume temperature changed negligibly.

The initial change in the coolant temperature in the interaction vessel was due to mixing of high enthalpy liquid coolant, swept from the vapor channel, with the local coolant near the thermocouple. One thermocouple was inadequate to track the coolant temperature.

A rapid decrease in the temperature at the top of the interaction vessel was observed near the breakup length time. The cover gas, heated by the multiple jet piping system heating tape in the pre-melt injection state, was thought to be swept out of the interaction vessel with the generation of vapor flow.

Early MFSBS-MJ tests had an additional thermocouple at the floor of the interaction vessel and did not track the condenser coolant temperature.

4.3 Data Reduction

The primary objective of the data reduction was to quantify the data for comparison to the 'boiling' jet breakup length correlation by Saito et. al. [9], involving the breakup length, the jet diameter at the coolant surface, and the Froude number.

4.3.1 Breakup Length

The breakup length was defined as the steady state depth from the pre-melt injection coolant surface at which significant reduction in axial momentum of the jets, collectively, was noticed. The subjective nature of this measurement prompted the breakup length to be determined by several methods. Table 4-1 summarizes the breakup length estimates.

A first estimate of the breakup length was visualized by reviewing the Hycam #1 film at

various speeds. Following this, the Hycam #1 film was used to measure the leading edge penetration length (from the pre-melt injection coolant surface) at four frame intervals (0.008 sec) well beyond the estimated breakup length. From this, a penetration length versus time graph was generated as shown in Figure 4-1. On this graph, the breakup length was estimated, and verified by Hycam film observation, as the location on the curve where the slope decreased considerably.

A more consistent method for estimating the breakup length was proposed in [7] using a central difference scheme to approximate the slope (i.e.; the penetration rate) of the penetration length versus time curve, and comparing this to the terminal velocity of the largest stable drop in freefall through the coolant. Thus, the drop freefall velocity was overlaid on a graph of the penetration rate versus penetration length and the point of intersection marked the breakup length. A sample graph, using the same data from Figure 4-1, is shown in Figure 4-2. The graphical results of the data extracted from the Hycam #1 film for each experiment are presented in Appendix F. In many of these graphs, the penetration rate curve oscillated about the drop freefall velocity line. The standard used was the intersection of the descending side of the last significant spike in the curve and the drop velocity line marked the breakup length. This analysis was most acceptable for the breakup length estimates. A final review of Hycam #1 film was done to verify the feasibility of the calculated breakup lengths.

The time from the initial penetration of the coolant to the breakup length was estimated from Figure 4-1. These estimates are given in Table 4-1.

4.3.2 Melt Streams

The melt stream velocity at the coolant surface was required to characterize the melt-coolant interactions. These calculations are summarized in Table 4-2.

Hycam #2 film was analyzed to estimate this velocity by recording the distance from the

MFSBS-	Measurement Technique			Time to Breakup (s)
	Observed Hycam #1	Penetration vs Time	Rate vs Depth	
MJ1	51	42	38	0.20
MJ2	-	-	-	-
MJ3	-	-	-	-
MJ4	52	47	44	0.25
MJ5	56	45	42	0.36
MJ6	54	47	45	0.22
MJ7	85	68	77	0.46
MJ8	73	78	74	0.40
MJ9	69	73	69	0.33
MJ10	93	92	92	0.42
MJ11	44	53	53	0.24
MJ12	70	64	64	0.40
MJ13	70	62	61	0.30
MJ14	74	62	61	0.29
MJ15	69	63	65	0.25
MJ16	73	72	72	0.30
MJ17	60	52	49	0.19

Table 4-1: MFSBS-MJ Dimensional Breakup Length Estimates (cm) and Time to Breakup from Coolant Surface

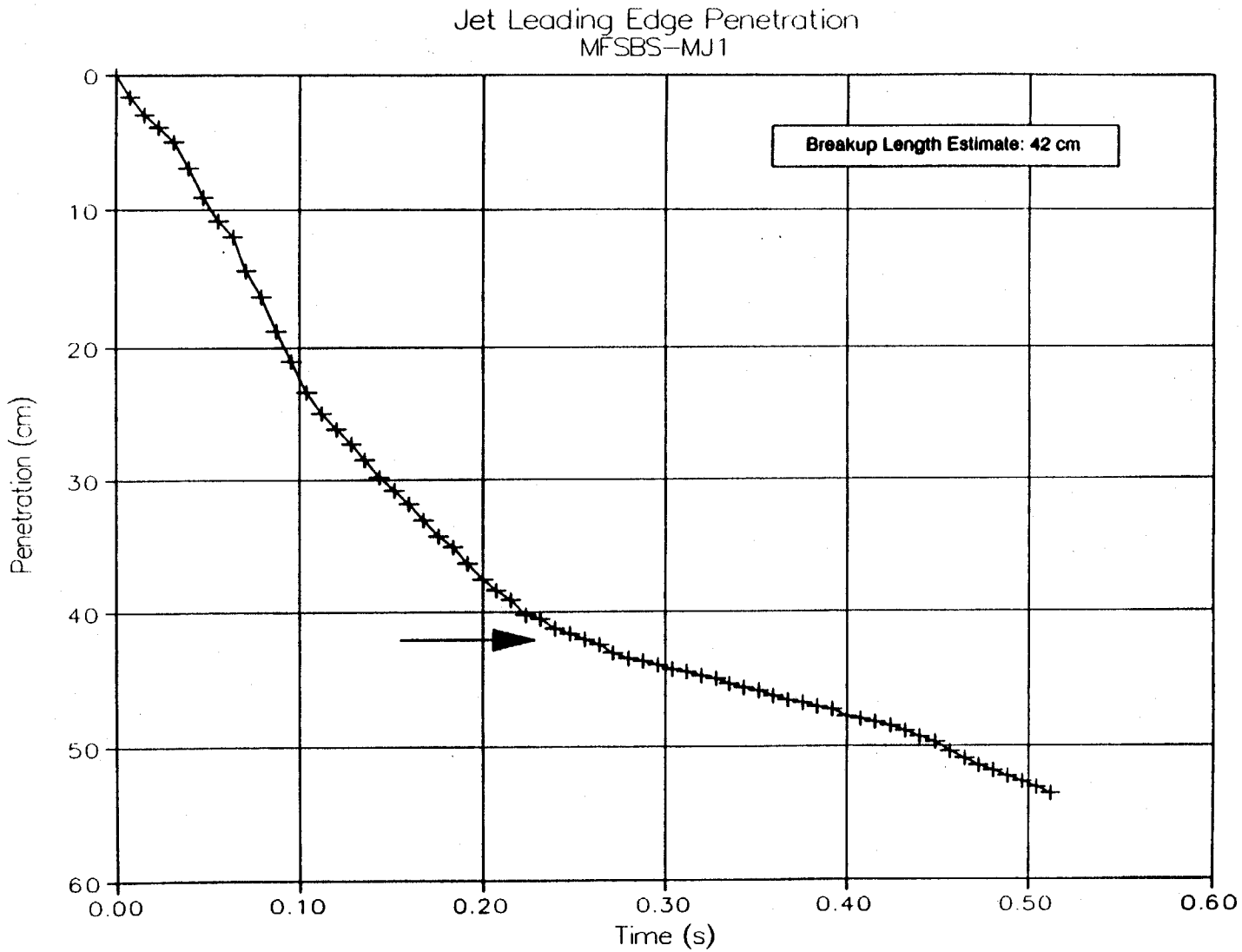

Figure 4-2: Multiple Jet Leading Edge Penetration vs. Time (from MFSBS-MJ1)

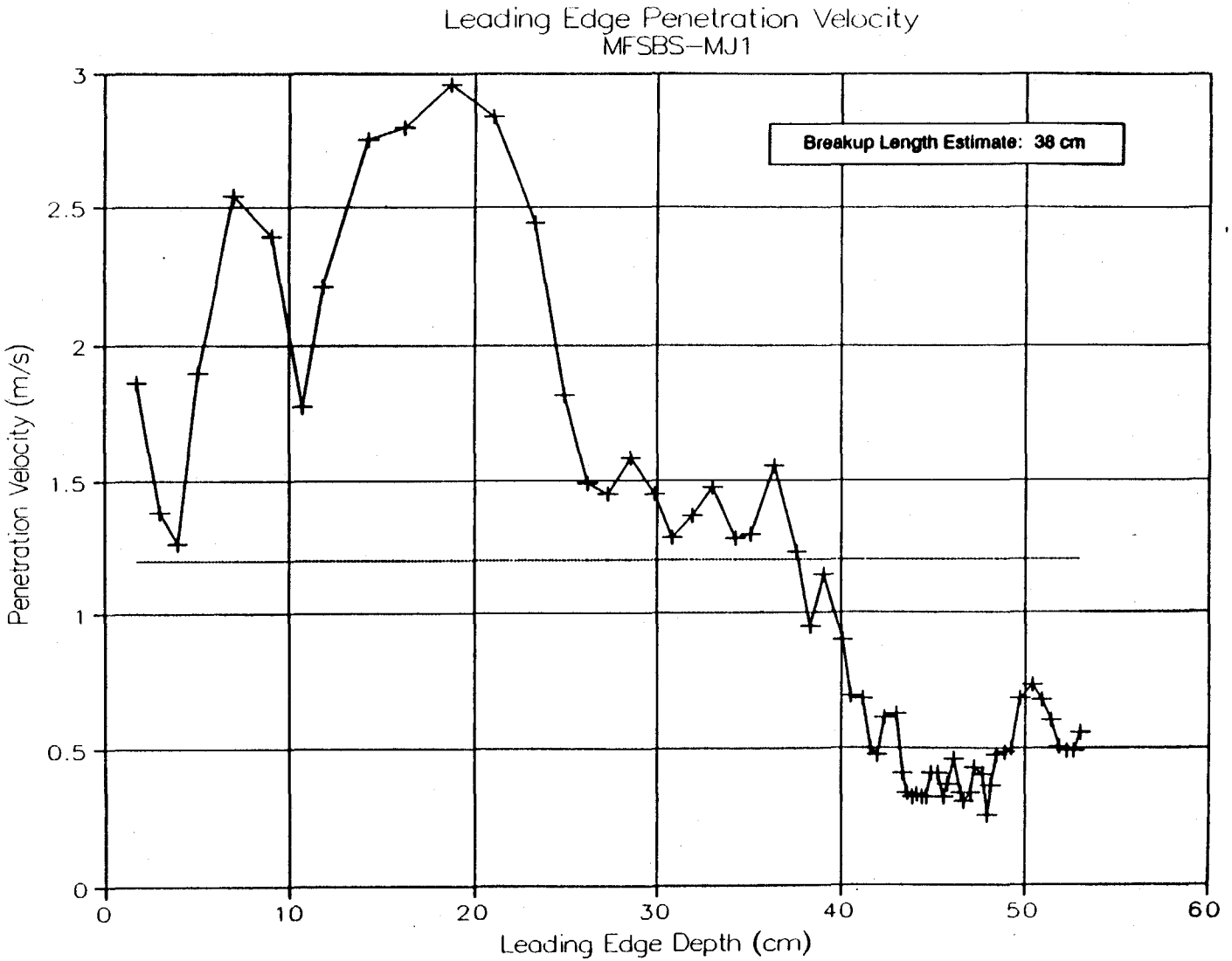

Figure 4-3: Multiple Jet Leading Edge Penetration Velocity vs. Penetration Depth (from MFSBS-MJ1)

nozzles to the coolant surface and the number of frames that the initial melt stream needed to traverse this distance. This information was sufficient to calculate the average melt stream velocity at the coolant surface. In some tests, the initial melt streams were fragmented and had significant deformation. It was suspected that the very fast cutter motion propelled some melt drops ahead of the main melt stream body, and for small diameter jets it was difficult to distinguish between the drops and the start of the main melt stream.

A limiting estimate of the melt stream velocity at the coolant surface was calculated by the Bernoulli velocity. The melt mass was used to calculate the initial height of the melt in the furnaces. It was assumed that the melt surface in the furnace varied negligibly during the time to reach the breakup length (i.e.; constant velocity), and the smaller of the velocity values was used to characterize the melt stream velocity at the coolant surface.

The final column in Table 4-2 shows the melt diameter at the coolant surface. This calculation was needed to normalize the breakup length and was assumed constant for the time needed to achieve the breakup length (about 0.3 seconds). The melt diameter accounted for stretching due to gravitational acceleration.

4.3.3 Vapor Generation

To further characterize the melt-coolant interactions, a calculation of the distribution of melt streams enthalpy was attempted from simple thermodynamic principles. The melt enthalpy (i.e.; sensible heat and latent heat of fusion) was distributed as follows: to the coolant in the form of sensible heat; to the generation of saturated vapor; and to the interaction vessel (i.e.; losses). These calculations are given in Table 4-3, which also gives the percentage of the total energy used for sensible heating of the coolant and for heat losses. Significant heat was lost from the system from calculations are given in Table 4-3, which also gives the percentage of the total energy used for

MFSBS-	Hycam #2 Observed(cm/s)	Bernoulli Velocity(cm/s)	Melt Diameter(cm)
MJ1	308	423	0.60
MJ2	-	-	-
MJ3	-	-	-
MJ4	287	431	0.90
MJ5	210	436	1.15
MJ6	288	441	0.87
MJ7	376	424	1.24
MJ8	432	422	1.24
MJ9	377	432	1.23
MJ10	405	427	1.24
MJ11	280	442	0.57
MJ12	520	439	1.20
MJ13	675	427	0.91
MJ14	519	427	0.91
MJ15	335	429	0.90
MJ16	697	444	0.61
MJ17	482	440	0.62

Table 4-2: Melt Stream Velocity and Diameter at Coolant Surface for MFSBS-MJ Experiments

sensible heating of the coolant and for heat losses. Significant heat was lost from the system from the non-solidified debris bed to the interaction vessel aluminum frame. Also, the time scale for the heat transfer to the coolant was very much greater than the breakup length time scale. These factors, and the non-uniform thermodynamic properties resulting from pressure variations in the interaction vessel during the melt injection, prevented a more detailed thermodynamic analysis. Also, only one thermocouple was located in the coolant pool for steady state pre-test readings and could not satisfactorily record the bulk temperature (i.e.; sensible heat) changes during these transient experiments.

MFSBS-	Melt Energy (kJ)	Vapor Energy (kJ)	Coolant/Lost Energy (%)
MJ1	302.1	21.3	92.9
MJ2	313.0	-	-
MJ3	290.7	-	-
MJ4	544.5	29.3	94.6
MJ5	631.4	-	-
MJ6	617.8	34.6	94.4
MJ7	673.7	-	-
MJ8	746.5	-	-
MJ9	864.9	34.6	96.0
MJ10	842.5	42.6	94.9
MJ11	639.5	59.9	90.6
MJ12	743.4	31.9	95.7
MJ13	585.7	34.6	94.1
MJ14	591.8	24.0	95.9
MJ15	570.3	41.3	92.8
MJ16	317.1	17.3	94.5
MJ17	402.7	20.0	95.0

Table 4-3: Melt Energy Distribution in MFSBS-MJ Experiments

5. RESULTS

The primary interest in the MFSBS-MJ experiments was to determine the influence of adjacent molten metal jets on a central jet during their simultaneous penetration into a volatile liquid. The data analysis results can be characterized on the following graphs: (1) multiple jet breakup length, normalized by the jet diameter, versus the Froude number, and (2) the ratio of normalized jet breakup lengths from the MFSBS-MJ experiments and the Saito correlation [9], versus the geometric spacing ratio. These graphs are presented in Figures 5-1 and 5-2, respectively.

In Figure 5-1, the breakup length data was plotted as a function of the Froude number, where

$$Fr = \frac{U_s^2}{g d_s} \qquad (10)$$

and U_s was the velocity at the coolant surface, taken to be constant over the breakup time. A simple power law ($y = Ax^b$) regression was done on the data and the resulting curve ($L/d = 7.46 * Fr^{0.44}$) is shown on the graph. The correlation coefficient for this fit was 0.80, indicating a reasonable fit of the data. The 'boiling' jet penetration length correlation from Saito et. al. [9] (see Eqn. 8) was also shown on this graph to provide a reference for evaluation of these results. For convenience, Figure 5-3 was included to show the test number corresponding to each data point.

The apparent applicability of the Saito correlation to the MFSBS-MJ data was further investigated by fitting the data to the parameters of the correlation (i.e.; normalized breakup length and square root of the density ratio and Fr), and determining a proportionality constant. This result is shown in Figure 5-4, where the independent axis is given as the Saito correlation without the leading coefficient. A linear regression curve fit was done, producing a slope (i.e.; proportionality constant) of 2.16. The correlation coefficient was 0.75.

An attempt was made to characterize the geometric spacing effects on the breakup length.

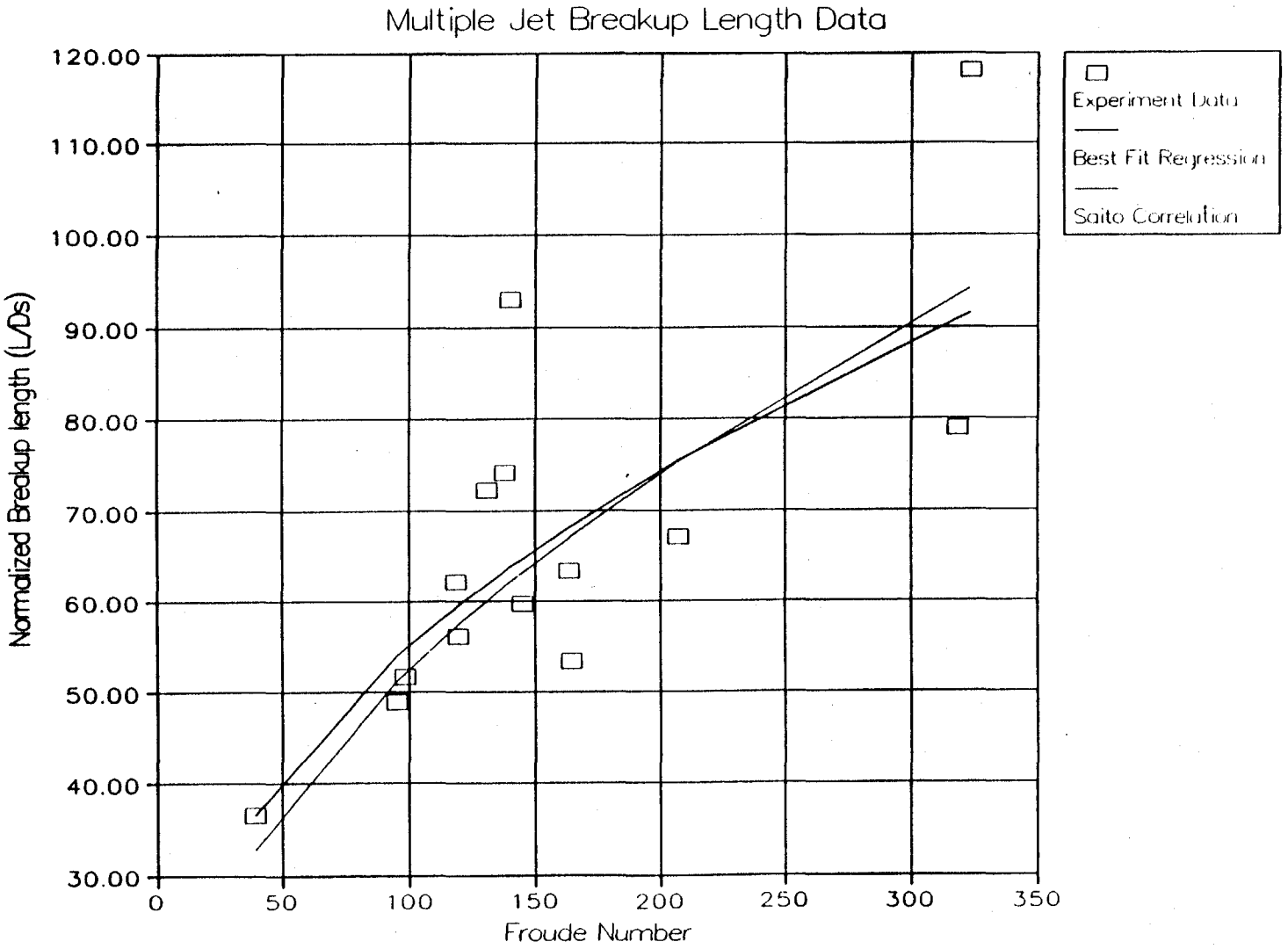

Figure 5-1: MFSBS-MJ Breakup Length Data

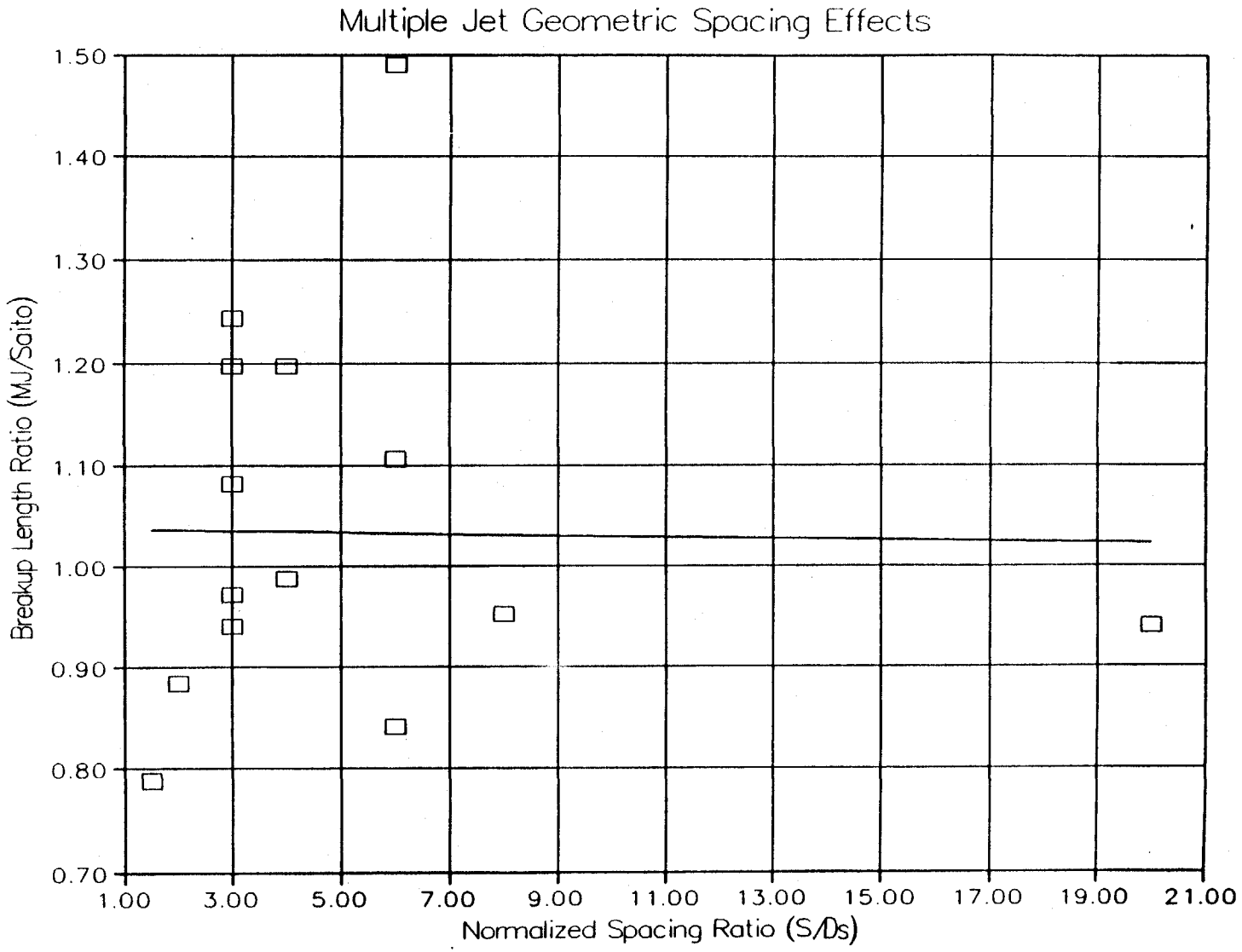

Figure 5-2: Geometric Spacing Influence on MFSBS-MJ Breakup Lengths

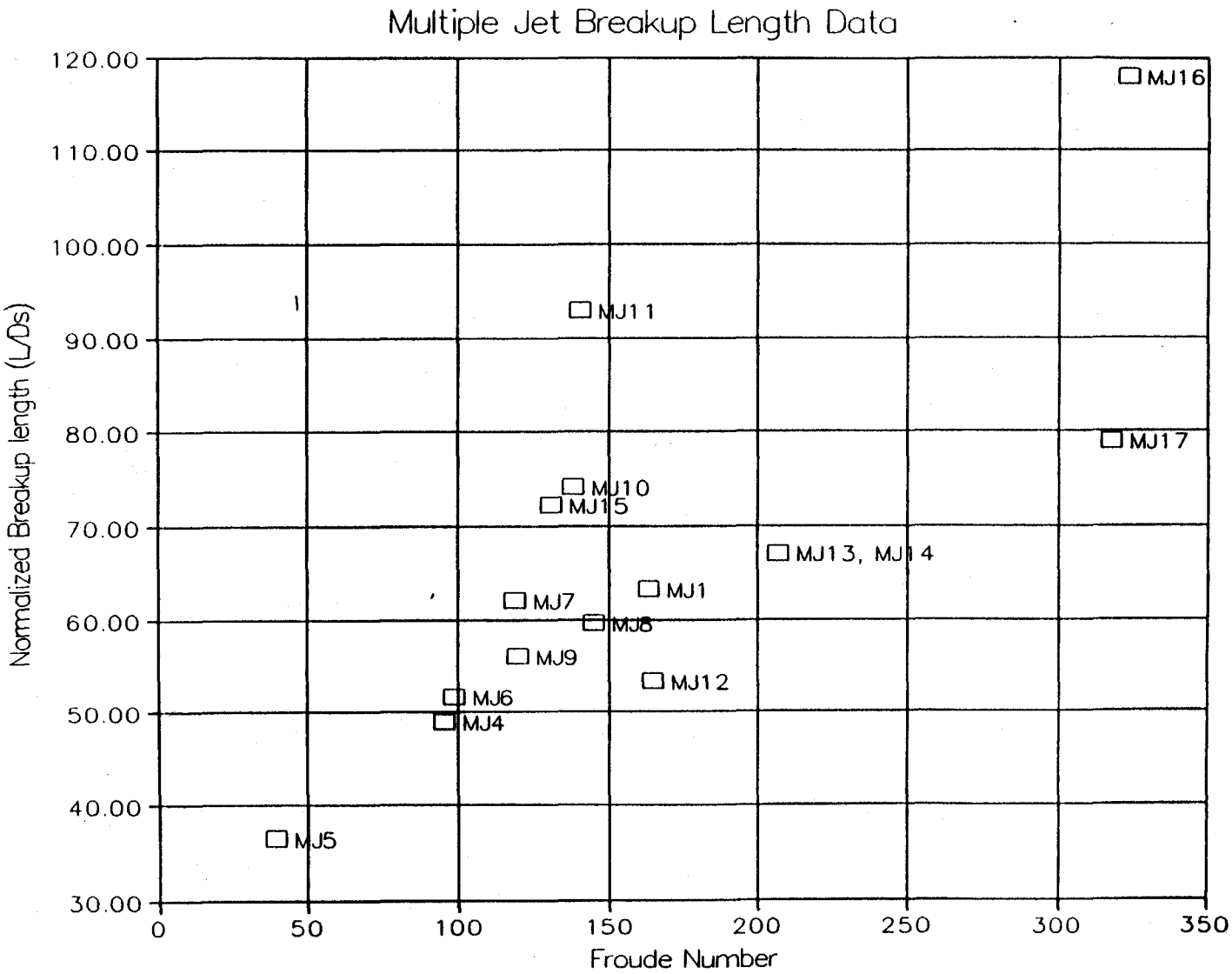

Figure 5-3: MFSBS-MJ Test Data Identification

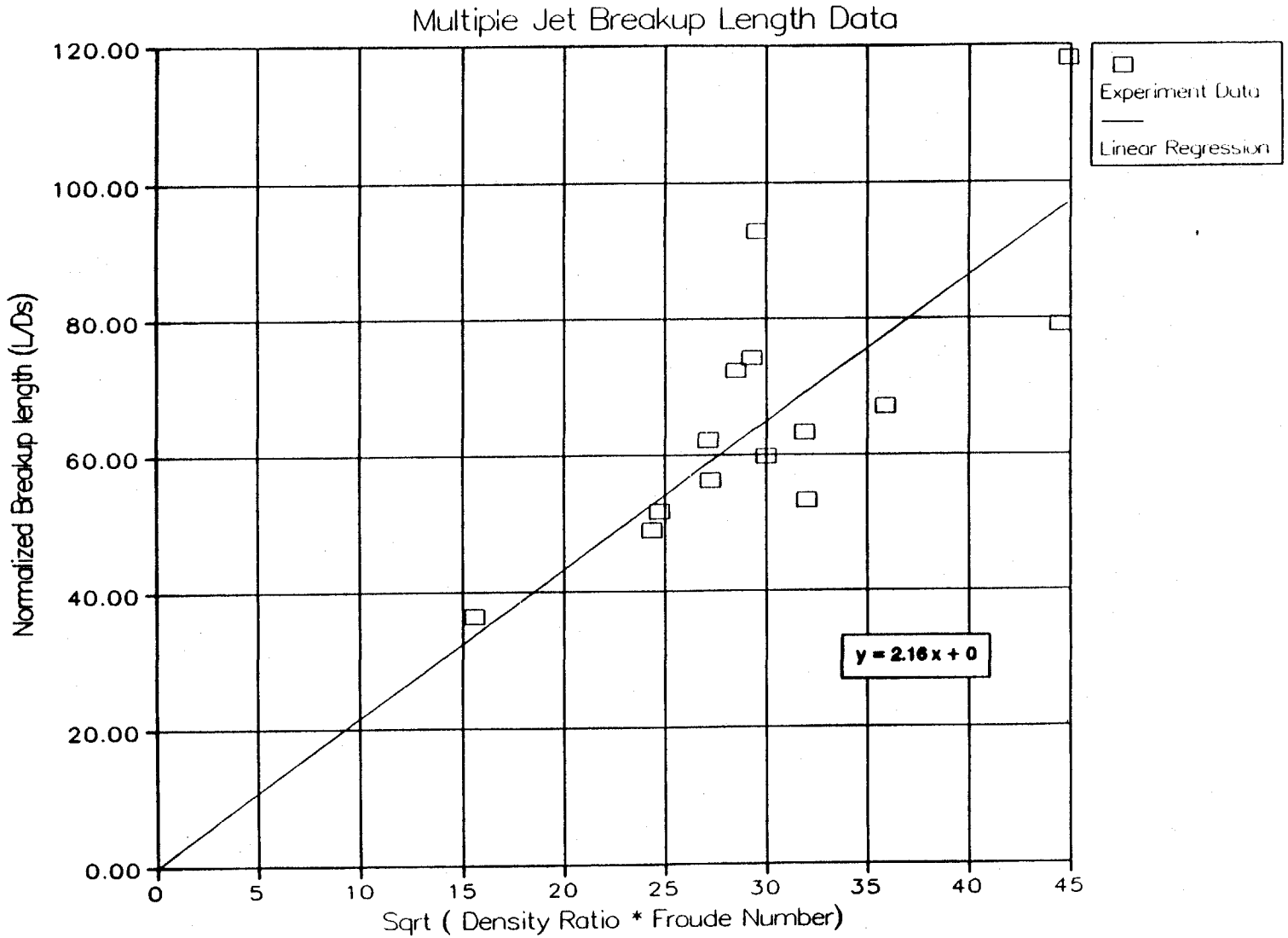

Figure 5-4: Proportionality Constant for MFSBS-MJ Data Fit to Saito Correlation

This is shown in Figure 5-2, where the ratio of the measured breakup length and the Saito correlation represents the dependent variable. The large scatter of data precluded any correlation. The anticipated trend of this graph was that the breakup length ratio would decrease asymptotically from a minimum spacing ratio to unity at large spacing ratios, implying no geometric spacing effects (this was observed in MJ1 where S/d was 20). The minimum spacing ratio could approach unity, implying that the nozzles be butted against each other. For this limiting case, the Saito correlation would use an effective diameter of the combined jet areas to predict the breakup length ratio. That is, in the limit as S/d approaches unity,

$$d_{eff} = \sqrt{3} * d_{single} \tag{11}$$

resulting in a predicted normalized breakup length of:

$$\frac{L}{d} = (3)^{\frac{1}{4}} * \left(\frac{L}{d}\right)_{single} \tag{12}$$

Thus, when Eqn. 11 is used to predict the breakup length for the limiting case, the resulting breakup length ratio (i.e.; the dependent variable in Figure 5-2) goes to 1.32 (i.e.; $3^{1/4}$).

5.1 Discussion

In the present section, the results of the MFSBS-MJ experimental investigation are discussed as they pertain to the project objectives. The objectives underlying this experimental investigation were to assess the influence of adjacent jets on the breakup length of a central jet in a one-dimensional array of molten metal jets simultaneously penetrating a volatile liquid. This was to be accomplished by comparison of the results to the current literature (i.e.; the Saito et. al. [9] empirical penetration length correlation) and by verification of predictions from the physical model

for the Saito correlation proposed by Schneider [10]. A final objective was to produce a relevant set of data to test, and assist in the development of, current jet fragmentation modelling for postulated severe core melt accidents.

The experiments conducted by Saito et. al. [9] considered a single water jet penetrating a coolant pool, where boiling was present due to the coolant material and the large temperature differences of the participating liquids. An empirical correlation for the penetration length was developed:

$$\frac{L}{d_j} = 2.1\sqrt{\frac{\rho_j}{\rho_c} Fr} \qquad (8)$$

A comparison of the Saito correlation to a power law curve fit of the MFSBS-MJ experimental data was shown in Figure 5-1. In this Froude number range, the data fit the Saito correlation well. The strong compatibility of the present data to the Saito correlation suggested that the presence of adjacent jets had little influence on central jet breakup lengths. This result was more qualitatively developed in Figure 5-4, where the proportionality coefficient of the present data, when plotted as a function of the parameters of the Saito correlation, was determined to be 2.16. The proportionality constants given by the Saito correlation and by Schneider [10] were 2.1 and 2, respectively.

Schneider [10] proposed a model to explain the empirical correlation given by Saito et. al. This 'boiling' jet breakup model assumed that the steady state pressure gradient in the coolant pool was the hydrostatic pressure. The vapor boundary layer of a jet was considered thin compared to the jet diameter, so that the total volume displaced by the jet was essentially that of the jet. This implied that, given a hydrostatic pressure gradient in the coolant pool at steady state, the breakup length of a single jet would be negligibly influenced by the presence of simultaneously penetrating

adjacent jets, since a jet's thin boundary layer would not influence adjacent jets. The MFSBS-MJ experimental results support the thin vapor boundary layer assumption, as seen in Figure 5-1, where the data is shown to correlate well with the single jet 'boiling' breakup length model.

The influence of the multiple jet spacing ratio on the breakup length was specifically considered in Figure 5-2, where a geometric spacing relationship was attempted. The large scatter of data precluded any correlation, which supported the previous results that no notable influence of adjacent jets on the breakup length of a central jet existed.

Recorded observations of the MFSBS-MJ experiments provided valuable information about the hydrodynamics of the melt-coolant interactions. Although detailed descriptions and photographs are presented in the previous sections, several significant observations are restated. Significant vapor, produced mainly at the jets' leading edge, enveloped the molten metal streams from the onset of coolant interaction. The jets became discontinuous well above the breakup length and the ultimate breakup mechanism, enhanced by the vapor counter-flow, was due to the stripping of drops and filaments along the jet columns and segments. This was presumed to be a result of Kelvin-Helmholtz instability. Fragmentation of the large segments by windward side instabilities (i.e.; due to Rayleigh-Taylor instability) was not apparent. Further evidence of this came from examination of the debris bed, where large solidified globules/segments had very irregular surfaces. The physical progression of the melt streams breakup appeared to follow previously observed jet breakup phenomena. The significant concentration of the larger debris near the center of the interaction vessel floor indicated that there was little mixing between the jets and the liquid coolant above the breakup length. There appeared to be interaction between the jets in several of the experiments, although, the influence on the breakup length was undetected.

6. SUMMARY

In the present experimental investigation Cerrobend metal and liquid Freon-11 were used to determine the influence of adjacent jets on the breakup length of a central jet in a one-dimensional array of molten metal jets simultaneously penetrating a volatile liquid. This was accomplished by performing a matrix of tests encompassing a 1.5 to 20 range of nozzle spacing-to-diameter ratios. Data on the melt-coolant interactions was generated by motion picture photography and flash radiography. The hydrodynamics of the multiple jet breakup mechanisms were observed and characterized. The data was shown to fit the single jet penetration length correlation by Saito et. al. [9] well, suggesting that the adjacent jets had negligible influence on the central jet. The data also verified the assumptions proposed in the 'boiling' jet breakup model by Schneider [10]. This physical model predicted the independent penetration of multiple molten metal jets into a volatile liquid based on a thin vapor boundary layer about the jets and in the presence of a continuous coolant depth. A relation between the geometric spacing ratio and the jet breakup length was investigated, although no correlation was found. This further suggested that multiple jet effects were negligible.

These results and the observed melt-coolant interactions will be useful in the assessment, and advancement, of current computer models that simulate molten corium migration during postulated core melt accidents.

7. RECOMMENDATIONS FOR FURTHER WORK

The MFSBS-MJ experimental investigation provided a base set of data to assist in the understanding of the breakup mechanisms for multiple molten metal jets penetrating a volatile liquid. This database can be expanded in the following areas:

(1) The 1-dimensional nature of these experiments may have prevented the complete shrouding of the central jet, thereby prohibiting the freefall of the central jet and allowing leading edge erosion to effect the breakup. This issue may be addressed by the development of two-dimensional arrays of jets to investigate vapor crossflow effects and suspected bending of the peripheral jets.

(2) The observation of no spatial effects on the breakup length may suggest that something is missing in the present model. Possibly, the large amount of vapor generated among the jets diminishes the spacing effects. This issue may be addressed by utilizing subcooled coolant to restrict the vapor generation about the jets, which may reveal some spatial dependence.

(3) Expanding the Froude number range and increasing the temperature difference between the simulant materials may be done to test the limitations of the current 'boiling' jet breakup length model.

(4) The leading edge mechanisms and effects of jet interactions (i.e.; instabilities) were difficult to characterize due to the inability of the data recording mechanisms to capture them. Clarification of these phenomena may be obtained by utilization of cine-radiography to enhance the hydrodynamic observations within the vapor channel at the jets' leading edge.

REFERENCES

1. Nuclear Engineering International, Vol. 15, No. 167, p.344; April 1970.

2. J. L. Rempe, G. L. Thinnes, and C. M. Allison, "Light Water Reactor Lower Head Failure Analysis," Draft, NUREG/CR-5642, EGG-2618 (Draft); December 1990.

3. K. M. Becker, J. Engstrom, and R. V. MacBeth, "Enhancement of Core Debris Coolability," KTH-NEL-51, Department of Nuclear Reactor Engineering, Royal Institute of Technology, Stockholm, Sweden; May, 1990.

4. M. A. Abolfadl, and T. G. Theofanous, "An Assessment of Steam Explosion Induced Containment Failure. Part II: Premixing Limits," Nuclear Science and Engineering, 97, p. 282; 1987.

5. D. F. Fletcher, and R. P. Anderson, " A Review of Pressure-Induced Propagation Models of the Vapor Explosion Process," Progress in Nuclear Energy, Vol. 23, No. 2, p. 137; 1980.

6. T. G. Theofanous, "Thermo-Fluid Science in Severe Nuclear Accidents," ANS Proc. 1989 National Heat Transfer Conf., Philadelphia, PA, p. 3; August 6-9, 1989.

7. J. P. Schneider, "Breakup of Metal Jets Penetrating a Volatile Liquid," PhD Thesis, University of Illinois at Urbana-Champaign; In Preparation.

8. S. K. Wang, C. A. Blomquist, B. W. Spencer, L. M. McUmber, and J. P. Schneider, "Experimental Study of the Fragmentation and Quench Behavior of Corium Melts in Water," 5th Proc. of Nuclear Thermal Hydraulics, ANS Winter Mtg., San Francisco, CA; November 26-30, 1989.

9. M. Saito, K. Sato, and S. Imahori, "Experimental Study on Penetration Behaviors of Water Jet into Freon 11 and Liquid Nitrogen," ANS Proc. 1988 National Heat Transfer Conf., Houston, TX; July 24-27, 1988.

10. J. P. Schneider, M. J. Marciniak, and B. G. Jones, "Breakup of Metal Jets Penetrating a Volatile Liquid," Topical Meeting on Nuclear Reactor Thermal Hydraulics (NURETH-5), Salt Lake City, UT; September 21-24, 1992.

11. D. F. Fletcher, and A. Thyagaraja, "The CHYMES Coarse Mixing Model," Progress in Nuclear Energy, Vol. 26, p. 31; 1991.

12. T. Ginsberg, "Liquid Jet Breakup Characterization with Application to Melt-Water Mixing," Proc. International ANS/ENS Topical Meeting on Thermal Reactor Safety, San Diego, CA, Vol. 5, p. II.4-1; Feb. 2-6, 1986.

13. Grant, R. P., and S. Middleman, "Newtonian Jet Stability," AIChE Journal, Vol. 12, No. 4, p. 669; July, 1966.

14. Taylor, G. I., "The Dispersion of Jets of Metals at Low Melting Point in Water," (1942) in G. K. Batchelor, The Scientific Papers of G. I. Taylor, Vol. 3, Cambridge University Press, Cambridge, MA; 1963.

15. H. J. Hoyt, and J. J. Taylor, "Waves on Water Jets," J. Fluid Mechanics, Vol. 83, Part 1, p.119; 1977.

16. G. De Jarlais, M. Ishii, and J. Linehan, "Hydrodynamic Stability of Inverted Annular Flow in an Adiabatic Simulation," ASME Transactions, Vol. 108, p. 84; 1984.

17. M. Epstein, and H. K. Fauske, "Steam Film Instability and the Mixing of Core-Melt Jets and Water," ANS Proc. 1985 National Heat Transfer Conf., ANS #700101, Denver, CO, p. 277; August 4-7, 1985.

18. B. W. Spencer, J. J. Sienicki, and L. M. McUmber, "Hydrodynamics and Heat Transfer Aspects of Corium-Water Interactions," EPRI NP-5127; March, 1987.

19. J. D. Gabor, B. W. Spencer, and J. C. Cassulo, "Simulant Material Pour Stream Breakup Tests and Model Implications," ANL Technical Memorandum ANL-IFR-77; August, 1987.

20. E. I. Du Pont De Nemours and Company, Inc., "Thermodynamic Properties of Freon 11 Refrigerant," E. I. Du Pont De Nemours and Company, Wilmington, Delaware; 1965.

21. Literature from Cerro Copper and Brass Company, Bellefonte, PA.

APPENDIX A. Design Specification for Furnace/Pour Assembly

Design Specification
MFSBS-MJ
Furnace/Pour Assembly
Phase I

See Figures #1 and #2 for scaled drawing of furnace/pour assembly.

Comments: unless otherwise noted, material thicknesses shown in the figures are nominally taken as 3/8".
unless otherwise noted, dimensions and thicknesses do not require "precise" reproduction.
utilize materials that are most readily available.

Part **#1**: Piston/cylinder assembly

Existing piston/cylinder:
1" dia.; 8" total length
5/8" threaded nose piece, 1/2" length
5/16" dia. SS rod, threaded, protrudes 1/2" at tdc
4" stroke

New base plate:
See Figure #3
1/4" * 9 1/2" dia.; SS
(12) 11/32" dia. bored holes, 8 13/16" B.C., 30 degrees
(2) 1/4" dia. NPT holes, 4 1/2" B.C., 180 degrees
(2) "U" shaped SS handles welded to top of plate;
1" height, 2" length; 4 1/2" B.C., 180 degrees;
offset 90 degrees from NPT holes
(1) 5/8" dia. bored hole, center, threaded (to accept nose of cylinder)

New cutter:
See Figure #4
1 7/8" O.D. * 2" length SS cylinder
1/16" wall thickness
30 degree cut at bottom
sharpen angled edge
weld (3) 3" length, 1/8" dia., angled SS wires to inside wall of cutter at 1/2" from top, 120 degrees

New rod:
See Figure #4
5/16" dia.; SS
fabricate threaded adapter to connect to existing rod
weld SS wires from cutter to rod at 1/2" from bottom

Part #1 (continued):

Comments: rod length will be specified after other parts are fabricated.
minimize flow obstruction at the cutter.
initial cutter position (lowest point) to be at 2" above diaphragm.
cutter tip - rod positioning **to be maintained** as shown in Figure #4.

Part #2: **New** upper furnace (see Figure #2)

New upper flange: 9 1/2" O.D.; Aluminum
(12) 11/32" dia. bored holes, 8 13/16" B.C., 30 degrees
7" I.D.

New lower flange: 9 1/2" O.D.; Aluminum
(12) 11/32" dia. bored holes, 8 13/16" B.C., 30 degrees
7" I.D.

New spool section: 7" I.D.; Aluminum
6" height
30 degree angled Al nozzle at base of spool; securely mount to spool and lower flange (heat shrink fit)
(8) 1/4" NPT holes at 1" below top of spool, 45 degrees

Comments: good surface contact is necessary between the nozzle and the spool.
heating system is currently being investigated.
chamfer nozzle near 2" I.D. dimension.
provide (1) high temperature gasket to match upper flange geometry.

Part #3: **New** insulation flange (see Figure #2)

3/4" * 9 1/2" O.D.; SS
6" I.D.
(12) 11/32" dia. bored holes, 8 13/16" B.C., 30 degrees
(2) 1/8" dia. bored holes along width of flange, 180 degrees; offset from vertical holes

Comments: provide (2) high temperature gaskets to match flange geometry.

Part #4: **New** lower furnace (see Figure #5)

New upper flange:
9 1/2" dia.; Aluminum
(12) 11/32" dia. bored holes, 8 13/16" B.C., 30 degrees
2" I.D.

New lower flange:
3 1/8" dia. (**maintain this dimension**); Aluminum
(8) 5/32" dia. SS studs, 3/4" length, 2 3/4" B.C.
45 degrees, threaded
1 mm countersink, 2 1/4" O.D.
2" I.D.

New spool section:
15" length, Aluminum
2" I.D.

Comments: heating system is currently being investigated.

Part #5: **New** diaphragm holder (see Figure #2)

New upper flange:
3 1/8" dia. (**maintain this dimension**); Aluminum
(8) 5/32" dia. bored holes, 2 3/4" B.C., 45 degrees
1.0 mm raised surface, 2 3/8" O.D.
2" I.D.

New lower flange:
3 1/8" dia. (**maintain this dimension**); Aluminum
(8) 5/32" dia. bored holes, 2 3/4" B.C., 45 degrees
2" I.D.

New spool section:
1 1/2" height, Aluminum
2" I.D.
2 3/8" O.D. (**maintain this dimension**)

Comments: overall length of diaphragm holder must be at least 2 1/4".

Part #6: **New** nozzles - for continuation of single jet experiments (see Figure #2)

New upper flange: 3 1/8" dia. (**maintain this dimension**); Aluminum
(8) 5/32" dia. bored holes, 2 3/4" B.C., 45 degrees
2" I.D.

New spool section: 2 3/4" height; Aluminum
bore desired diameter hole up to 3/4" from bottom
2 3/8" O.D. (**maintain this dimension**)

Comments: (4) separate nozzles are required: 1/8", 1/4", 1/2", and 3/4" dia.
top of upper flange is at 2" I.D.; neck down to desired diameter at 3/4" from bottom.
Chamfer intersection - **it is important that there is a very smooth transition at the intersection.**

Part #7: Existing furnace mounting plate/tee (see Figure #1)

Part #8: Existing apparatus' frame (see Figure #1)

Part #9: Existing interaction vessel (see Figure #1)

Notes:

high temperature gaskets can be punched at ANL.
TC, PT, and Ar ports must be plugged.
provide sufficient thread length on all studs to ensure securely bolted parts.
diaphragm material to be 2-3 mil Brass/SS, 2 3/8" O.D.
provide (12) 11/32" bolts, 1 1/2" length, and associated nuts and washers.
provide (12) 11/32" bolts, 3" length, and associated nuts and washers.
provide (8) 5/32" bolts, 1 1/4" length, and associated nuts and washers.
provide (8) nuts and washers to accommodate 5/32" dia. studs.

FIGURE #1:
MFSBS-MJ
FURNACE/POUR ASSEMBLY

SCALE: 1/4" = 1"
@ 90 PHOTOCOPY REDUCTION

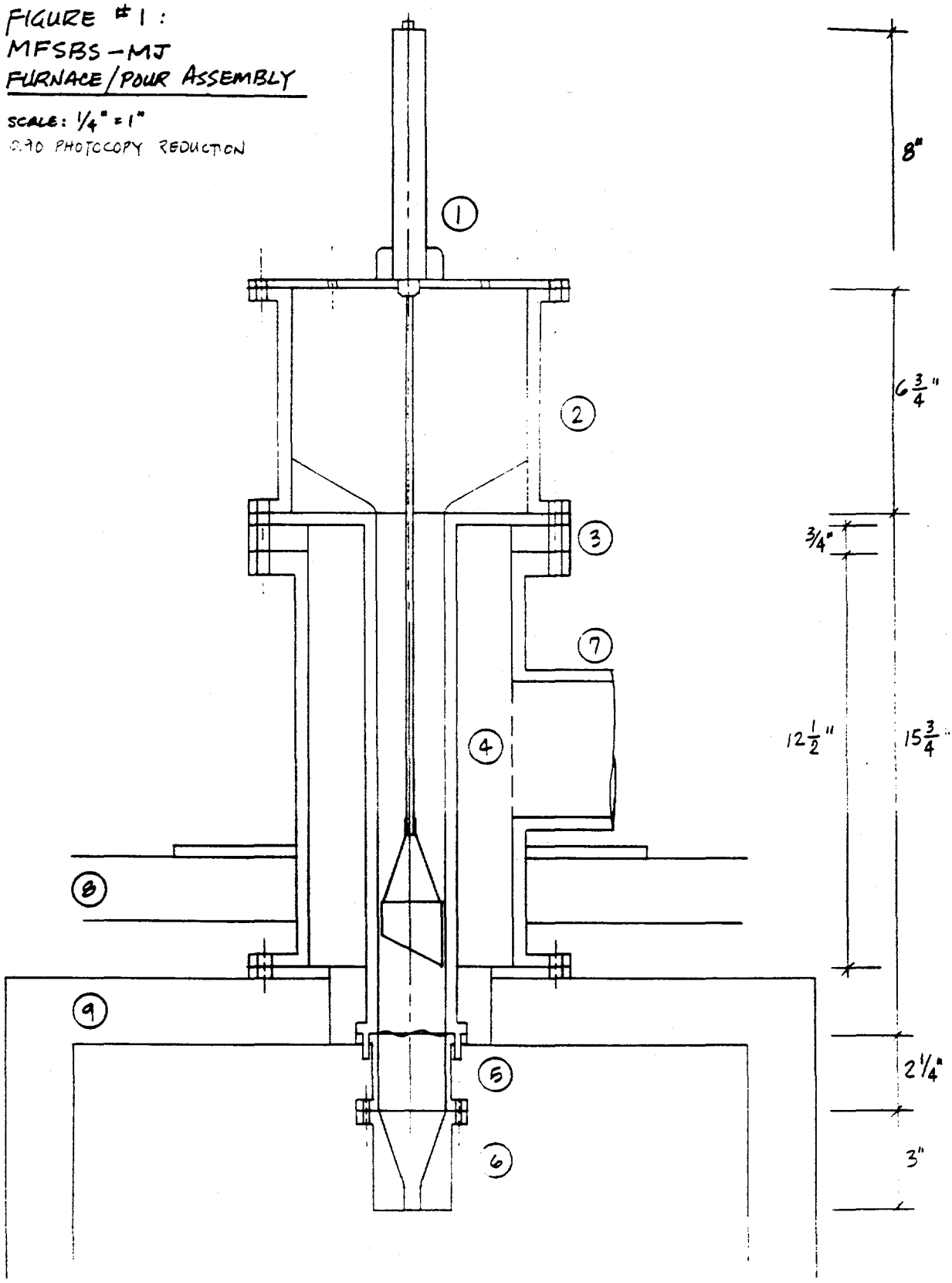

FIGURE # 2:
FURNACE/POUR DETAIL

SCALE: 1/2" = 1"
@ 90% PHOTOCOPY REDUCTION

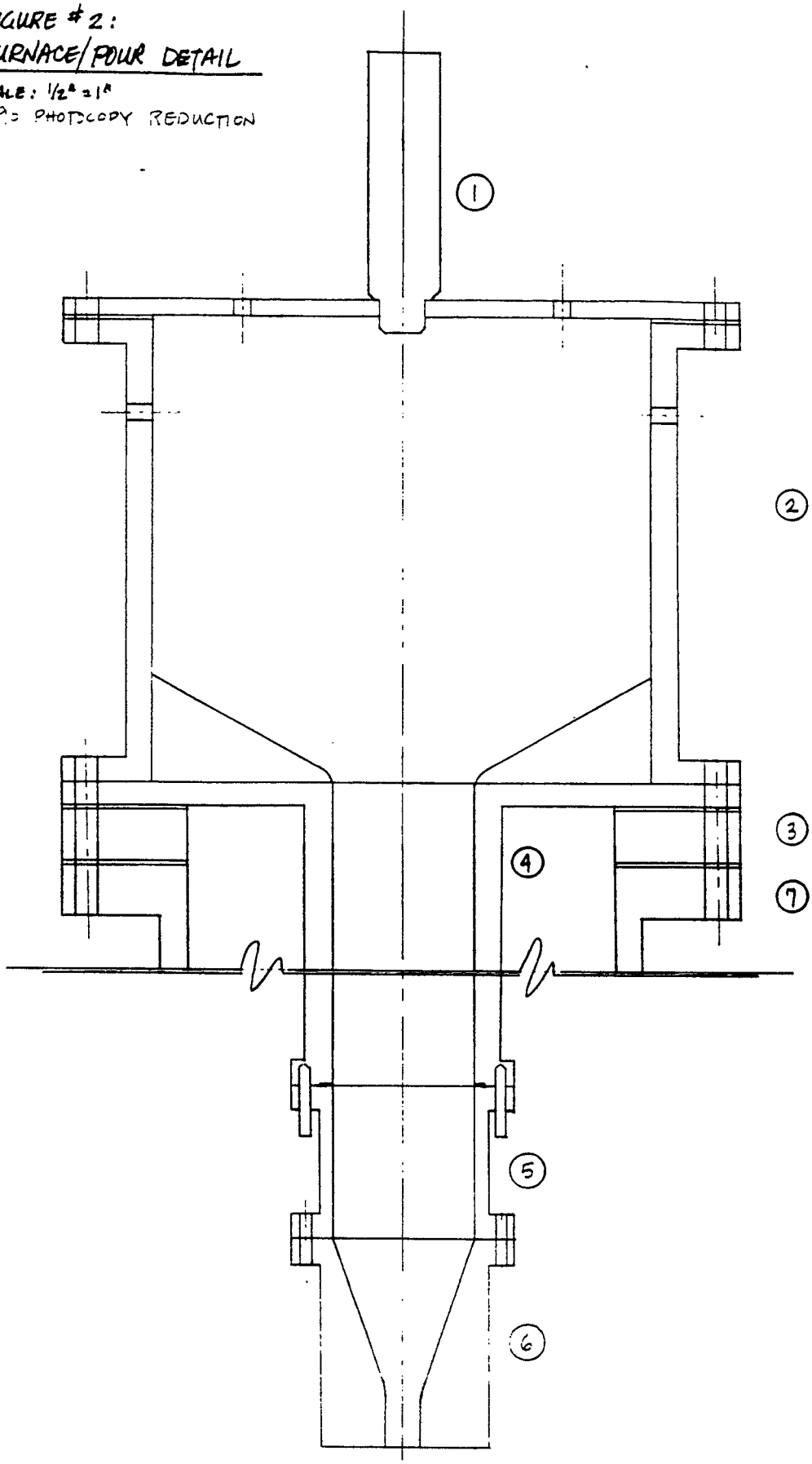

FIGURE #3:
PISTON/CYLINDER BASE PLATE

SCALE: 1/4" = 1"
C.90 PHOTOCOPY REDUCTION

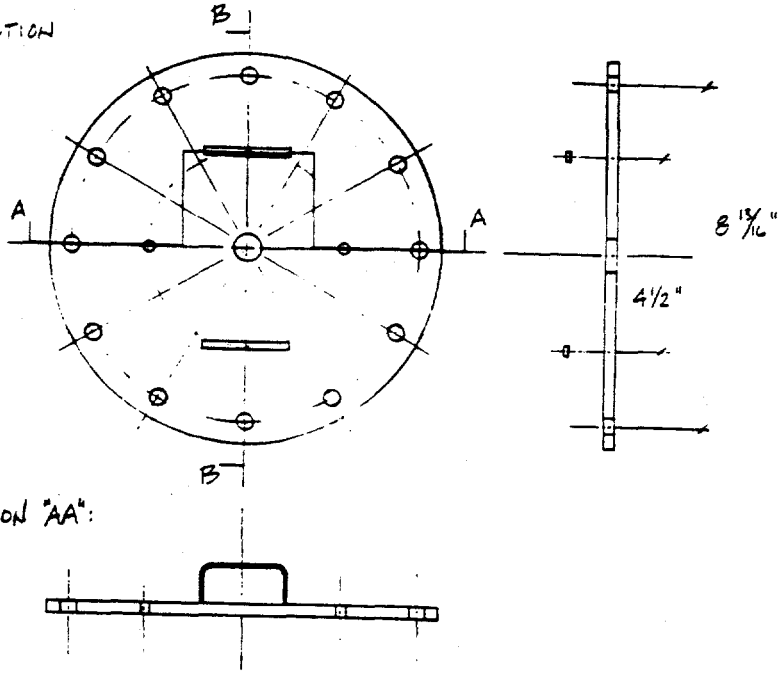

FIGURE #4:
DIAPHRAGM CUTTER

SCALE: 1/2" = 1"
C.90 PHOTOCOPY REDUCTION

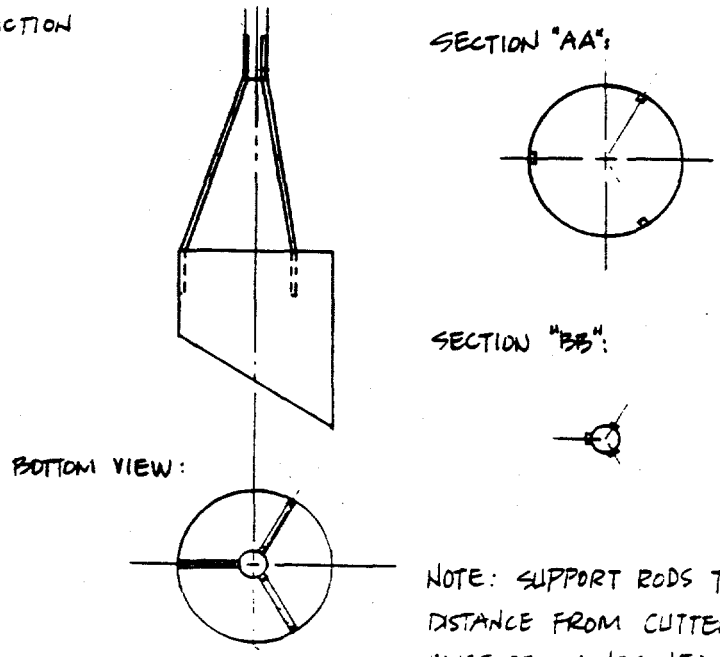

NOTE: SUPPORT RODS TO BE EQUAL DISTANCE FROM CUTTER TIP. THIS MUST BE MAINTAINED IN FABRICATION.

FIGURE #5:
LOWER FURNACE

SCALE: 1/2" = 1"
0.90 PHOTOCOPY REDUCTION

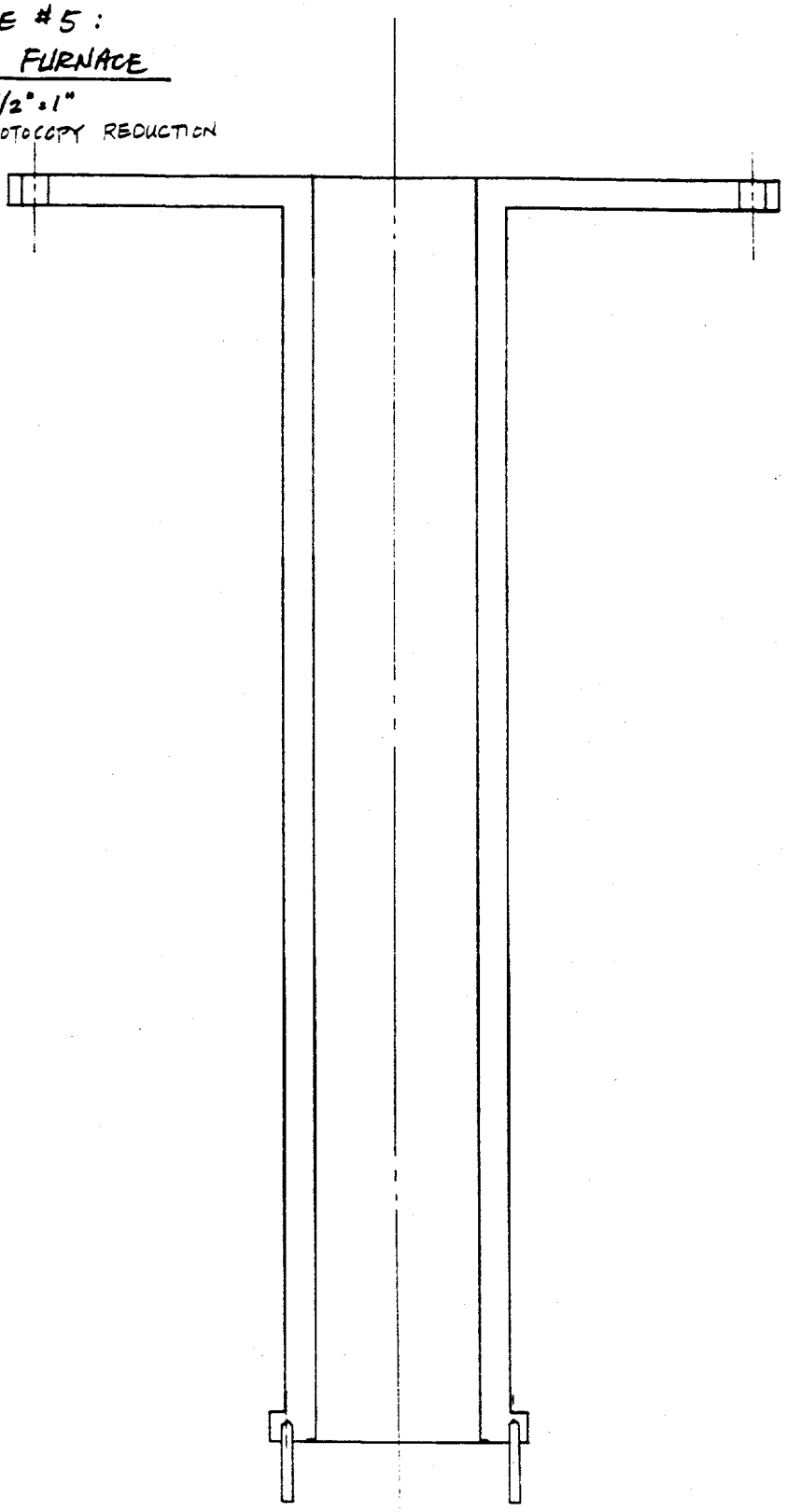

APPENDIX B. Experimental Procedure Checklist

Test Designation: MFSBS-_____
Date: ___-___-92

MFSBS PROCEDURE CHECKLIST (revised 6-2-92)

Pre-test Apparatus Preparations

_____ Connect 440 Vac power supply to Variac cabinet.
_____ Connect 110 Vac power supply to Variac cabinet.
_____ Connect 110 Vac power supply to timer cabinet.
_____ Switch on electronic cold junctions; check batteries.
_____ Setup Visicorder (____ same as previous test).
_____ Load particulate metal into furnaces. Energize furnaces.
_____ Cue videotape; check positioning of video camera.
_____ Verify MV-1, -9, and -10 are open.
_____ Measure chilled freon volume; record in test specs.
_____ Load Hycam films.
_____ Verify these connections: 110 Vac power supplies to timer, Hycams, and solenoid valve; synchronizer to Hycam #1.
_____ Open low pressure Ar isolation valves.
_____ When melted, spoon oxide layer from furnace; mount diaphragm cutter; connect Ar supply hose to piston/cylinder.

Pre-test X-ray System Preparations

_____ Connect 110 Vac power supply to control cabinet.
_____ Connect wiring from control cabinet to generator.
_____ Open Nitrogen gas cylinder valve.
_____ Set Marx generator Nitrogen pressure to 25 psig.
_____ Set x-ray time delay; record in test specs.
_____ Place x-ray film cassette on interaction vessel and align x-ray tube; record positioning in test specs.
_____ Turn on x-ray control cabinet and high voltage power (**do not** insert key); check x-ray interlocks by opening each of three interlocked doors and verifying that the circuit opens; de-energize x-ray cabinet.

Interaction Vessel Fill

_____ Turn on local ventilation blower and fume hood fan.
_____ Raise freon barrels.
_____ Align valves as follows: MV-2, -4, -8, and -11 closed; MV-5 and -6 opened (MV-3, and -7 not used).
_____ Connect fill/drain and Ar supply hoses to freon barrel.
_____ Fill interaction vessel by throttling MV-2.
_____ Close MV-2, -5, and -6.
_____ Lower freon-11 barrels.
_____ Fill Ar reservoir to 80 psig.

Melt Injection

____ Verify TC-1a, -1b, and -1c trendicator readings are stable between 100 and 110 deg C; record in test specs.
____ Record TC-mj and ambient temperature trendicator readings in test specs.
____ Open MV-8.
____ Close MV-8 when interaction vessel pressure is stabilized.
____ Record interaction vessel coolant depth (137.5 cm - distance from top of vessel) in test specs.
____ Move exhaust hose to chilled freon location.
____ Attach chilled freon container and open MV-11.
____ Energize floodlights; check positioning.
____ De-energize furnaces.
____ Pressurize furnace via regulator at low pressure Ar supply.
____ isolate furnace.
____ **Evacuate room C-111.**
____ Start video recording.
____ Close interlock circuit.
____ Turn on x-ray cabinet power.
____ Insert key and turn on key switch.
____ Turn on POWER switch.
____ Turn the HIGH VOLTAGE CONTROL to zero.
____ Press the HIGH VOLTAGE ON button on the high voltage power supply and advance the HIGH VOLTAGE CONTROL until the meter reads 29 kV.
____ Manually start visicorder.
____ Manually start Hycams.
____ Manually energize timer for melt injection and x-ray delay generator.

____ Turn off POWER switch.
____ Turn off x-ray control cabinet power.
____ Re-enter room C-111; de-energize floodlights.
____ Close MV-11 after interaction vessel's pressure is stabilized.
____ Remove chilled freon container.
____ Turn off electronic cold junctions.
____ Reset visicorder, Hycams, and timer control switches.
____ Close x-ray Nitrogen cylinder valve.

Interaction Vessel Drain

____ Open MV-5 and -6.
____ Open MV-2 to drain interaction vessel.
____ Close MV-2, -5, and -6.
____ Isolate low pressure Ar supply.
____ Disconnect hoses from freon barrel.
____ Open MV-8.
____ Turn off local ventilation blower and fume hood fan.

Test Specification

Nozzle spacing: ____ 5" ____ 3" ____ 1 1/2" ____ 3/4"
Nozzle diameter: ____ 1/2" ____ 3/8" ____ 1/4"

X-ray time delay: _____ sec
X-ray cassette position: _____
_____

Chilled freon volume: pretest _____ ml
posttest _____ ml

Melt temperature: TC-1a _____ deg C TC-1b _____ deg C
TC-1c _____ deg C

Other temperatures: TC-ambient _____ deg C TC-mj _____ deg C

Freon liquid depth: _____ cm

Total debris mass: _____ g

Special test objectives: _____
_____
_____
_____

Comments regarding x-ray film development: _____
_____
_____
_____

Comments regarding experimental procedure: _____
_____
_____
_____
_____
_____
_____
_____
_____
_____
_____

GRC VISICORDER RECORD FORM

TEST MFSBS - MJ11 TEST DATE 5-1-92

PERSON RESPONSIBLE FOR DATA RECORDING MARCINIAK

VISICORDER # 18680 SET UP FOR IN INPUT ____ VDC X SC

Y	Power on Main Chassis	X	Timeline Post AUTO
N/A	Power on Amp Chassis	X	Grid Line Post INTD
X	New Paper Roll	X	Timer Post 20 sec
X	Start ____ Local X Remote	X	Speed 4 In/Sec = 1

Zero Input Record X Yes ____ No

Full Scale Record ____ Yes X No

Ref Data Record X Yes ____ No

VISC CE	ID	AMP MODULE	SENS V/DIV	TRACE Y	SEQ/PAR POST	REF DATA	NOTES
2	TC-2B		0.01	4	PAR		IV-top
4	TC-4B		0.01				IV - middle
6	TC-5B		0.01				REMOVED
8	TC-8B		0.01				Expansion Volume
10	TC-11A		0.01				Freon Condenser
12	TC-11B		0.01				Freon Condenser
14	PT-1		0.1				top furnace
16	PT-2B		0.1				IV
18	PT-7A		0.1				Expansion Volume

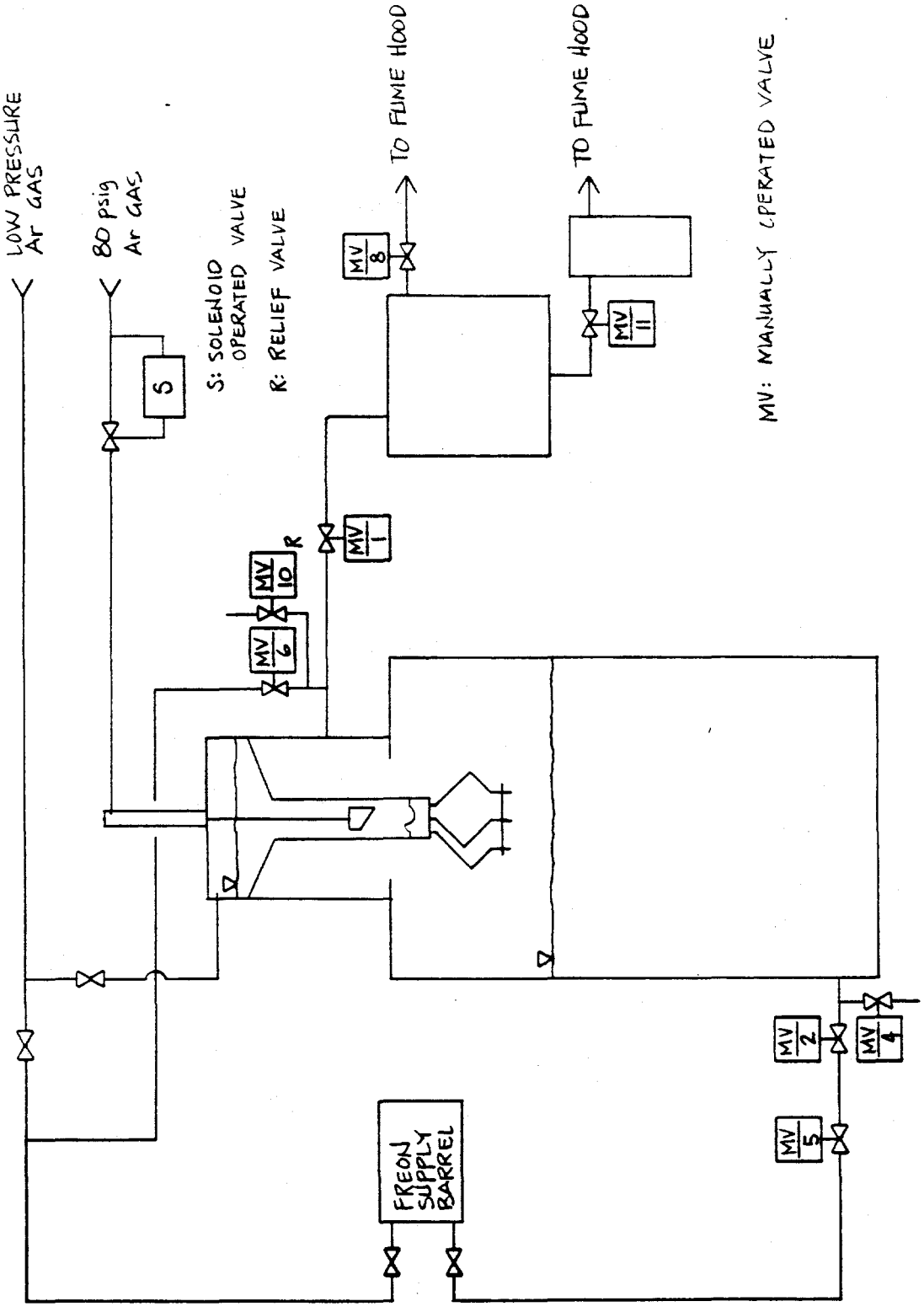

Schematic Diagram of MFSBS-MJ Experimental Apparatus
Depicting Gas/Coolant Supply and Control

OSCILLOGRAPH	
Channel	Input
2	TC-2B: vessel, top
4	TC-4B: vessel, middle
8	TC-8B: expansion volume
10	TC-11A: condenser, middle
12	TC-11B: condenser, bottom
14	PT-1: furnace, top
16	PT-2B: vessel, top
18	PT-7A: expansion volume

Oscillograph Data Input Connections
Primary Voltage: 110 Vac

TRENDICATOR	
Channel	Input
2	TC-1A: furnace, top
3	TC-1B: furnace, middle
5	TC-1C: furnace, bottom
7	TC-MJ: mj piping system
ambient	laboratory temperature

Trendicator Data Input Connections
Primary Voltage: 110 Vac

VARIAC POWER CABINET	
Variac Channel	Supplies
1	lower furnace
2	upper furnace
3	lights
4	lights
5	lights
6	lights
7	lights
8	lights
9	mj piping system
10	trendicator
11	oscillograph
12	digital voltmeter

Variac Power Cabinet Connections
Primary Voltage: 440 Vac, 110 Vac

APPENDIX C. Oscillograph Traces

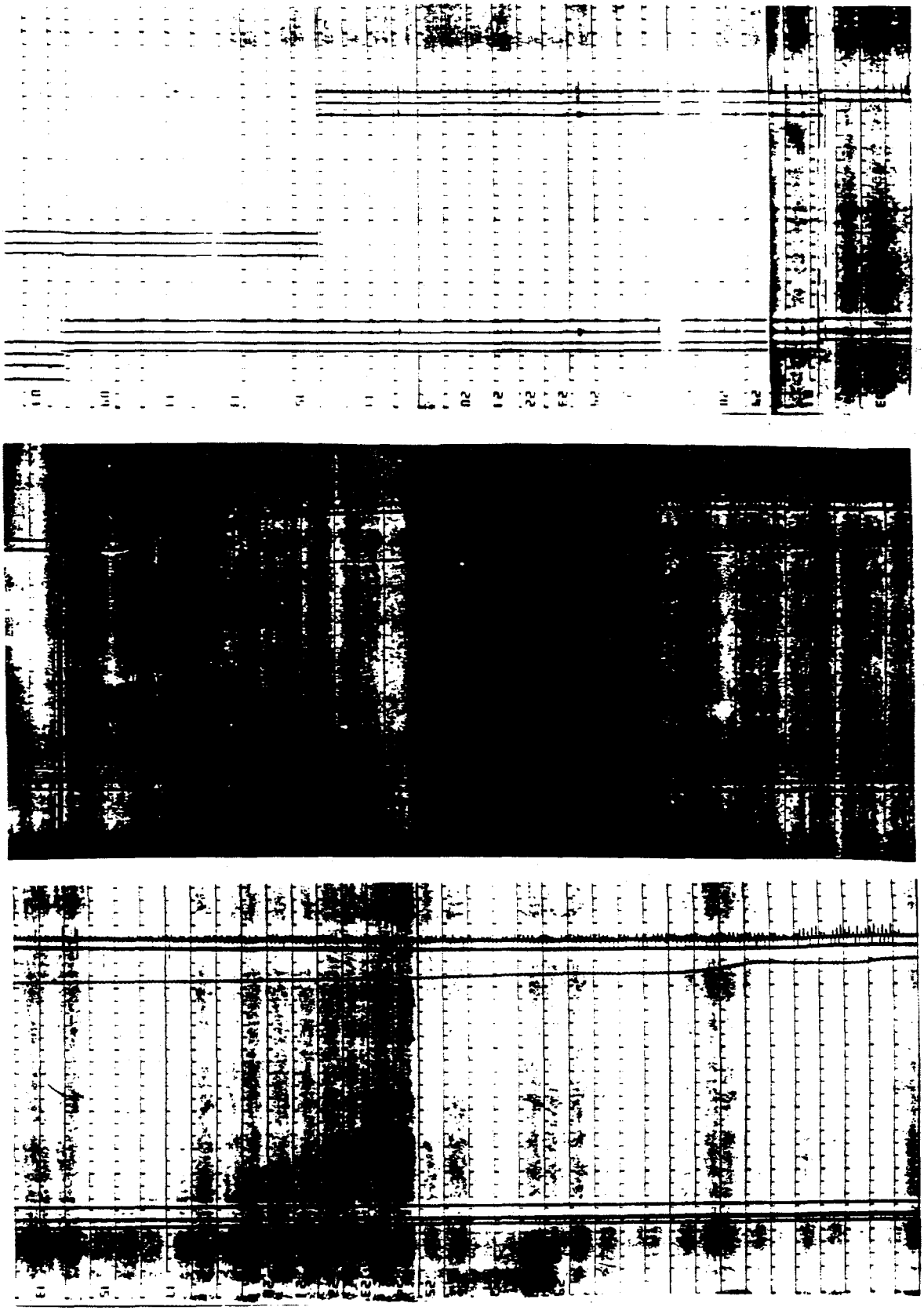

Oscillograph Trace - MFSBS-MJ1

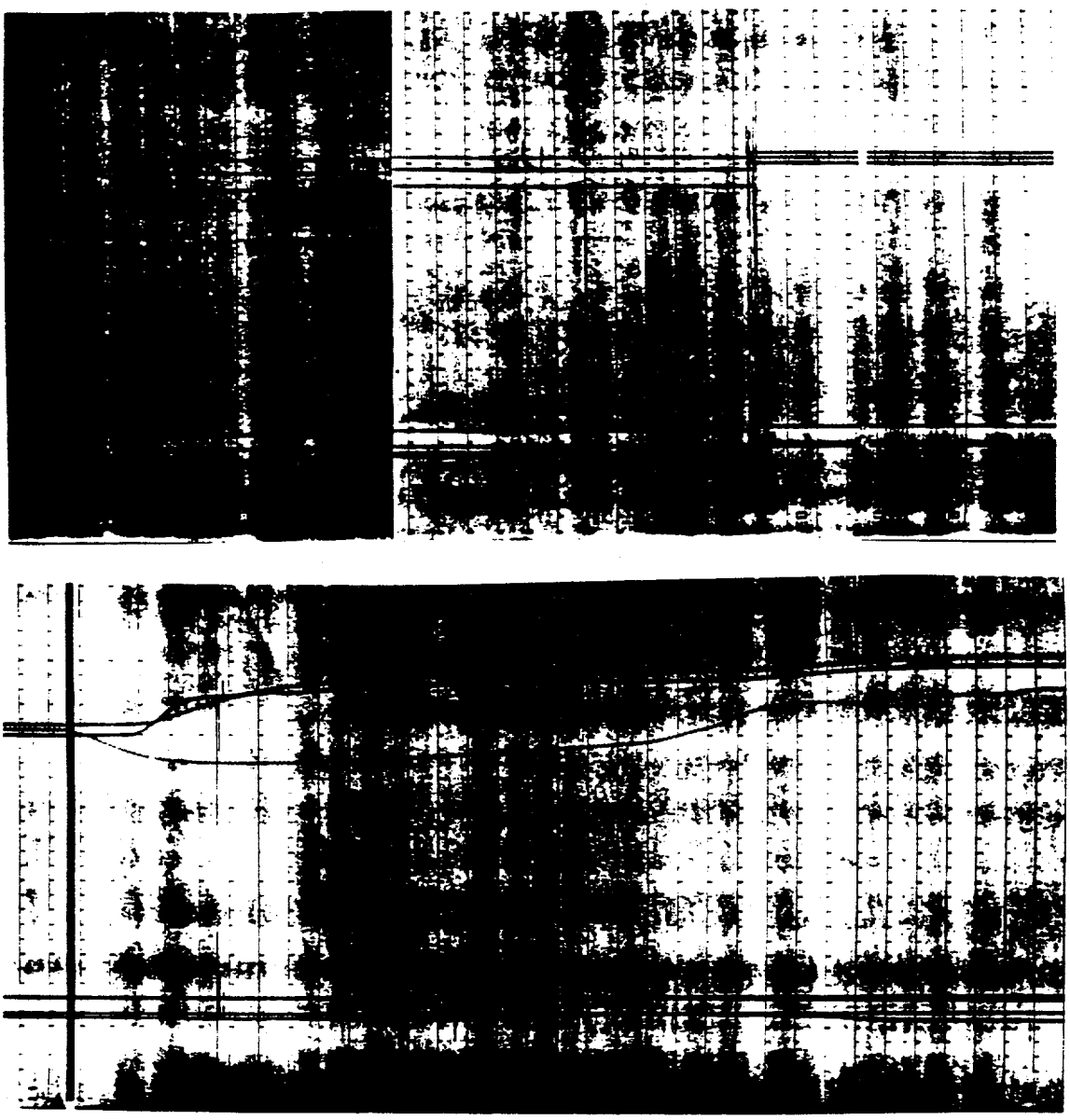

Oscillograph Trace - MFSBS-MJ2

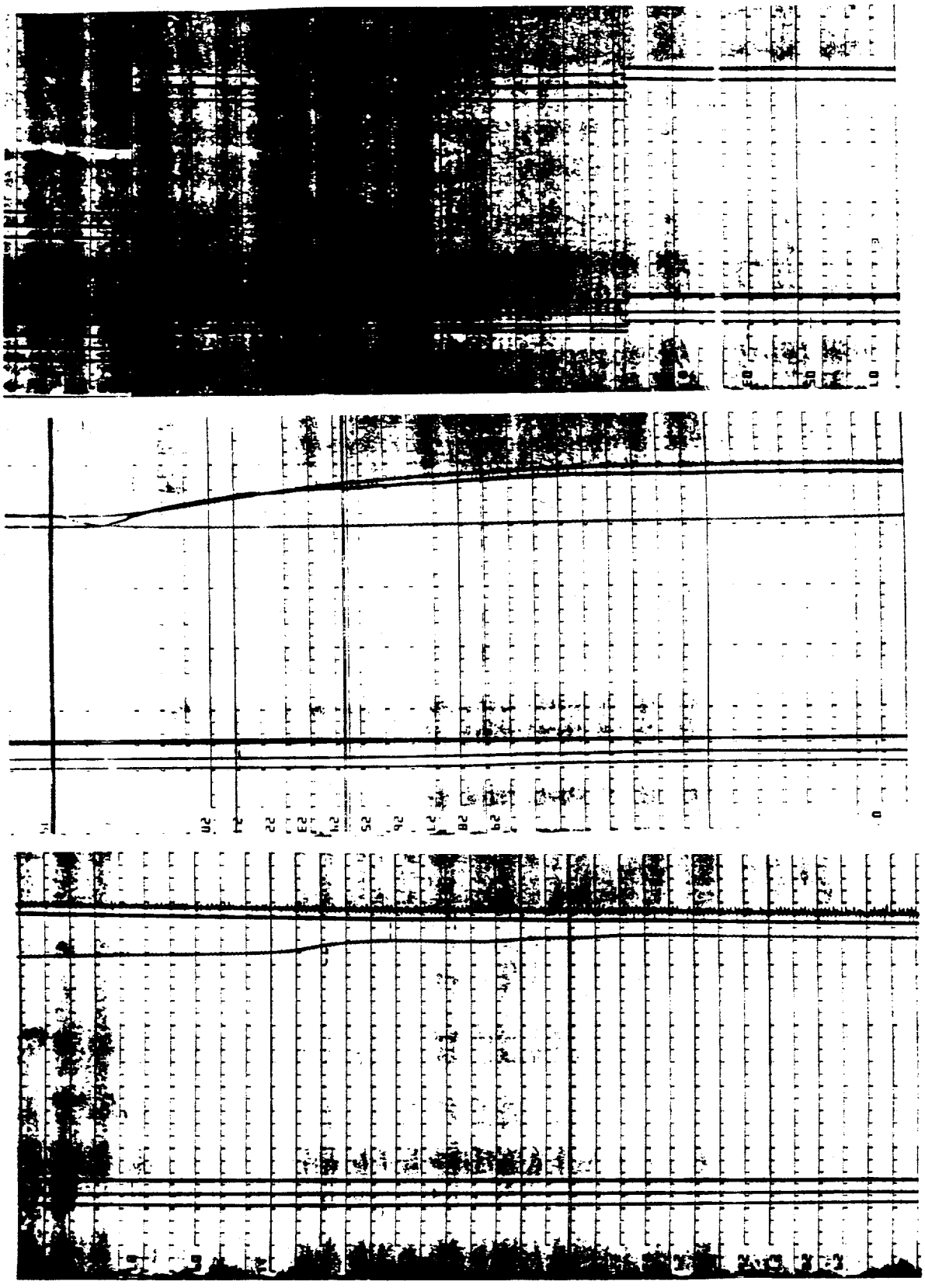

Oscillograph Trace - MFSBS-MJ3

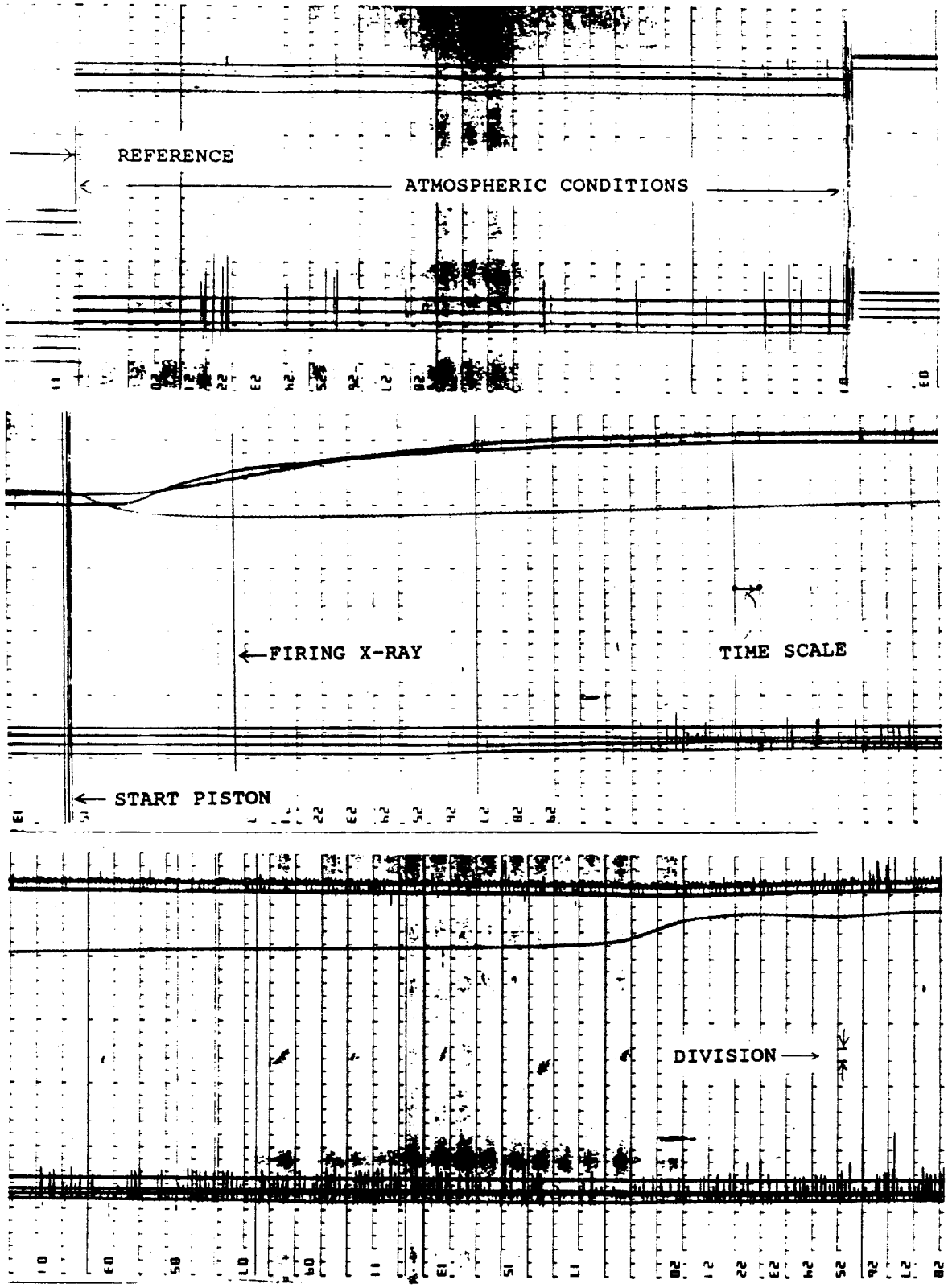

Oscillograph Trace - MFSBS-MJ4

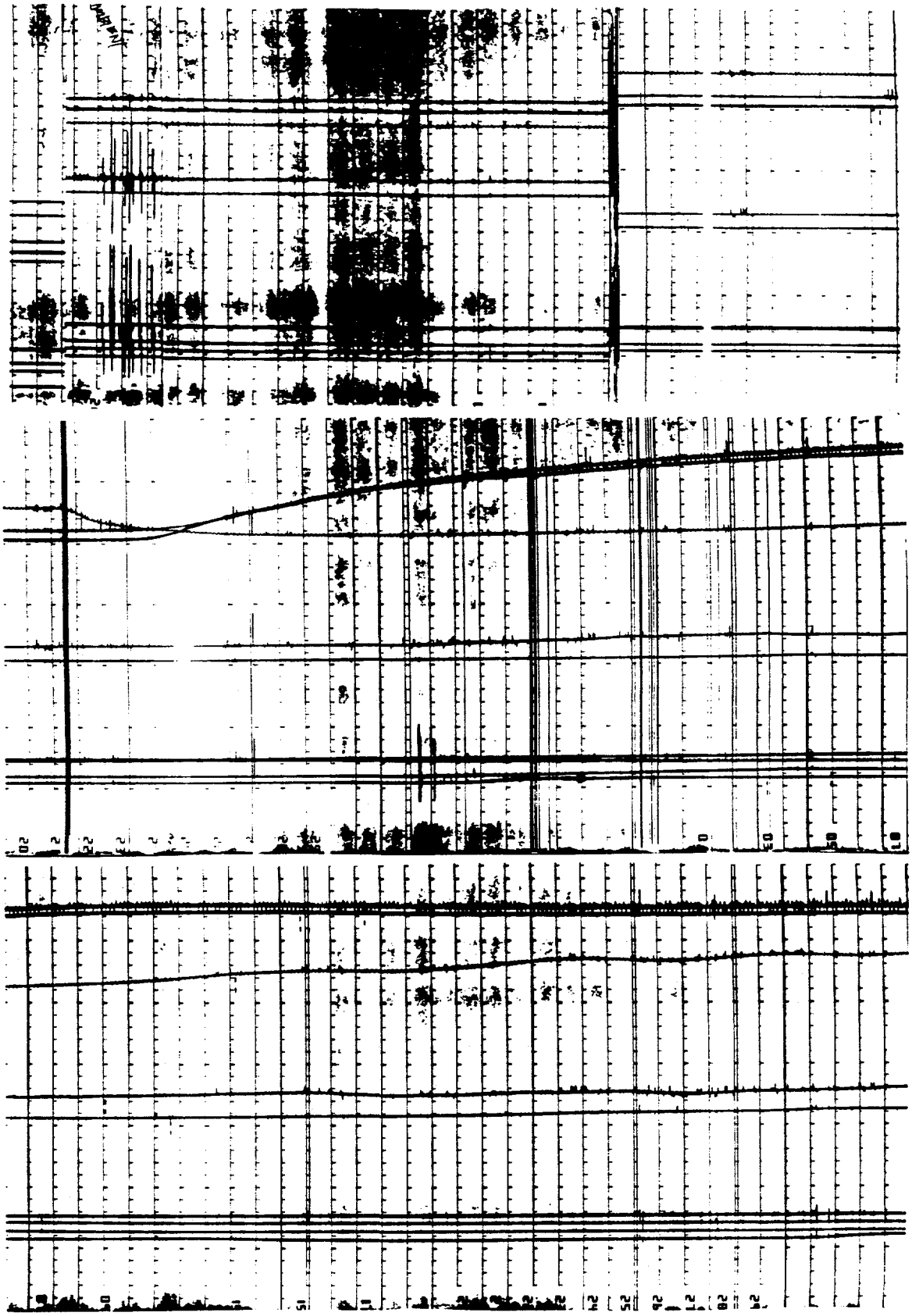

Oscillograph Trace - MFSBS-MJ5

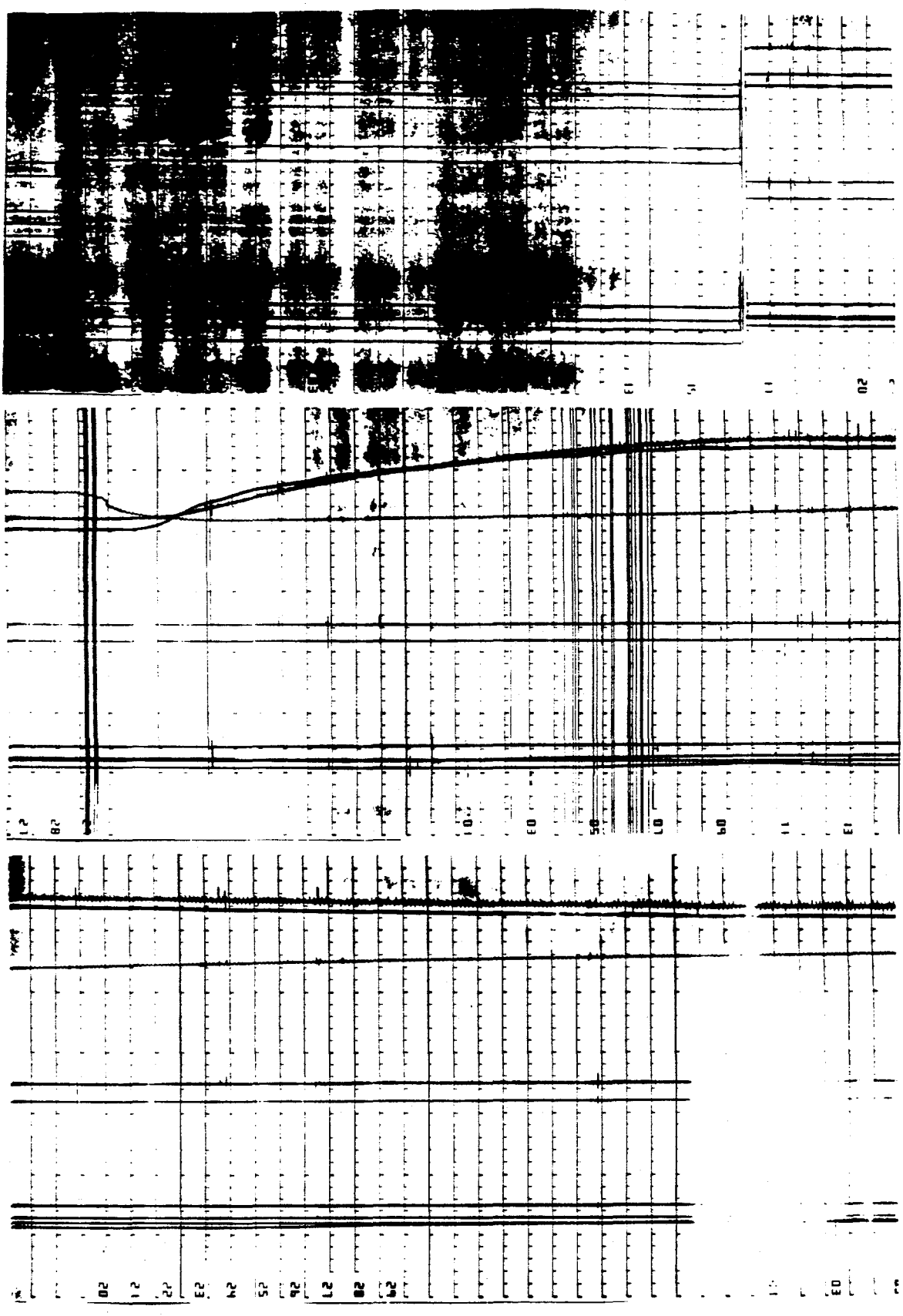

Oscillograph Trace - MFSBS-MJ6

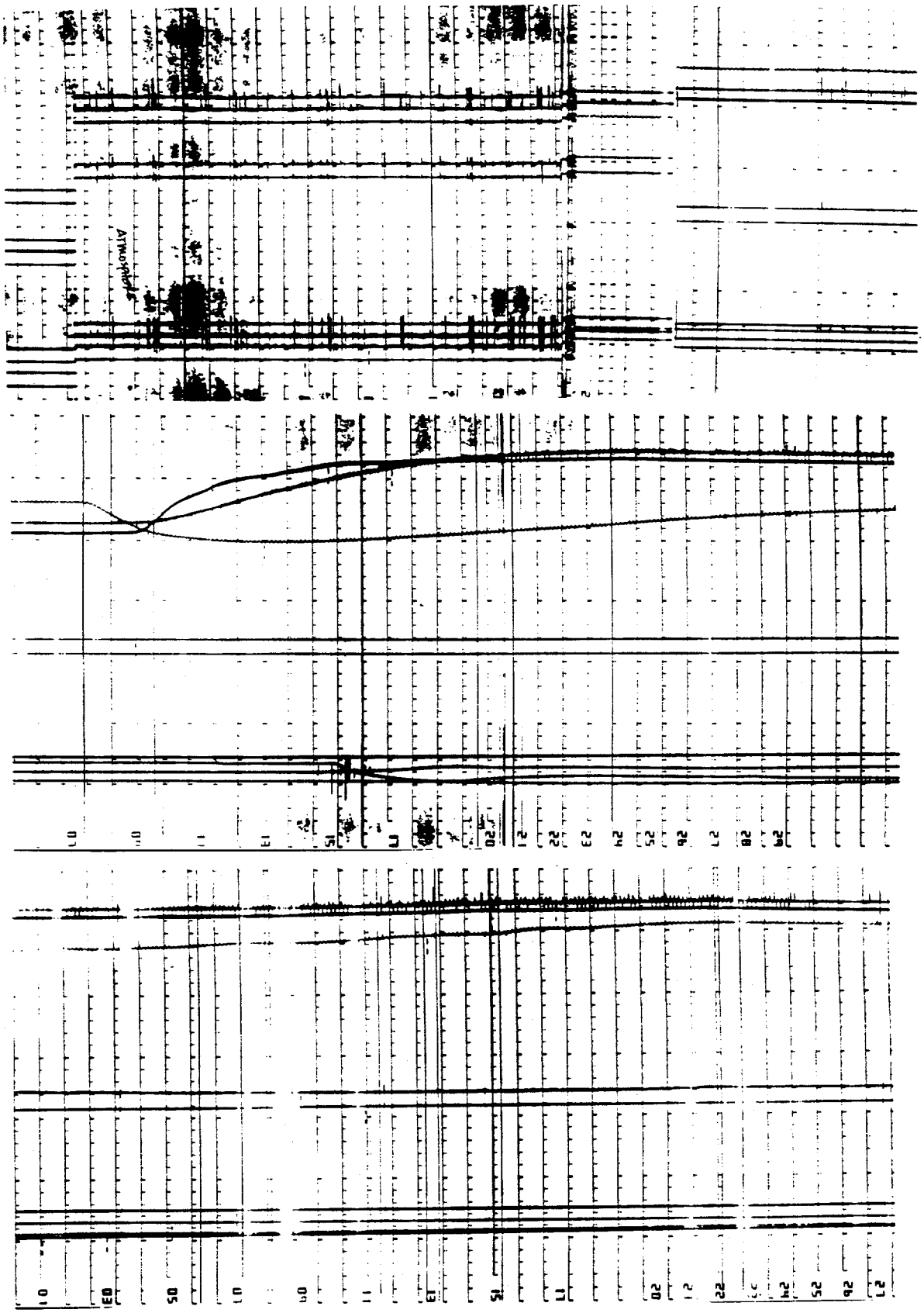

Oscillograph Trace - MFSBS-MJ7

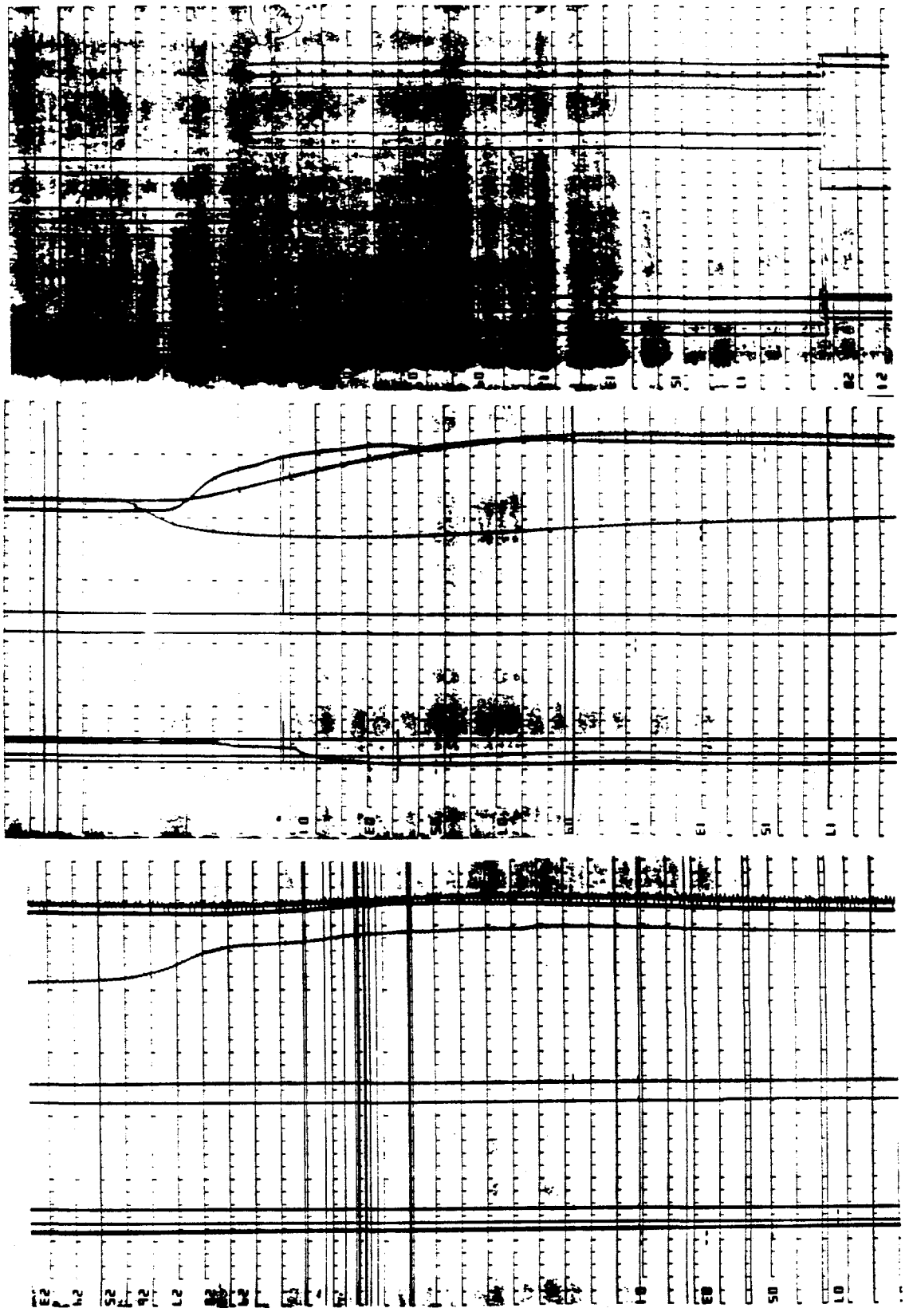

Oscillograph Trace - MFSBS-MJ8

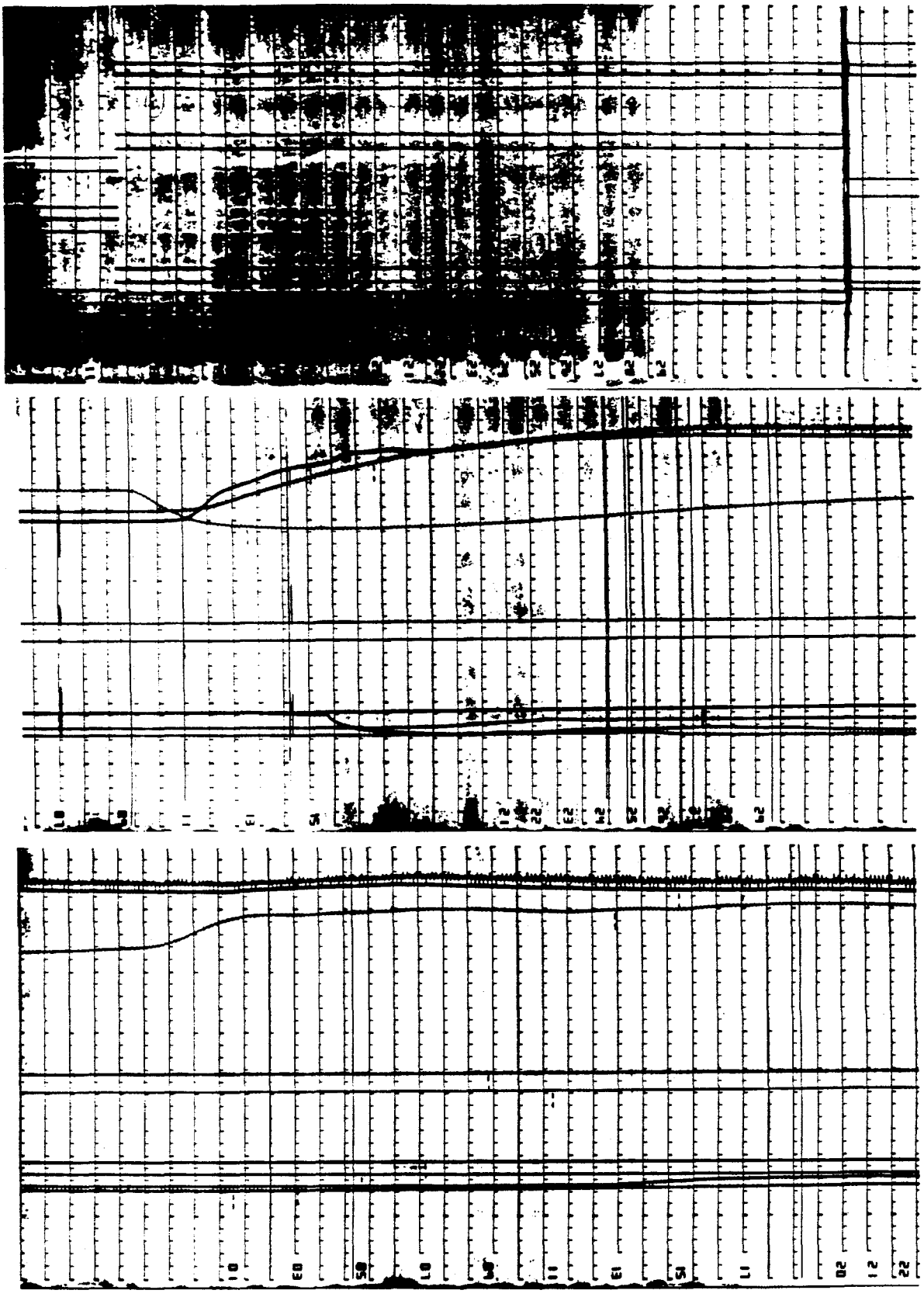

Oscillograph Trace - MFSBS-MJ9

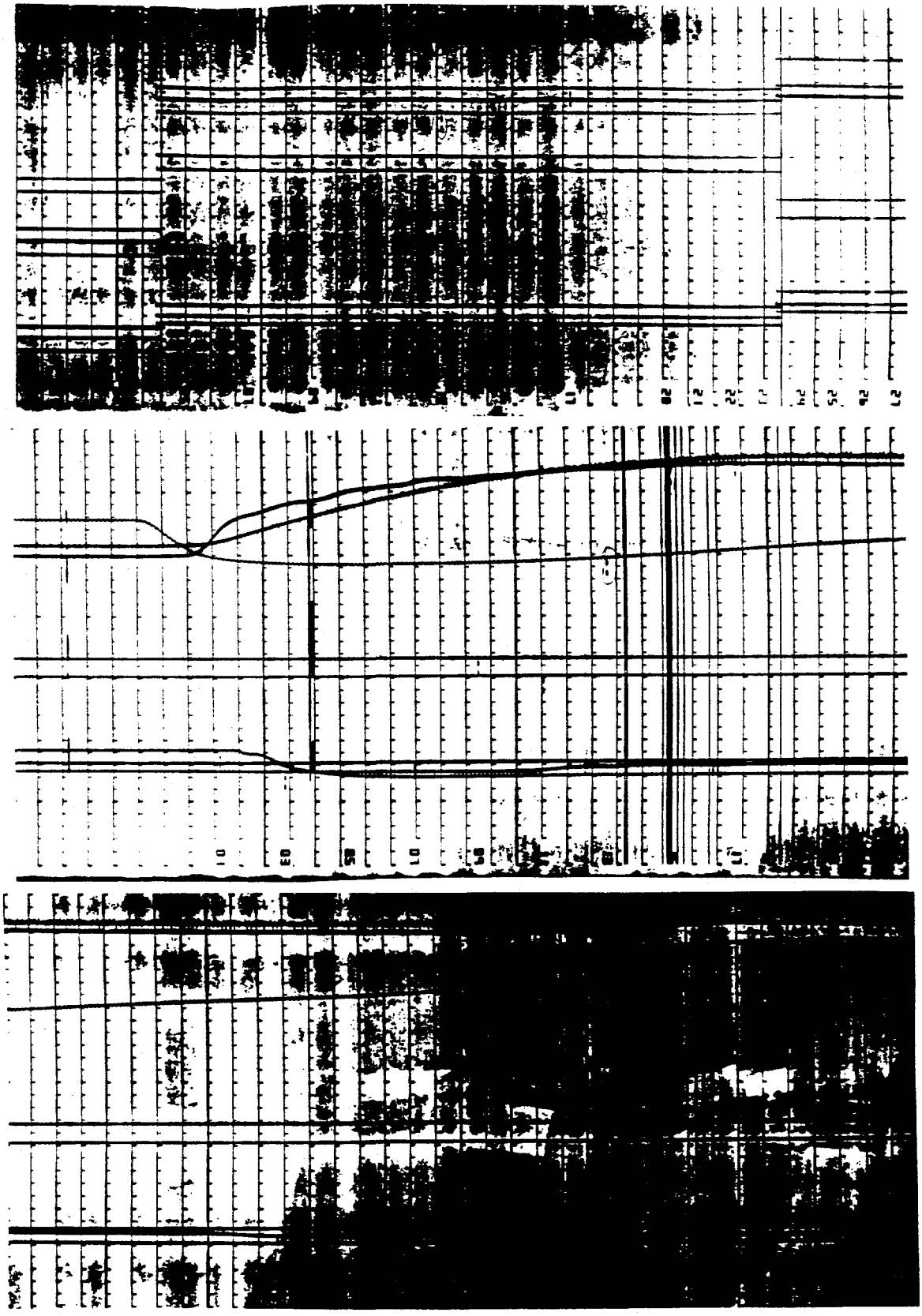

Oscillograph Trace - MFSBS-MJ10

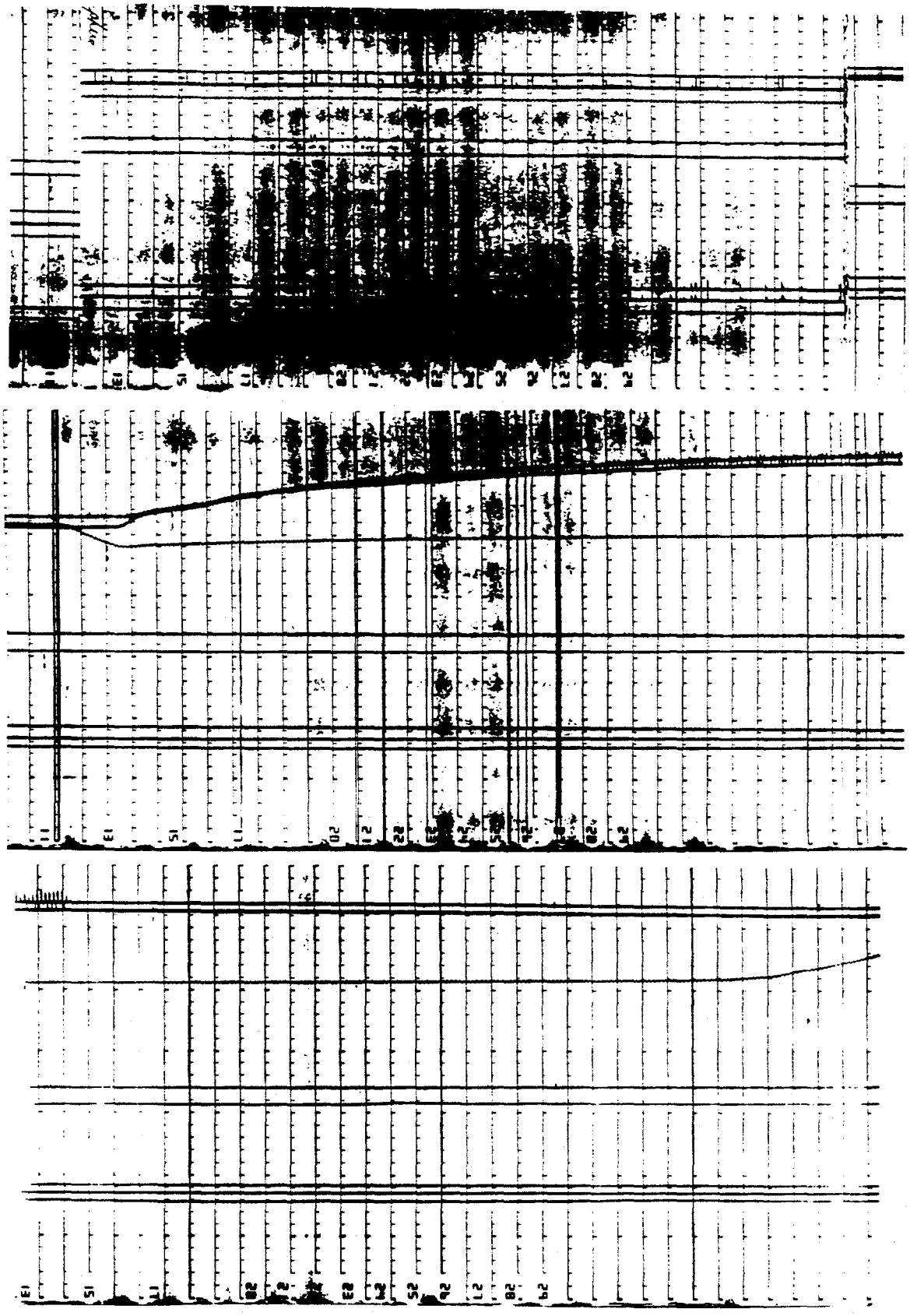

Oscillograph Trace - MFSBS-MJ11

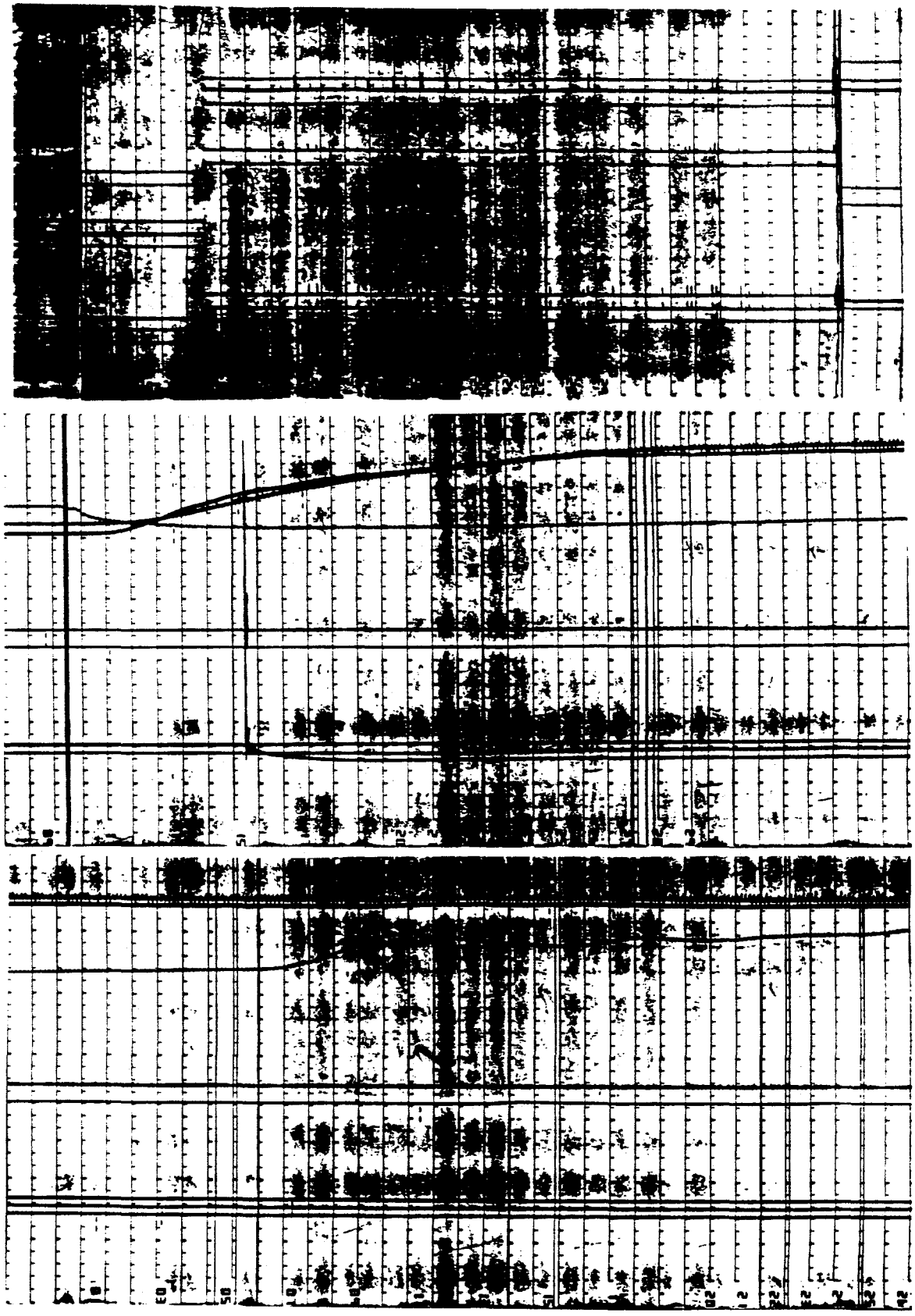

Oscillograph Trace - MFSBS-MJ12

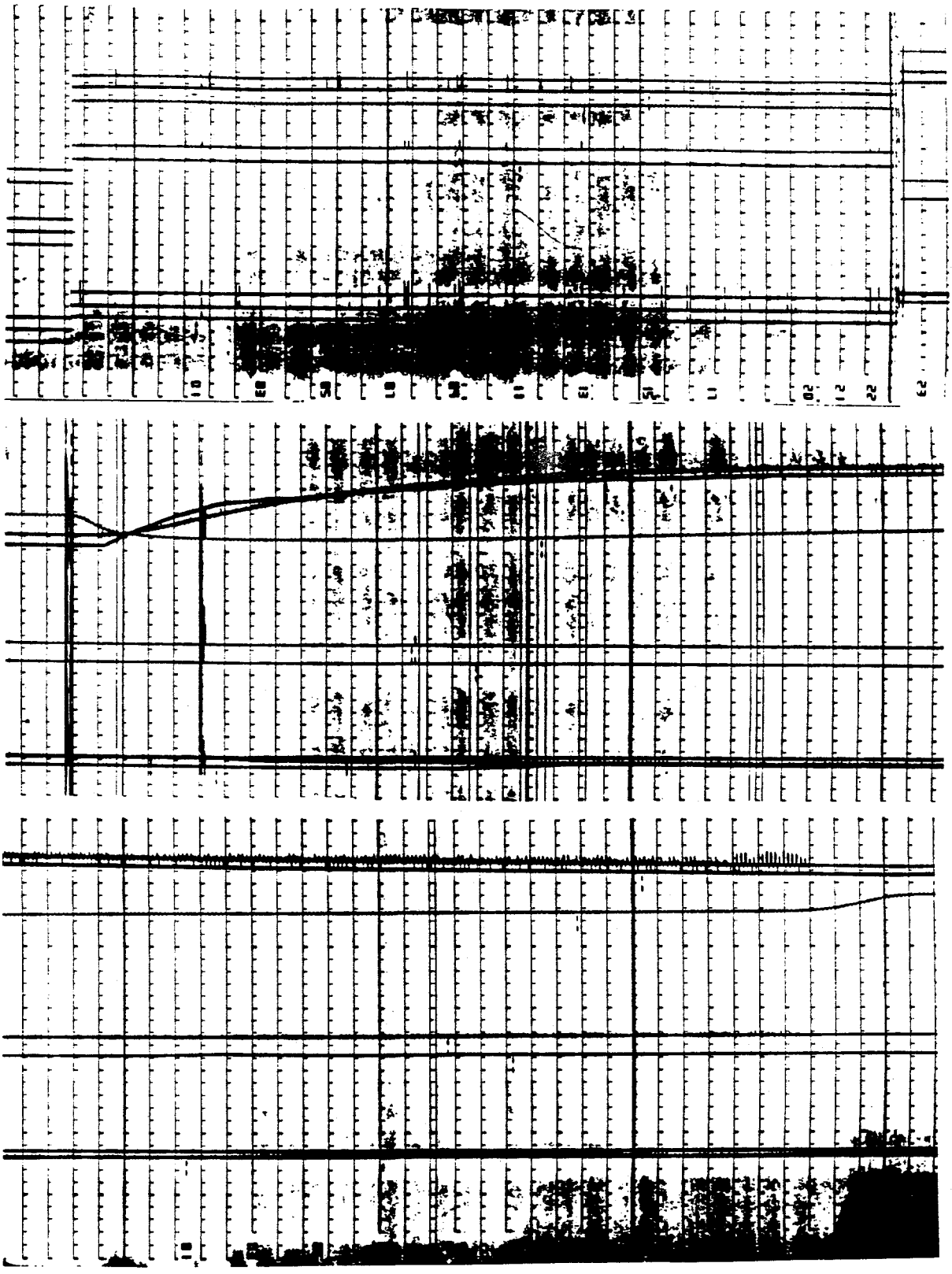

Oscillograph Trace - MFSBS-MJ13

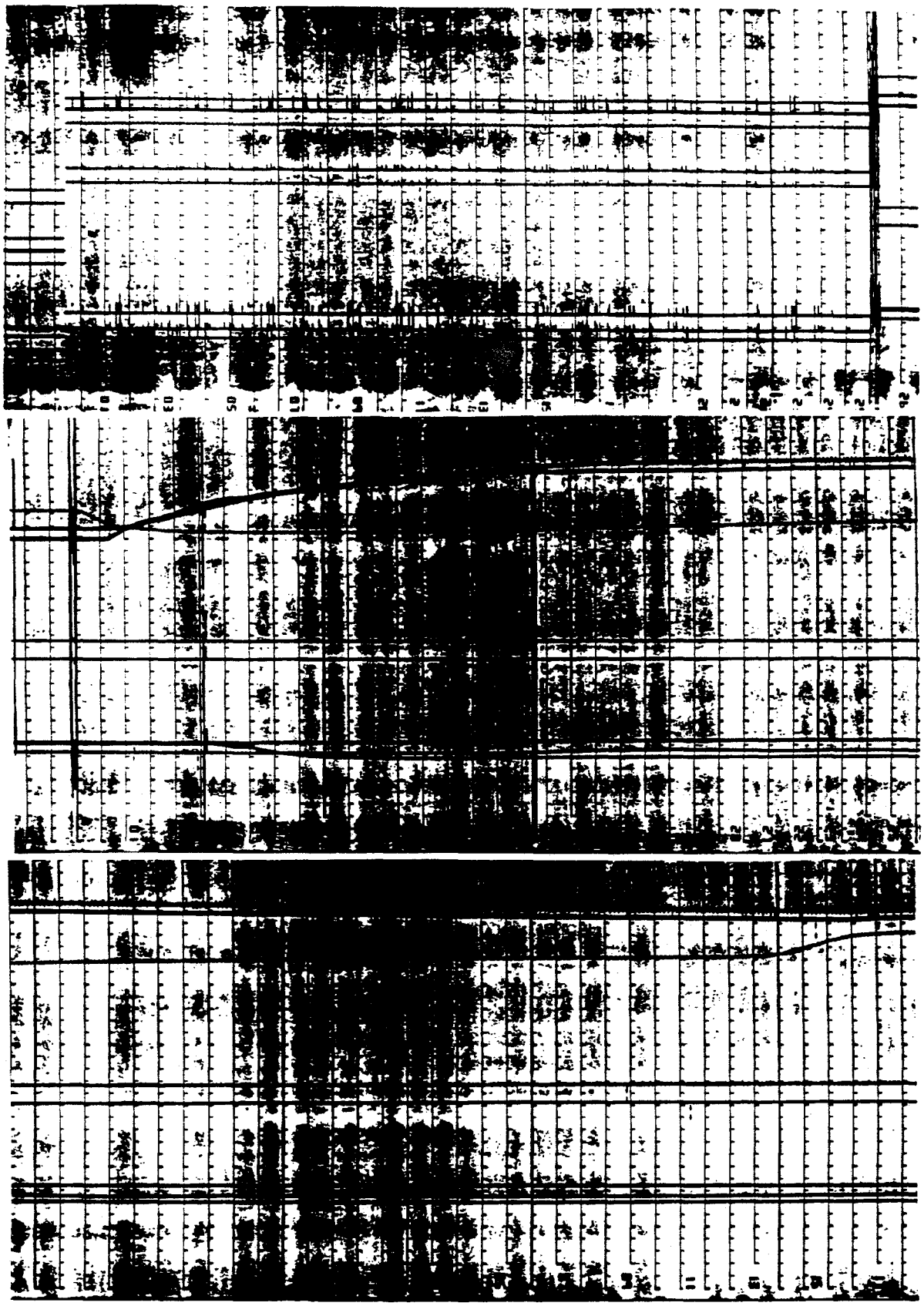

Oscillograph Trace - MFSBS-MJ14

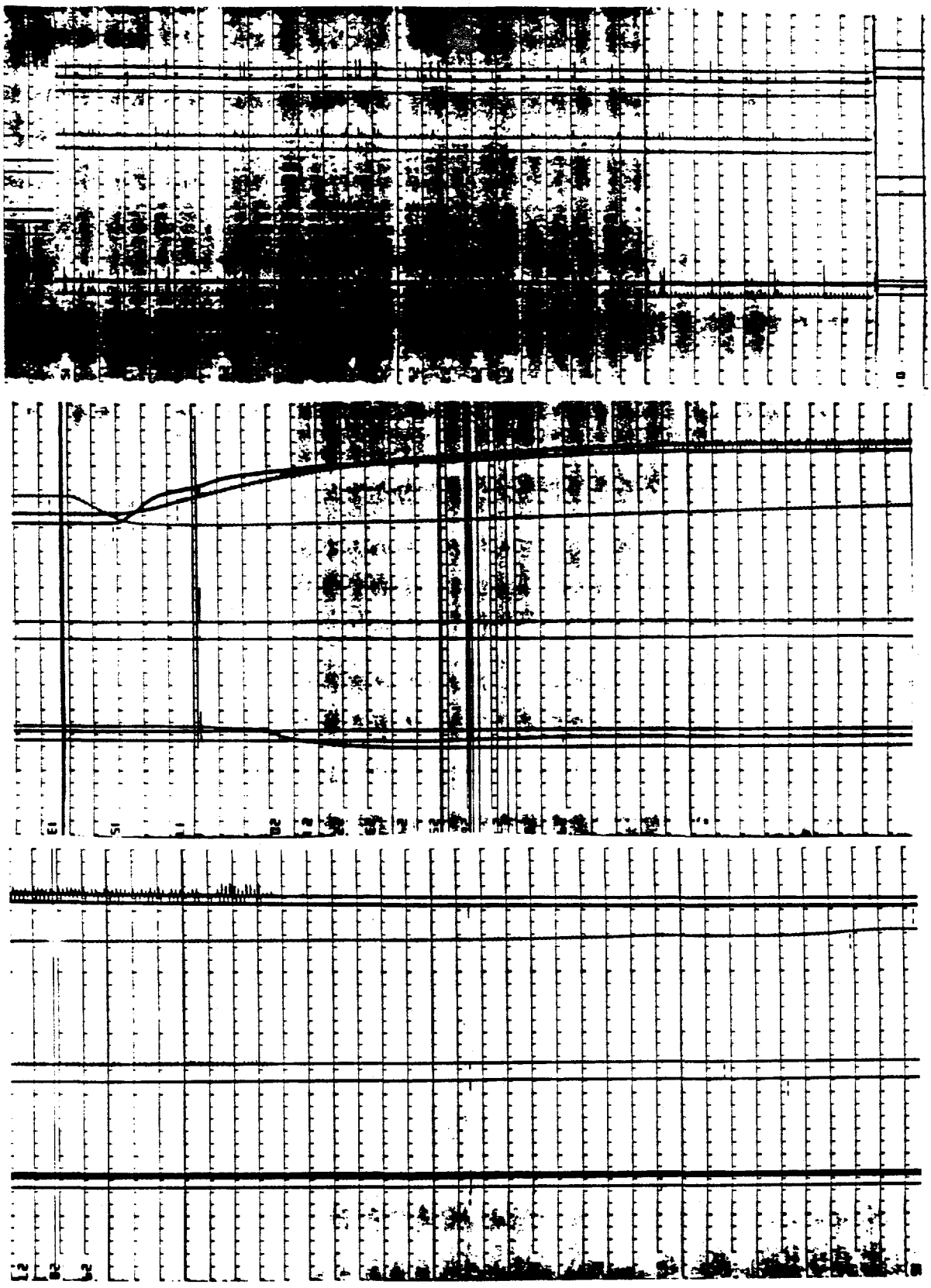

Oscillograph Trace - MFSBS-MJ15

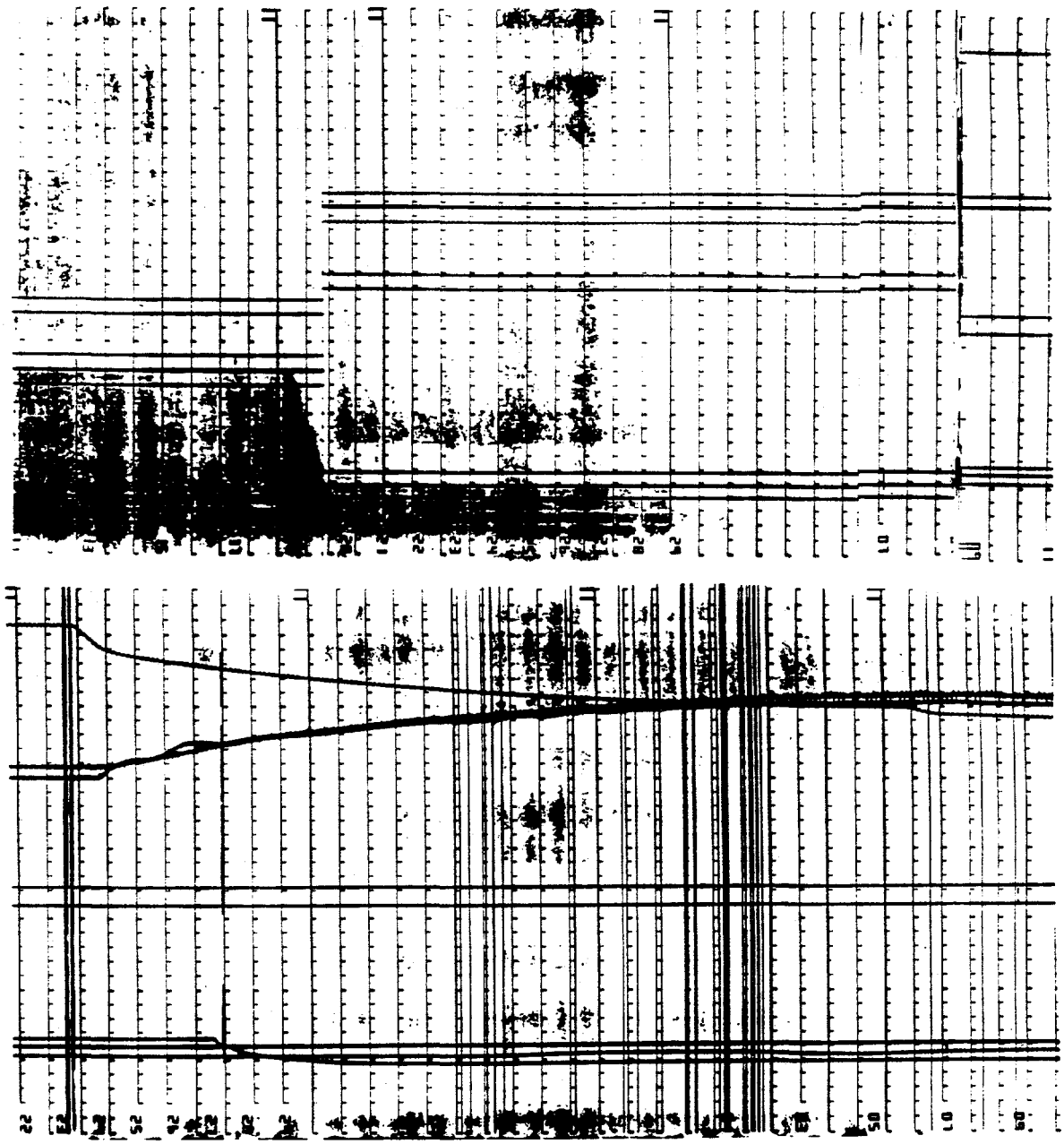

Oscillograph Trace - MFSBS-MJ16

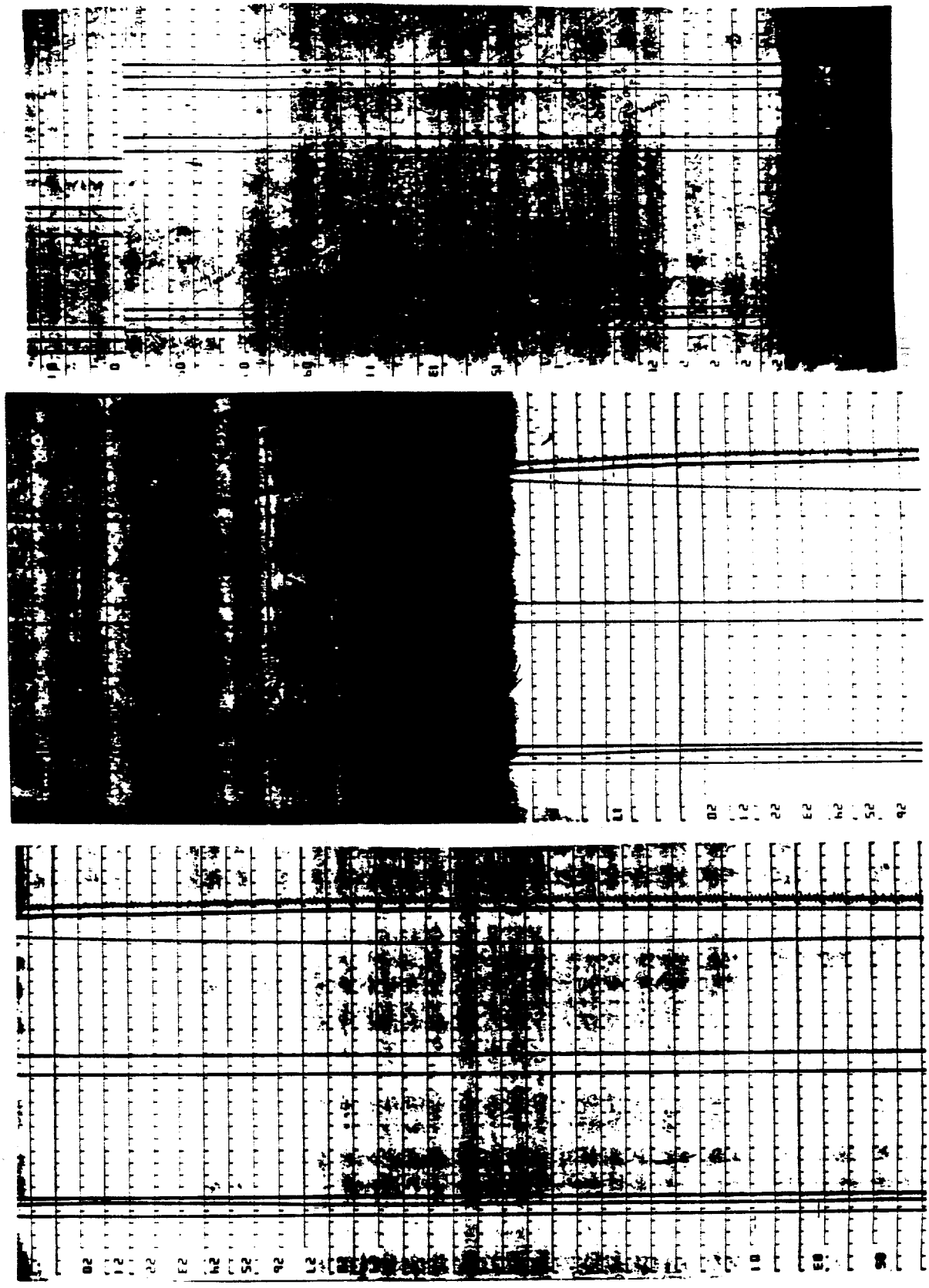

Oscillograph Trace - MFSBS-MJ17

APPENDIX D. Selected Frames from High Speed Motion Picture Films

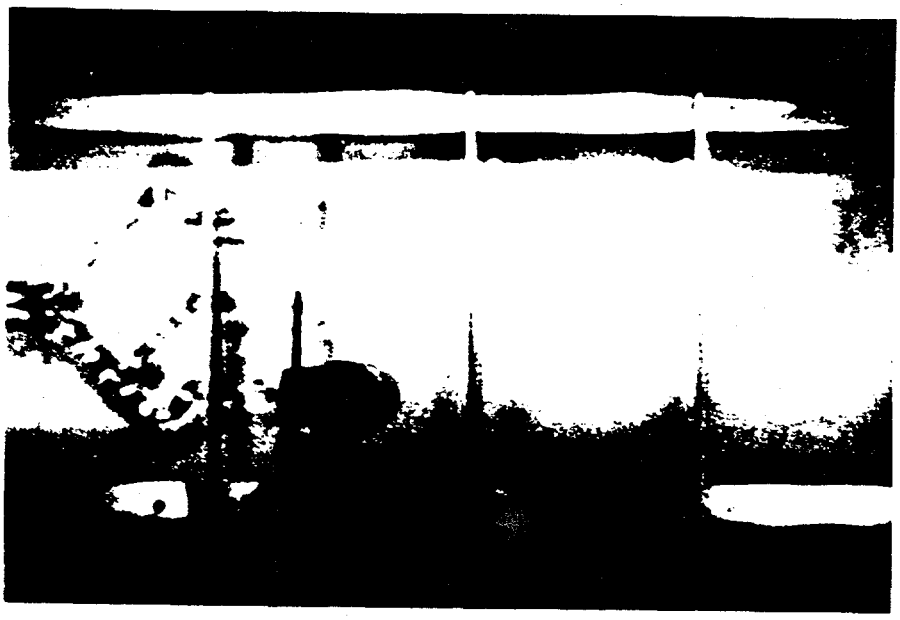

Contact - 0 ms

Time - 76 ms

Time - 156 ms

Breakup - 220 ms

Hycam #1 Film Selected Frames - MFSBS-MJ1

X-ray - 960 ms

Time - 1840 ms

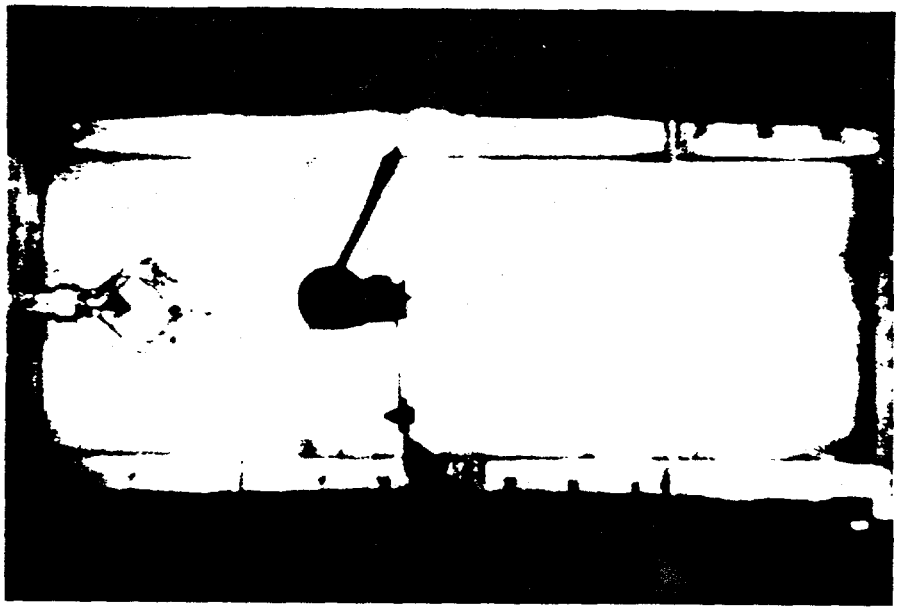

(Solenoid - 0 ms)
Contact - 478 ms

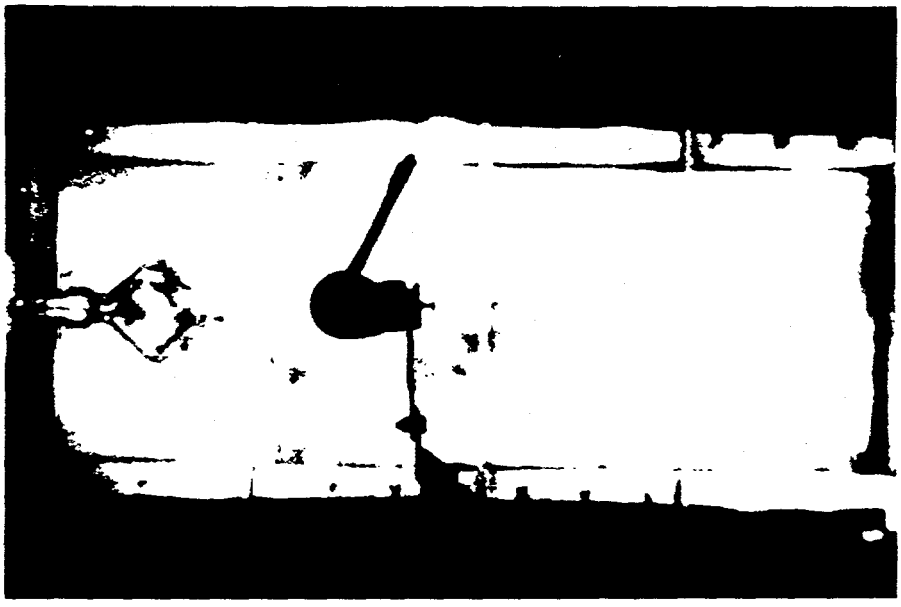

Time - 606 ms

Hycam #1 Film Selected Frames - MFSBS-MJ9

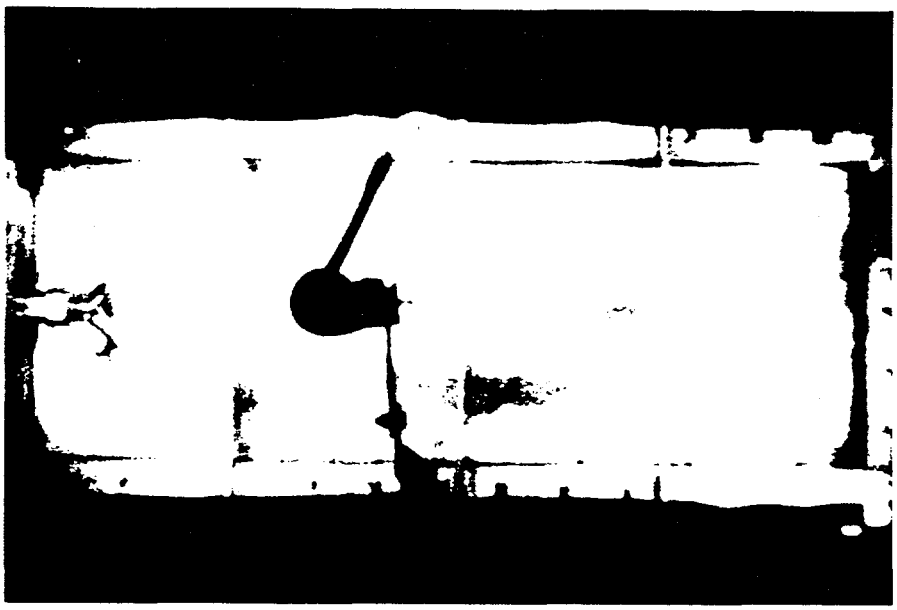

Time - 732 ms

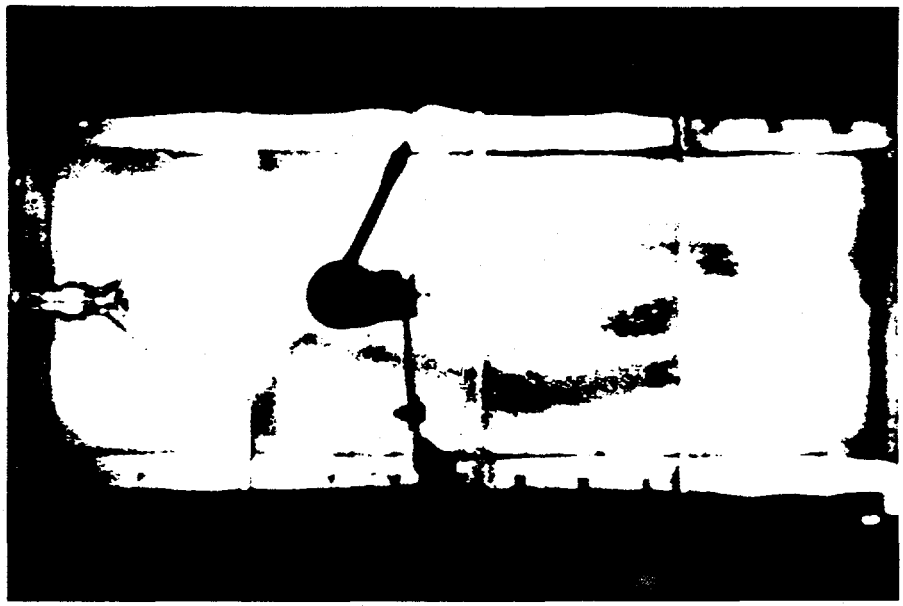

Breakup - 828 ms

Hycam #1 Film Selected Frames - MFSBS-MJ9

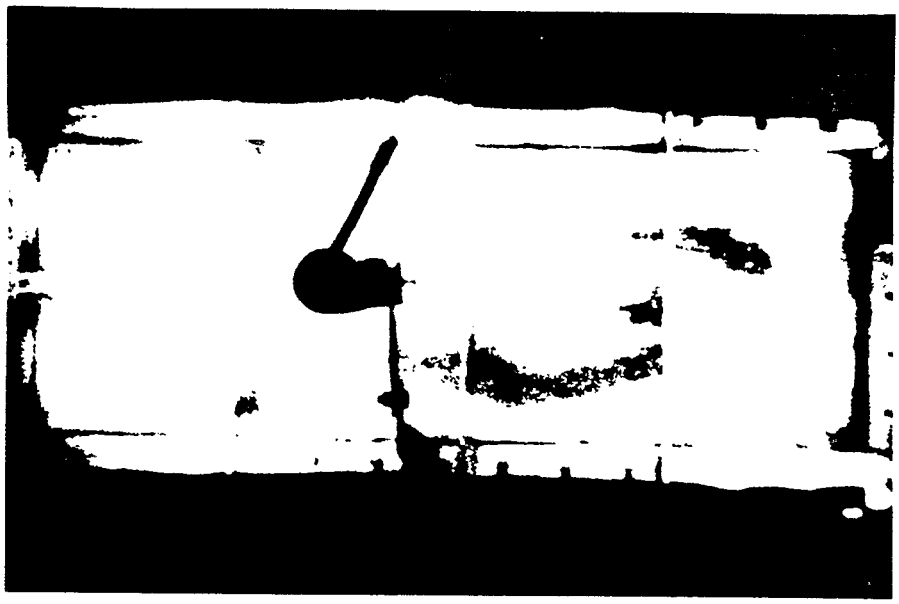

X-ray - 900 ms

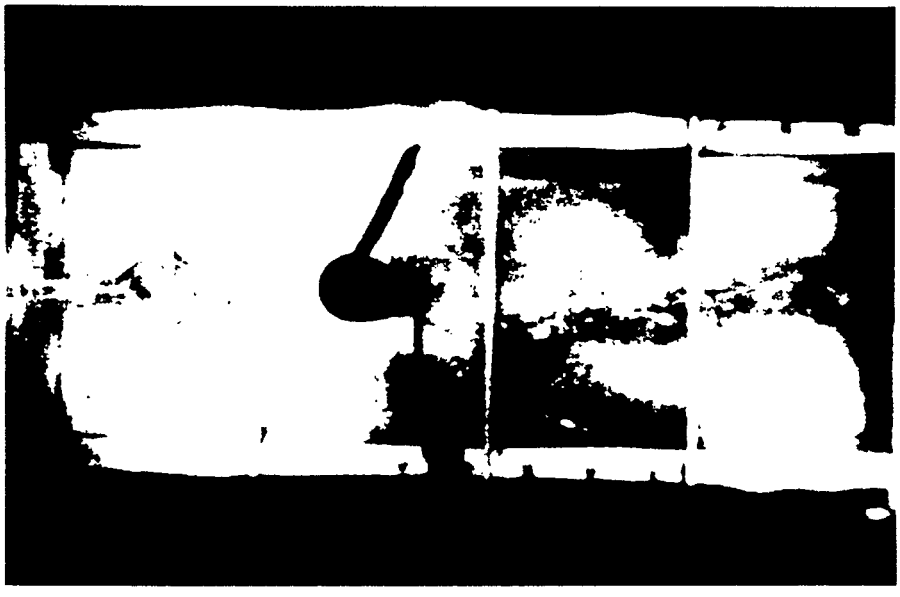

Time - 2208 ms

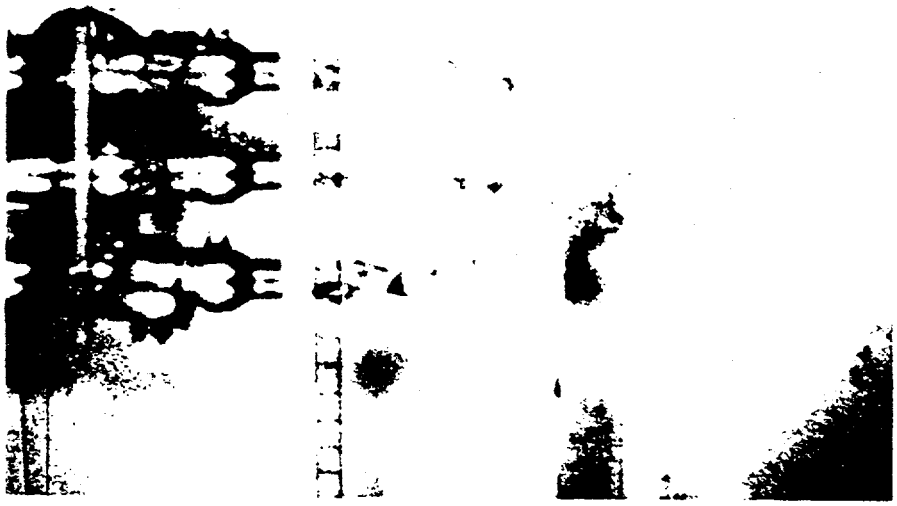

Contact - 0 ms

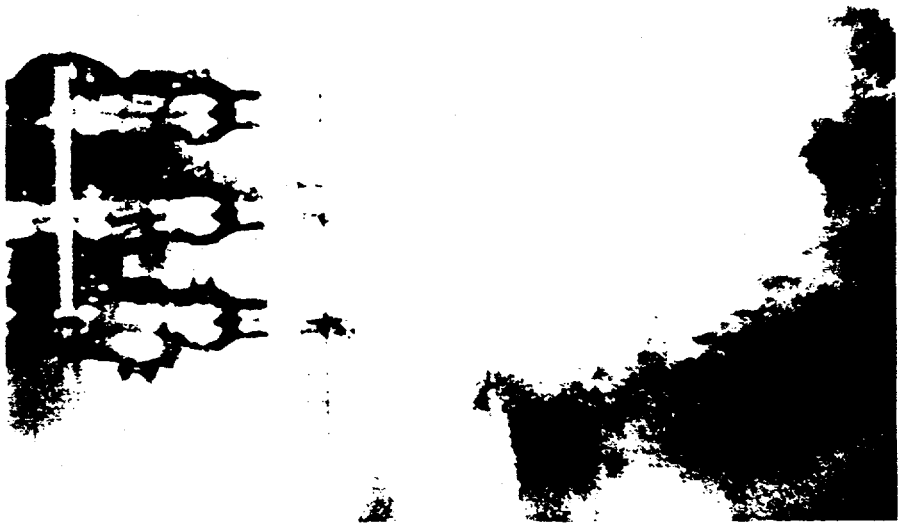

Time - 62 ms

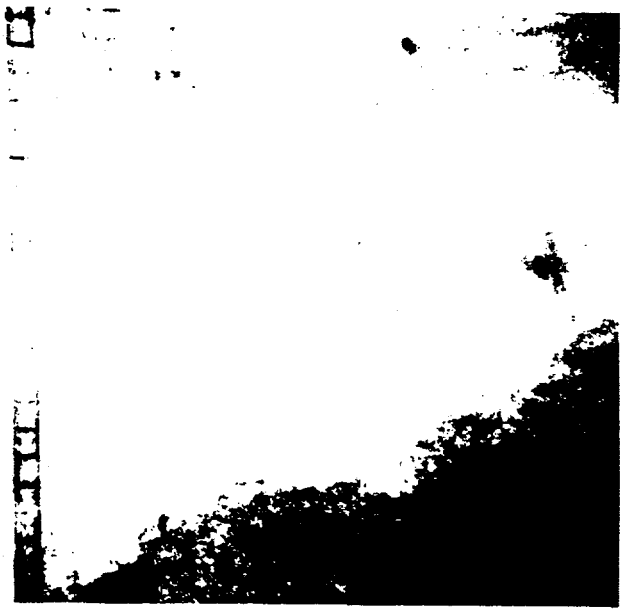

Time - 230 ms

Breakup - 350 ms

Hycam #2 Film Selected Frames - MFSBS-MJ9

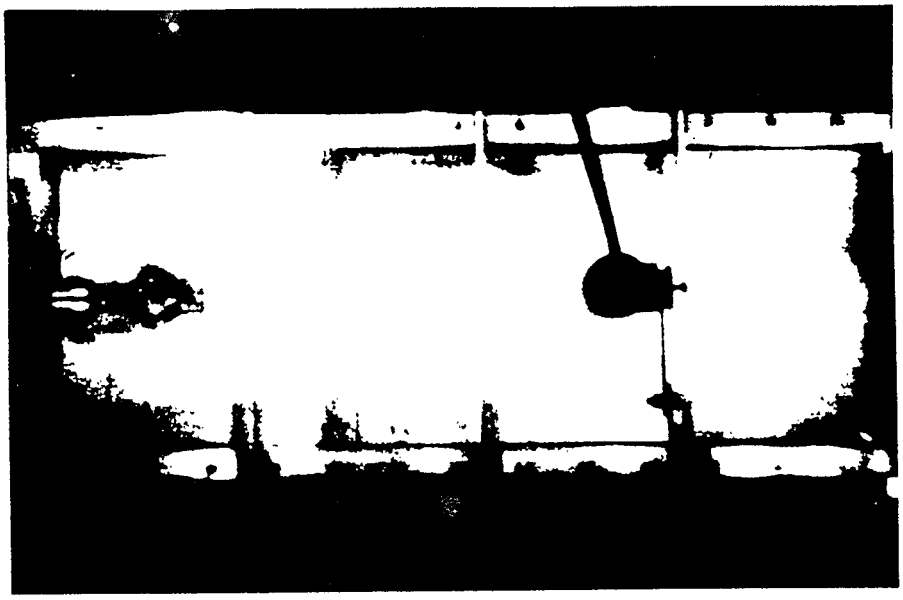

(Solenoid - 0 ms)
Contact - 380 ms

Time - 520 ms

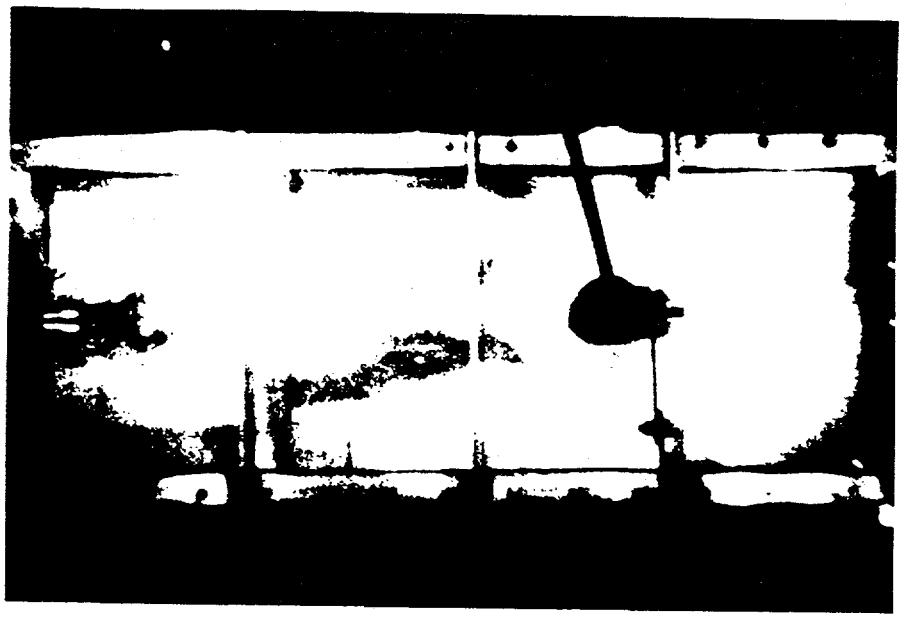

Breakup - 770 ms

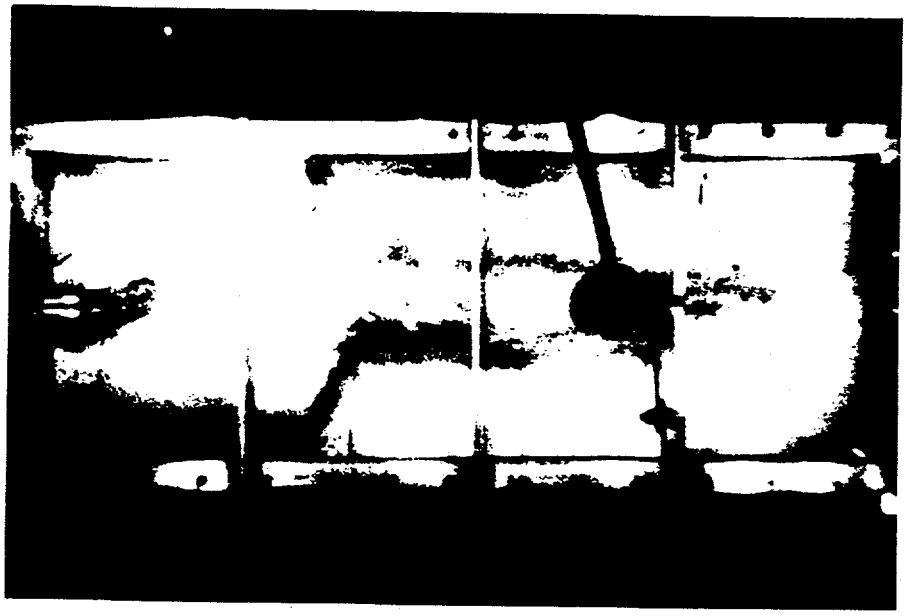

X-ray - 950 ms

Time - 1984 ms

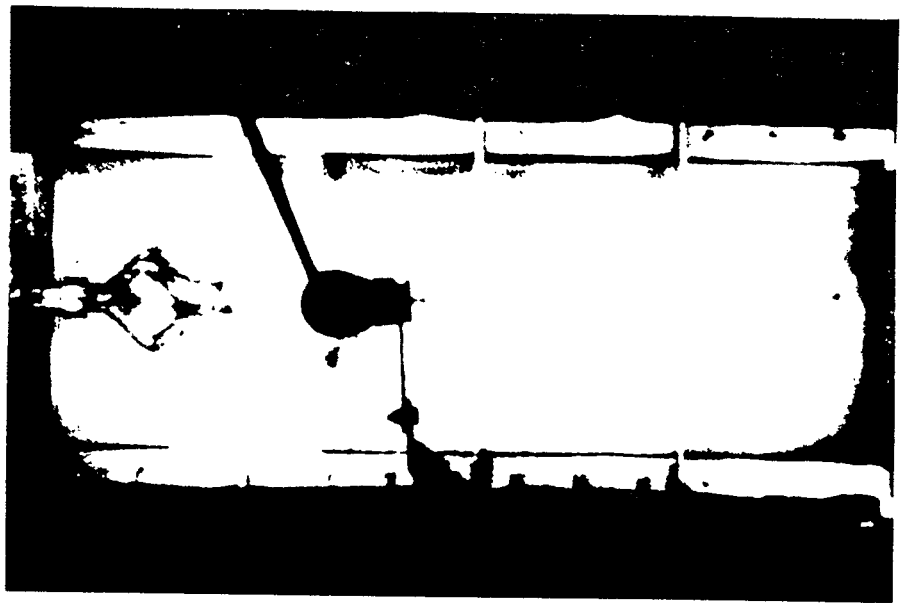

(Solenoid - 0 ms)
Contact - 420 ms

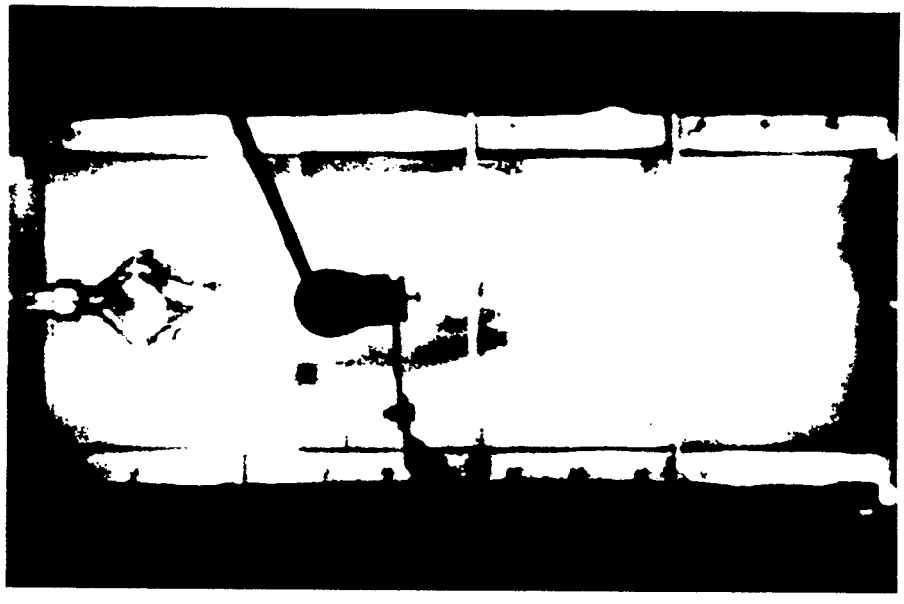

Time - 484 ms

Hycam #1 Film Selected Frames - MFSBS-MJ17

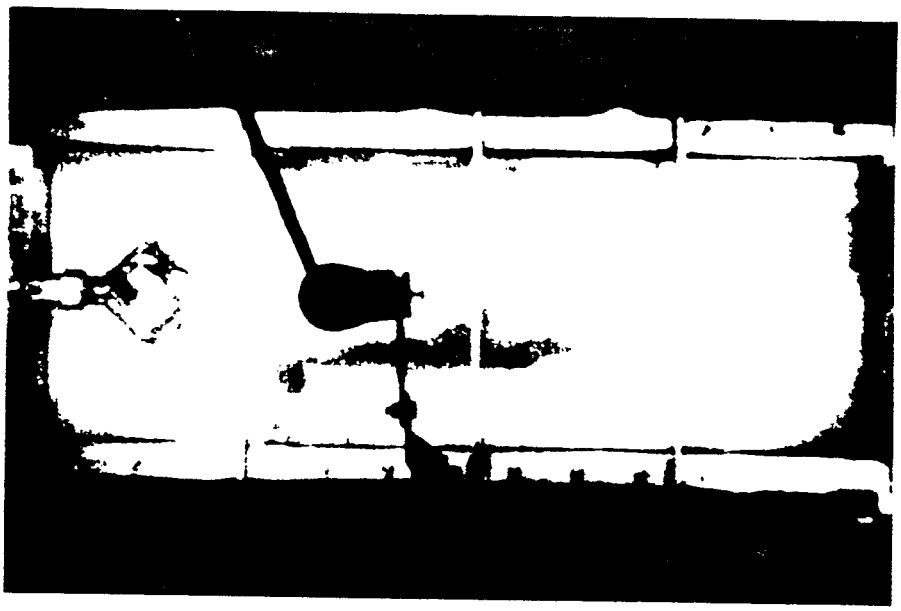

Time - 570 ms

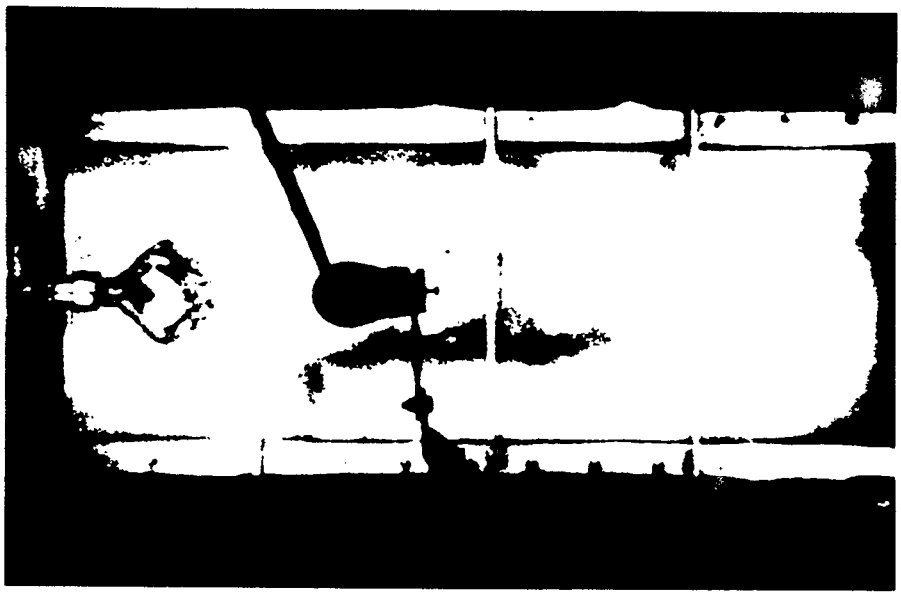

Breakup - 620 ms

Hycam #1 Film Selected Frames - MFSBS-MJ17

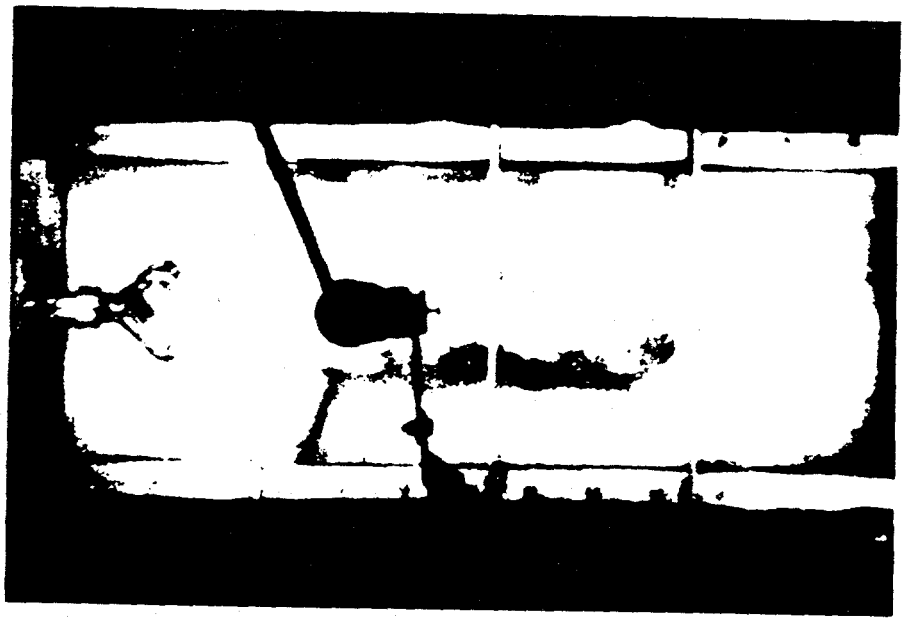

X-ray - 750 ms

Time - 2078 ms

APPENDIX E. Selected Radiographs

Radiograph - MFSBS-MJ3
Single Jet; 1/2" Nozzle; High Position

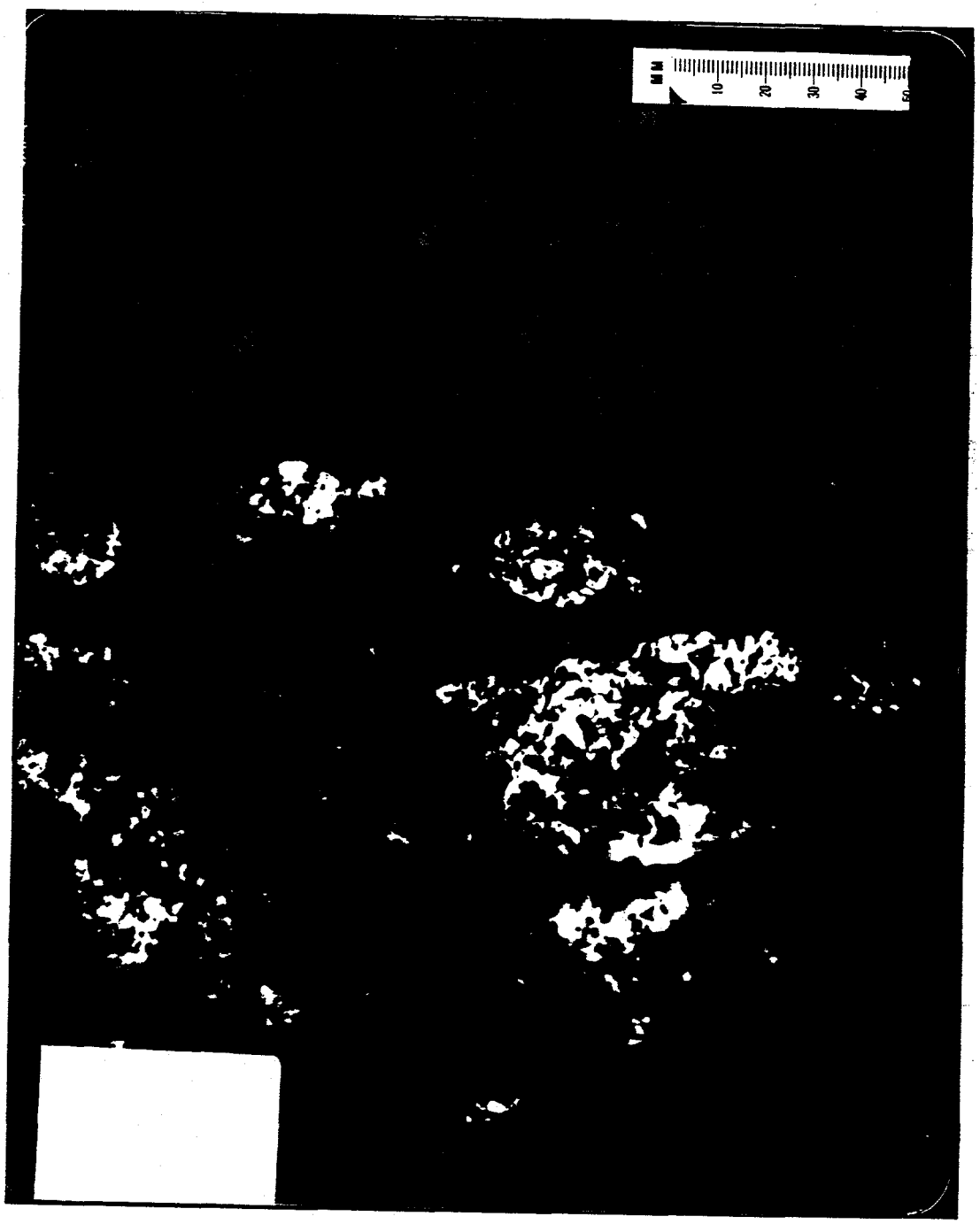

Radiograph - MFSBS-MJ5
3" Spacing; 1/2" Nozzles; High Position

Radiograph - MFSBS-MJ9
1-1/2" Spacing; 1/2" Nozzles; High Position

Radiograph - MFSBS-MJ13
3/4" Spacing; 3/8" Nozzles; High Position

Radiograph - MFSBS-MJ14
3/4" Spacing; 3/8" Nozzles; Low Position

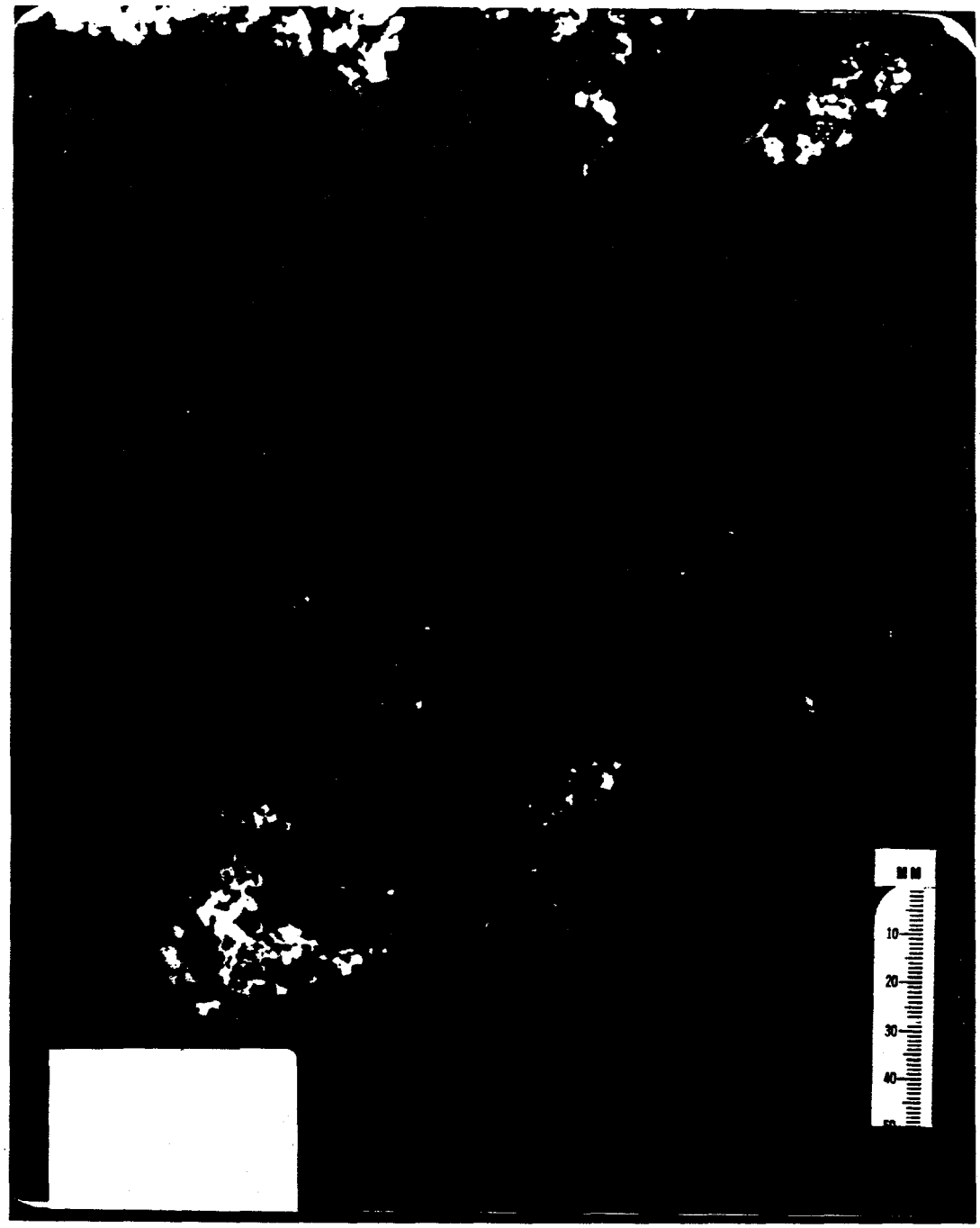

Radiograph - MFSBS-MJ15
1-1/2" Spacing; 3/8" Nozzles; Low Position

Radiograph - MFSBS-MJ17
1-1/2" Spacing; 1/4" Nozzles; High Position

APPENDIX F. Hycam #1 Films Data Reduction

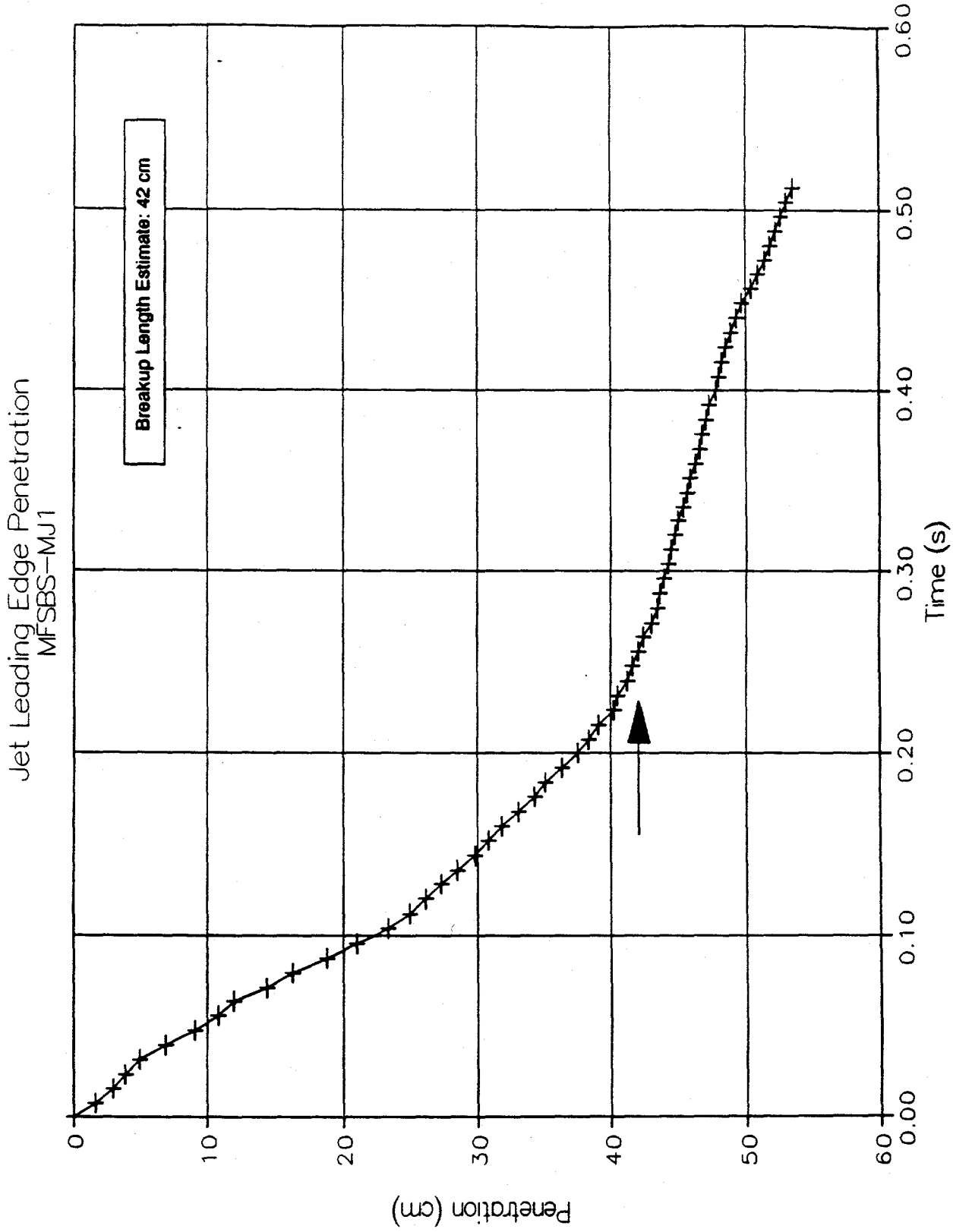
Jet Leading Edge Penetration
MFSBS-MJ1
Breakup Length Estimate: 42 cm
Penetration (cm)
0
10
20
30
40
50
60
Time (s)
0.00
0.10
0.20
0.30
0.40
0.50
0.60

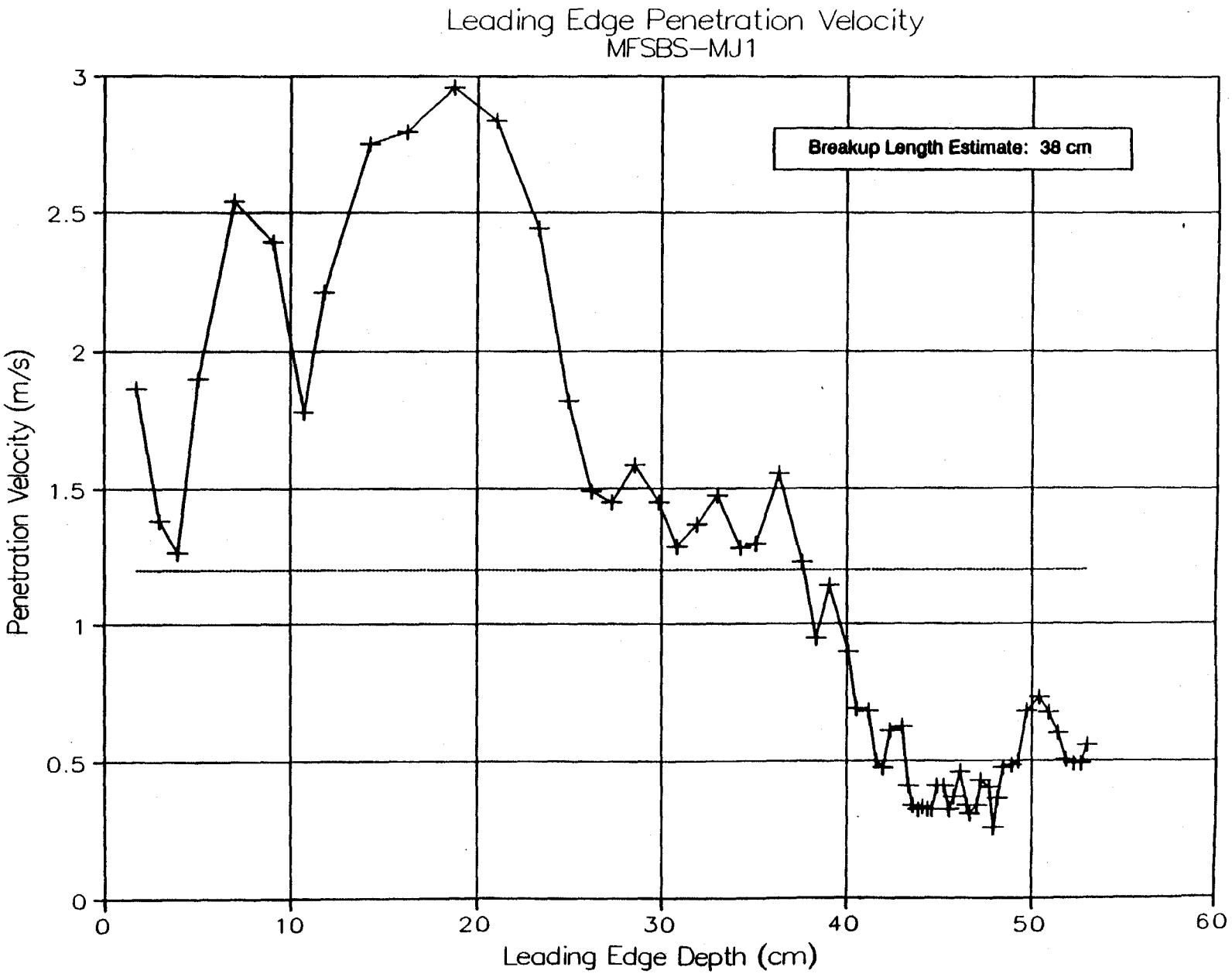
Leading Edge Penetration Velocity
MFSBS–MJ1
Breakup Length Estimate: 38 cm
Penetration Velocity (m/s)
Leading Edge Depth (cm)
0
0.5
1
1.5
2
2.5
3
0
10
20
30
40
50
60

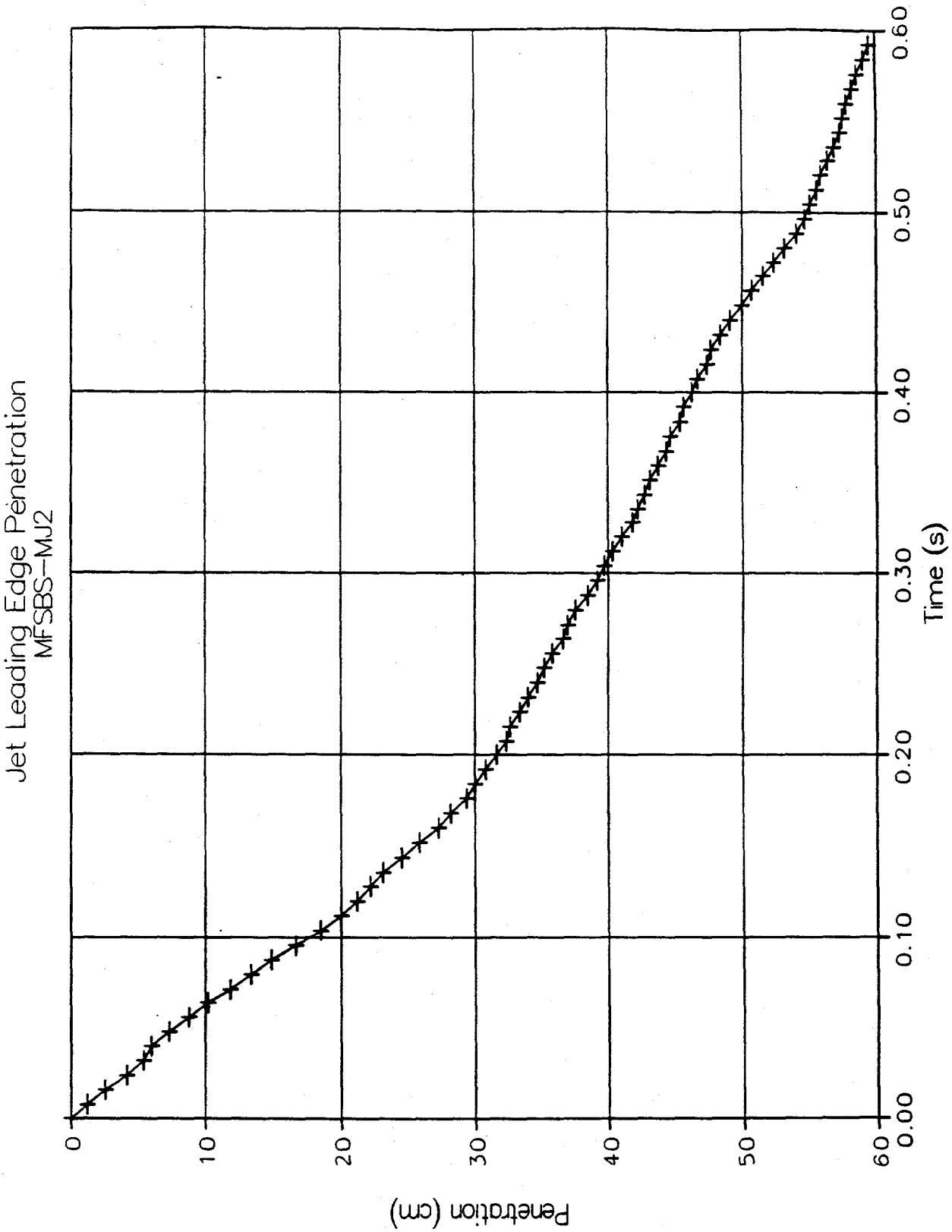
Jet Leading Edge Penetration
MFSBS-MJ2
Penetration (cm)
0
10
20
30
40
50
60
Time (s)
0.00
0.10
0.20
0.30
0.40
0.50
0.60

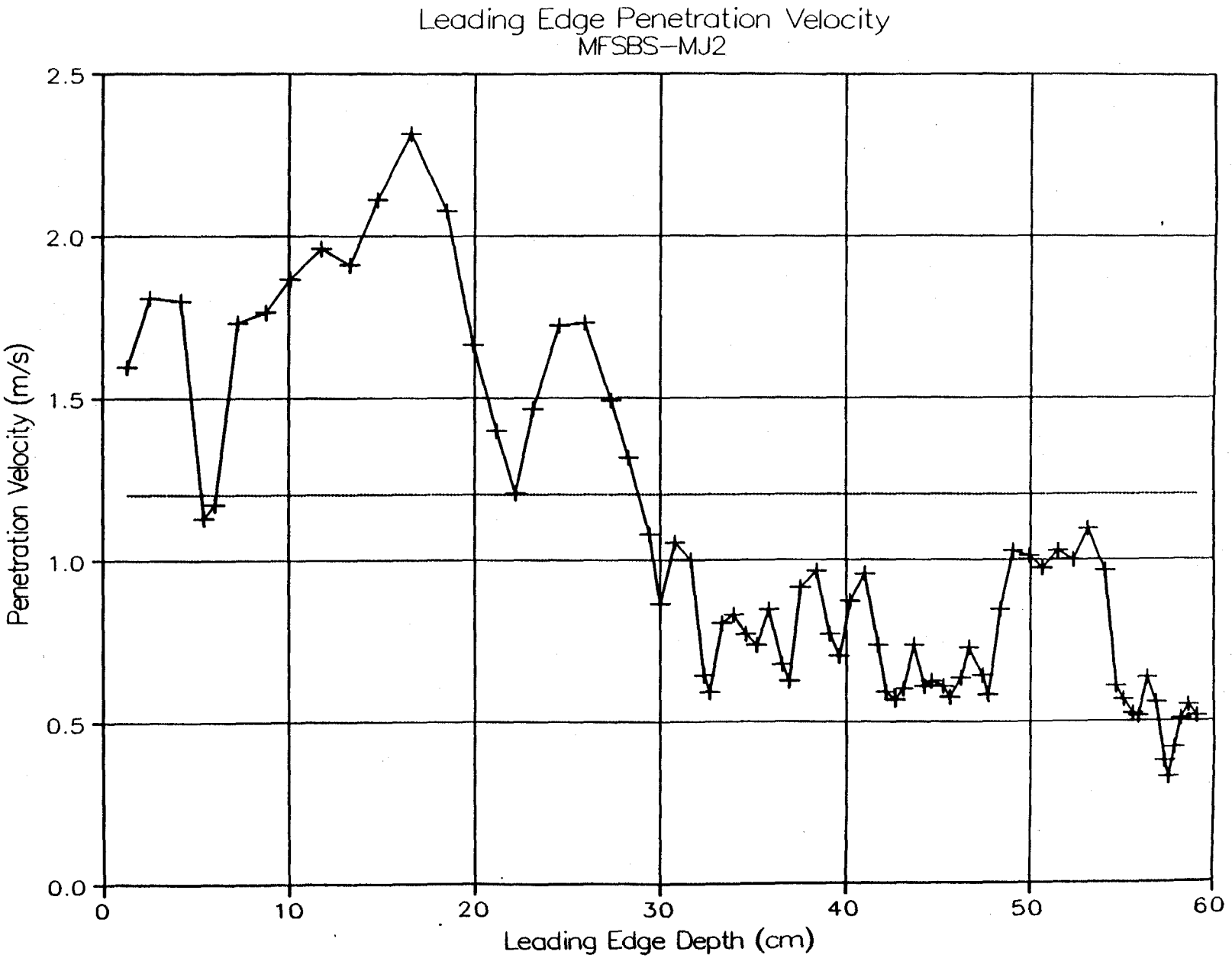
Leading Edge Penetration Velocity
MFSBS–MJ2
Penetration Velocity (m/s)
2.5
2.0
1.5
1.0
0.5
0.0
0
10
20
30
40
50
60
Leading Edge Depth (cm)

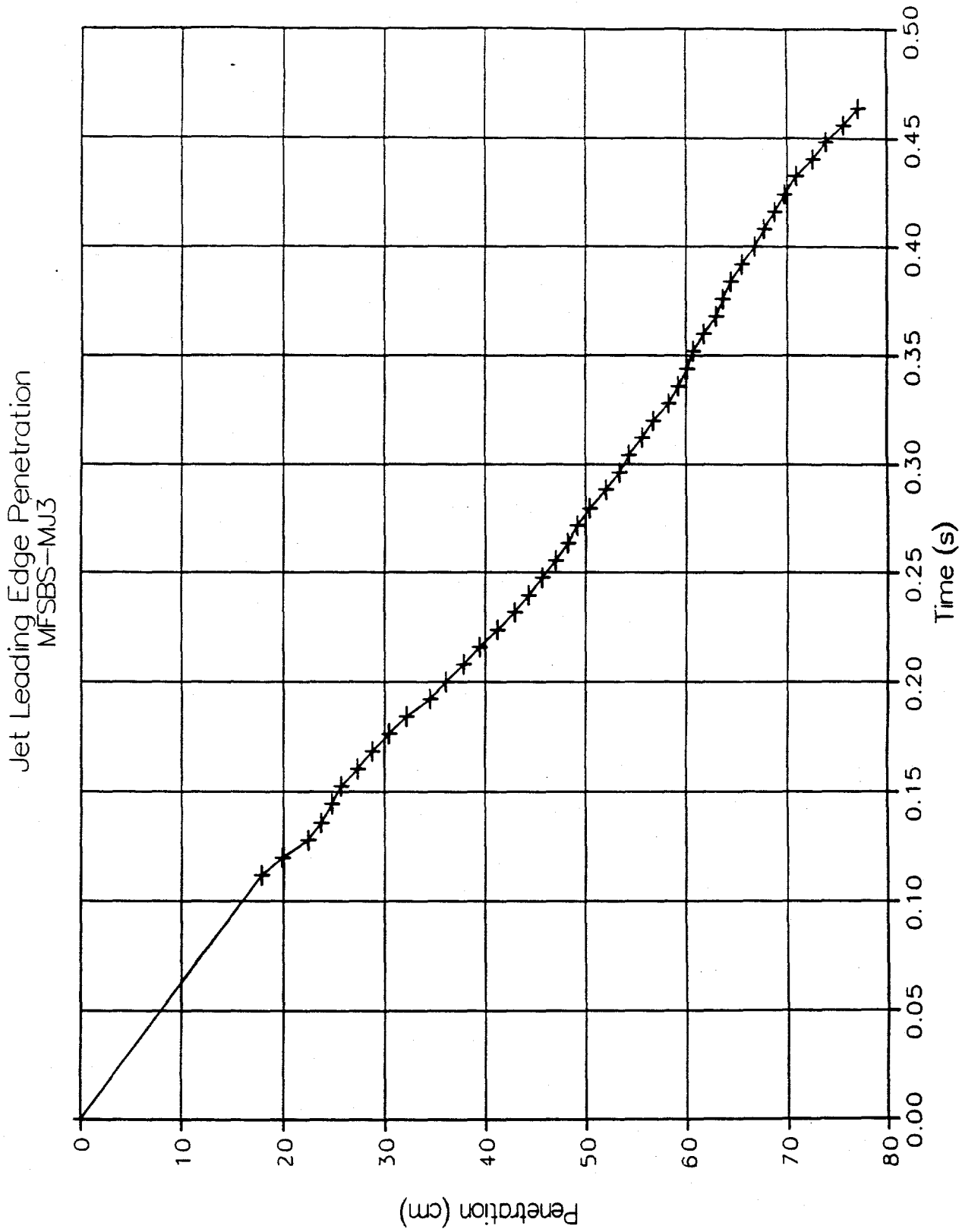
Jet Leading Edge Penetration
MFSBS-MJ3
Penetration (cm)
0
10
20
30
40
50
60
70
80
Time (s)
0.00
0.05
0.10
0.15
0.20
0.25
0.30
0.35
0.40
0.45
0.50

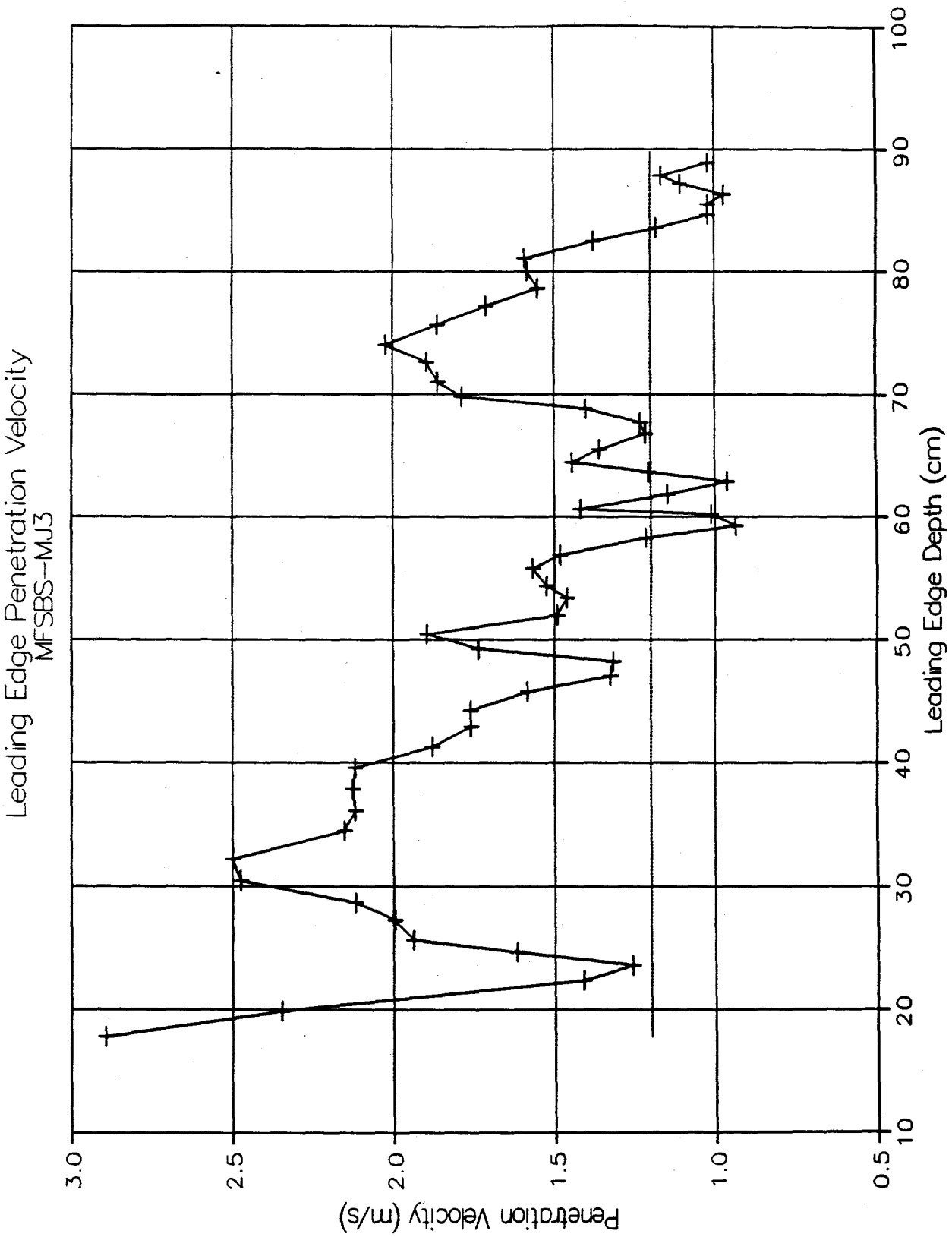
Leading Edge Penetration Velocity
MFSBS-MJ3
Penetration Velocity (m/s)
3.0
2.5
2.0
1.5
1.0
0.5
Leading Edge Depth (cm)
10
20
30
40
50
60
70
80
90
100

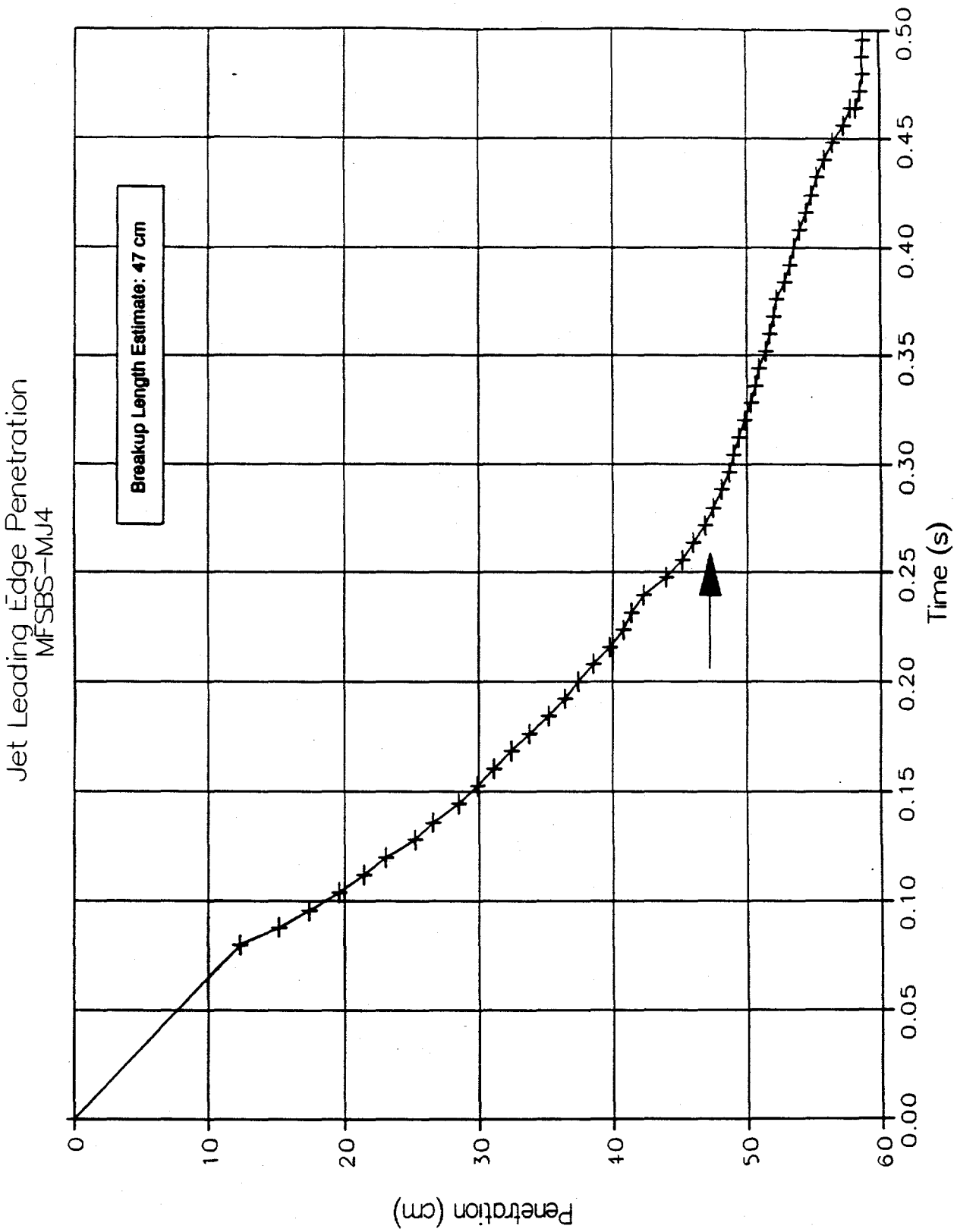
Jet Leading Edge Penetration
MFSBS-MJ4
Breakup Length Estimate: 47 cm
Penetration (cm)
0
10
20
30
40
50
60
Time (s)
0.00
0.05
0.10
0.15
0.20
0.25
0.30
0.35
0.40
0.45
0.50

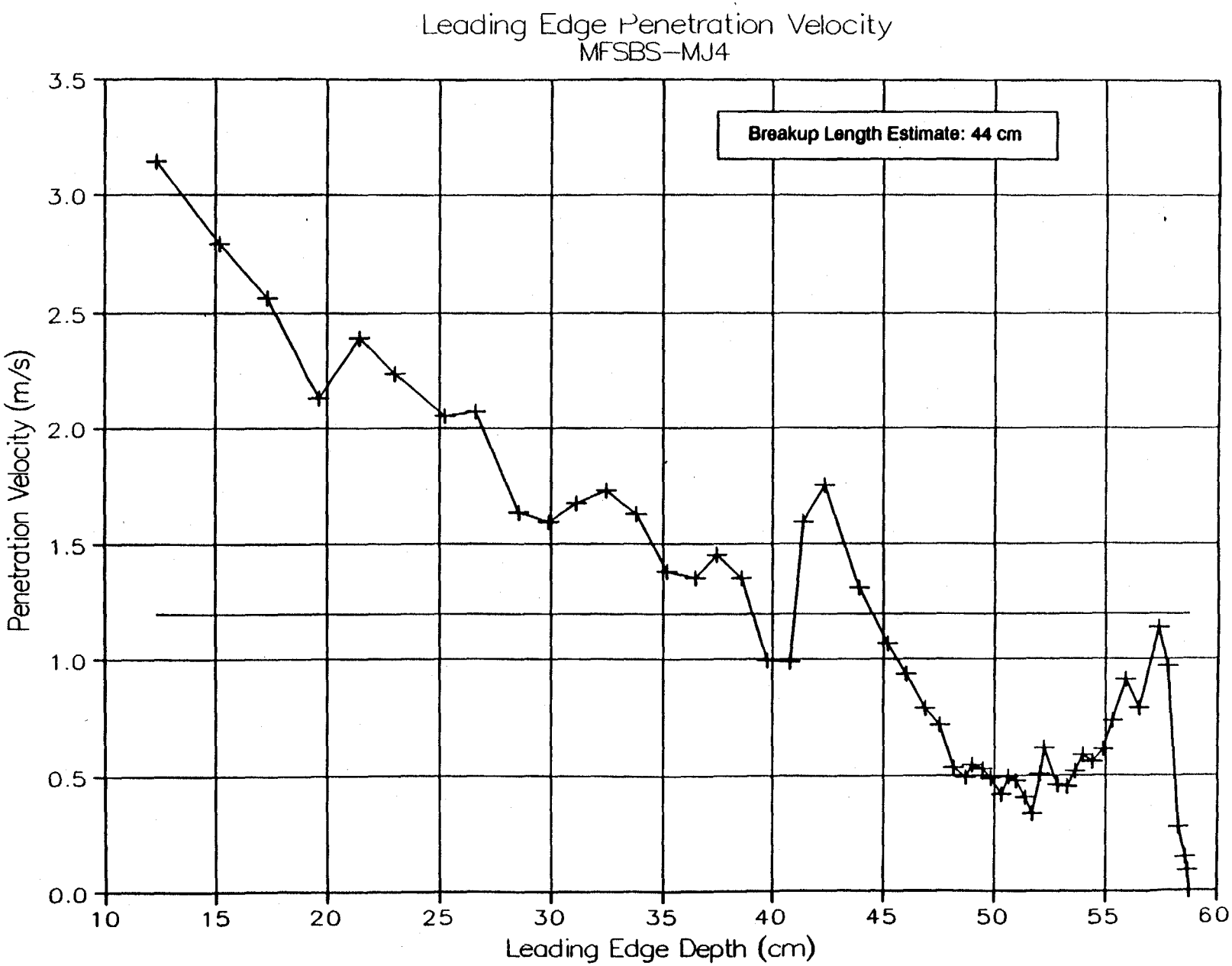
Leading Edge Penetration Velocity
MFSBS–MJ4
Breakup Length Estimate: 44 cm
Penetration Velocity (m/s)
Leading Edge Depth (cm)
0.0
0.5
1.0
1.5
2.0
2.5
3.0
3.5
10
15
20
25
30
35
40
45
50
55
60

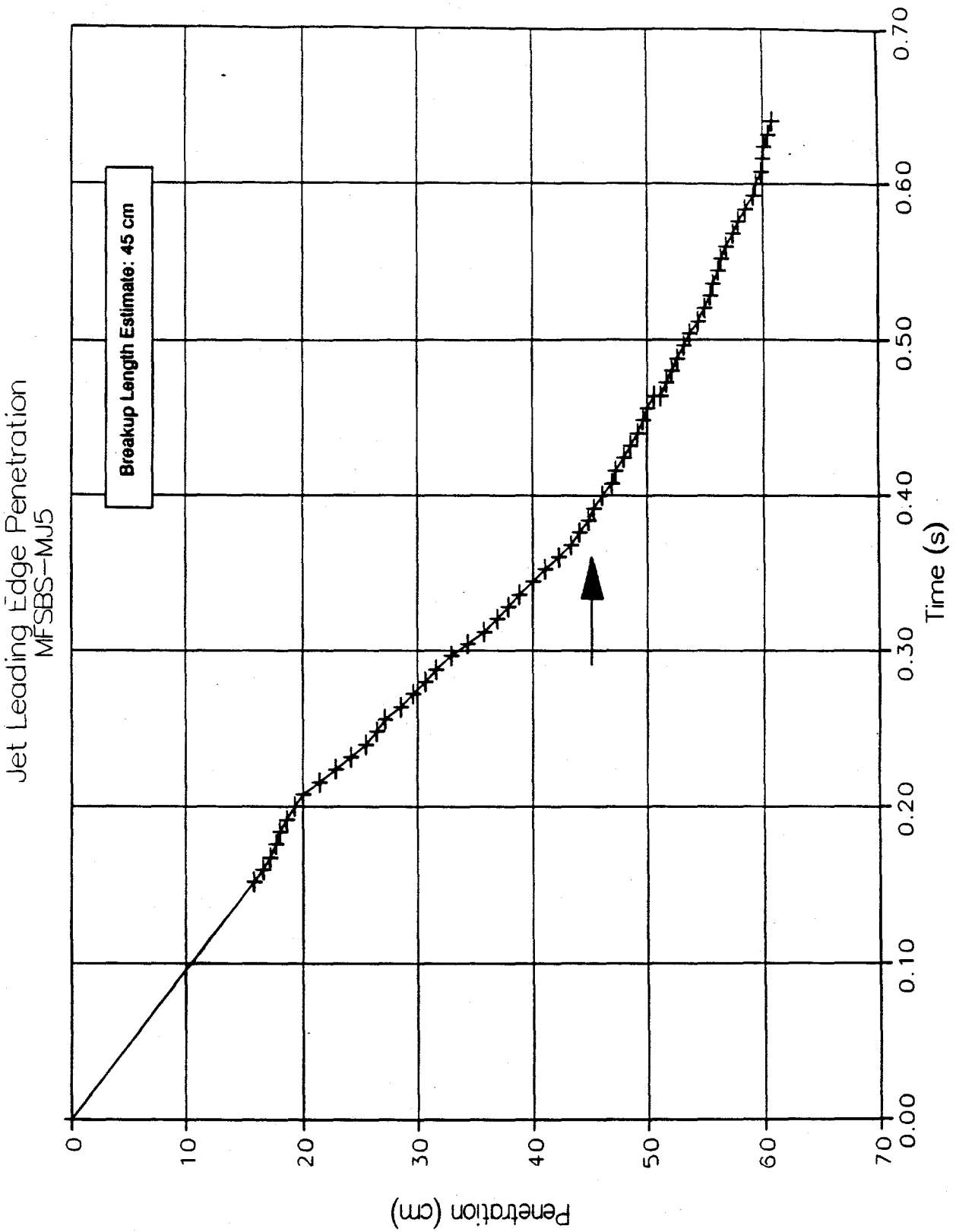
Jet Leading Edge Penetration
MFSBS-MJ5
Breakup Length Estimate: 45 cm
Penetration (cm)
0
10
20
30
40
50
60
70
Time (s)
0.00
0.10
0.20
0.30
0.40
0.50
0.60
0.70

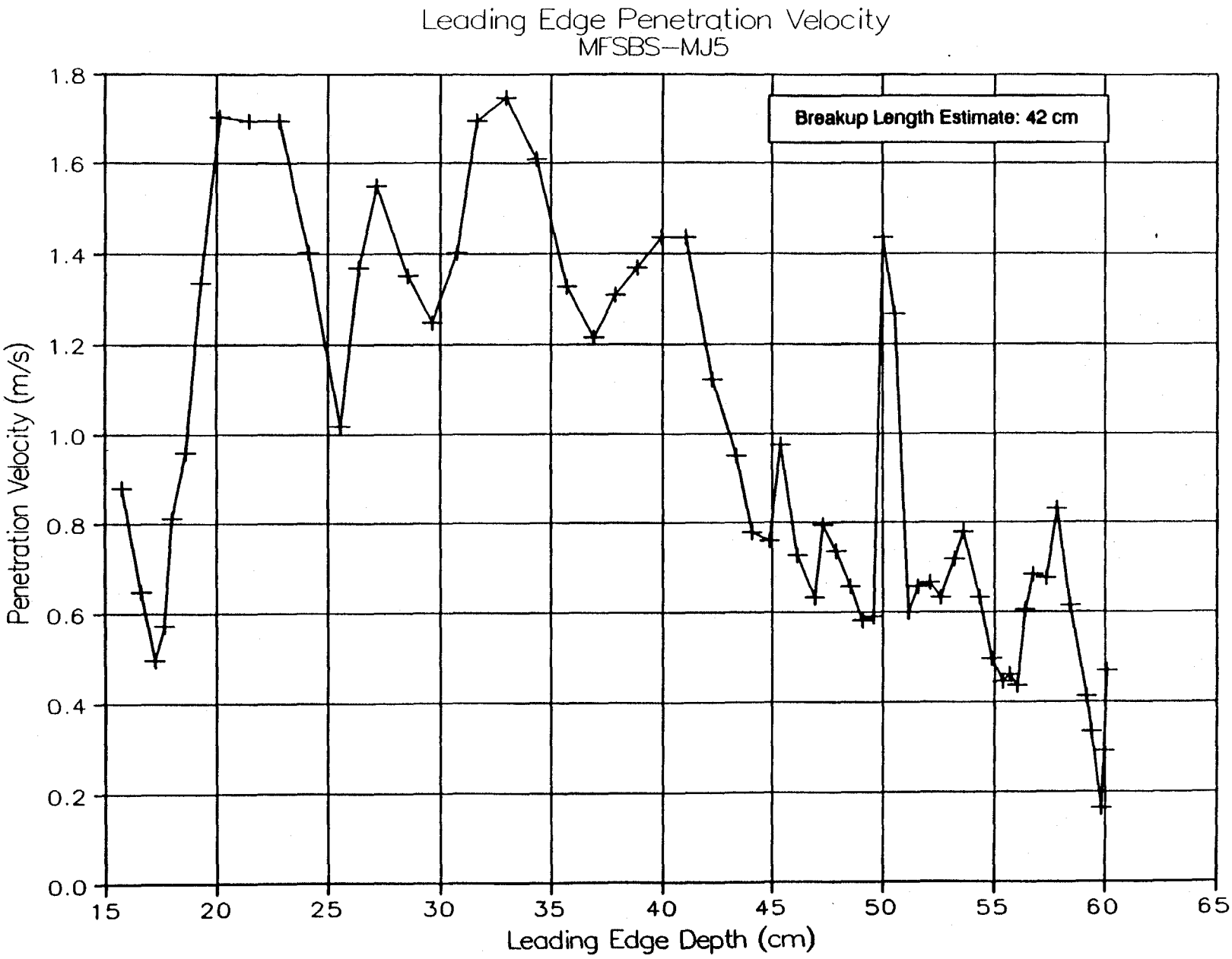
Leading Edge Penetration Velocity
MFSBS–MJ5
Breakup Length Estimate: 42 cm
Penetration Velocity (m/s)
Leading Edge Depth (cm)
0.0
0.2
0.4
0.6
0.8
1.0
1.2
1.4
1.6
1.8
15
20
25
30
35
40
45
50
55
60
65

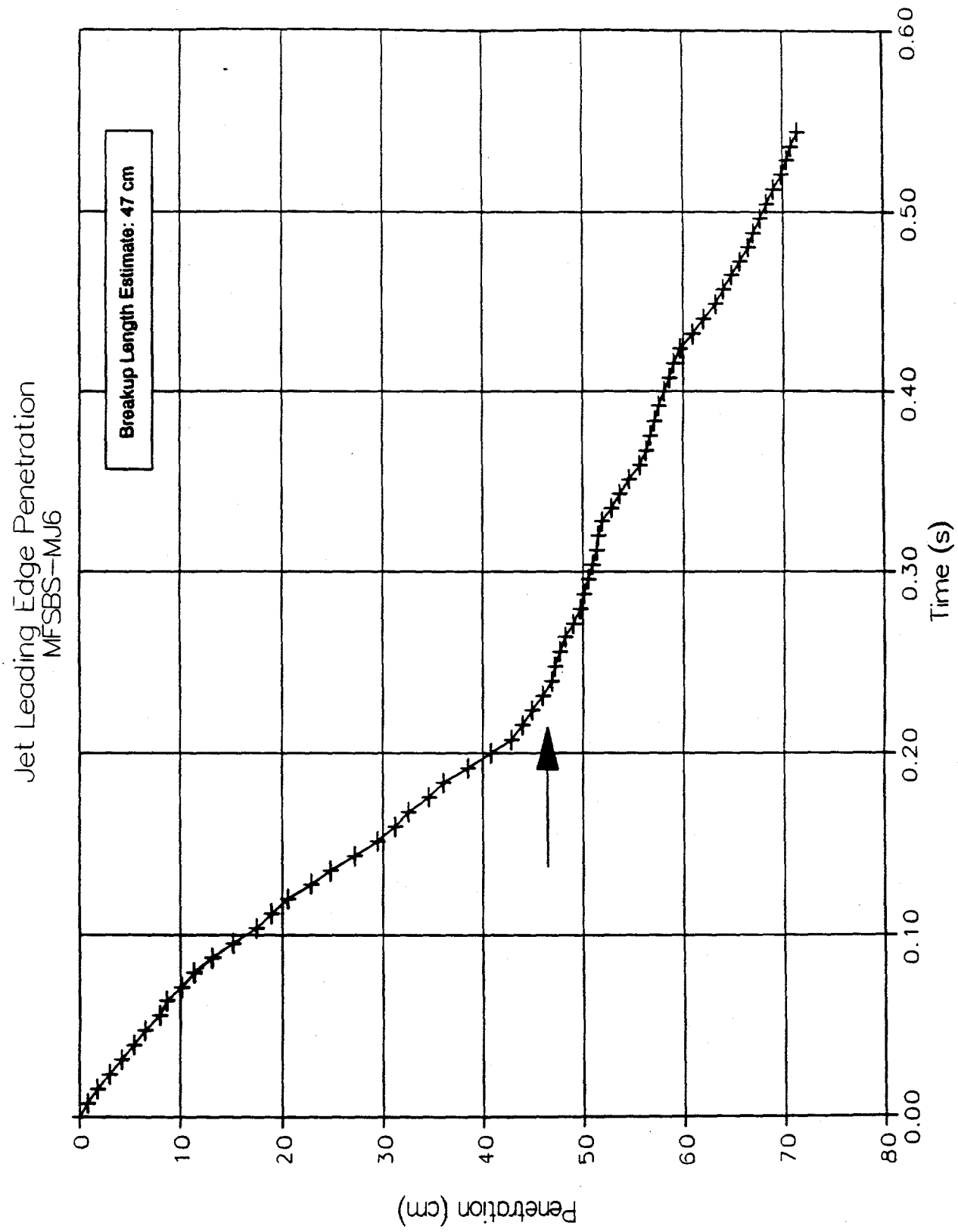
Jet Leading Edge Penetration
MFSBS-MJ6
Breakup Length Estimate: 47 cm
Penetration (cm)
0
10
20
30
40
50
60
70
80
0.00
0.10
0.20
0.30
0.40
0.50
0.60
Time (s)

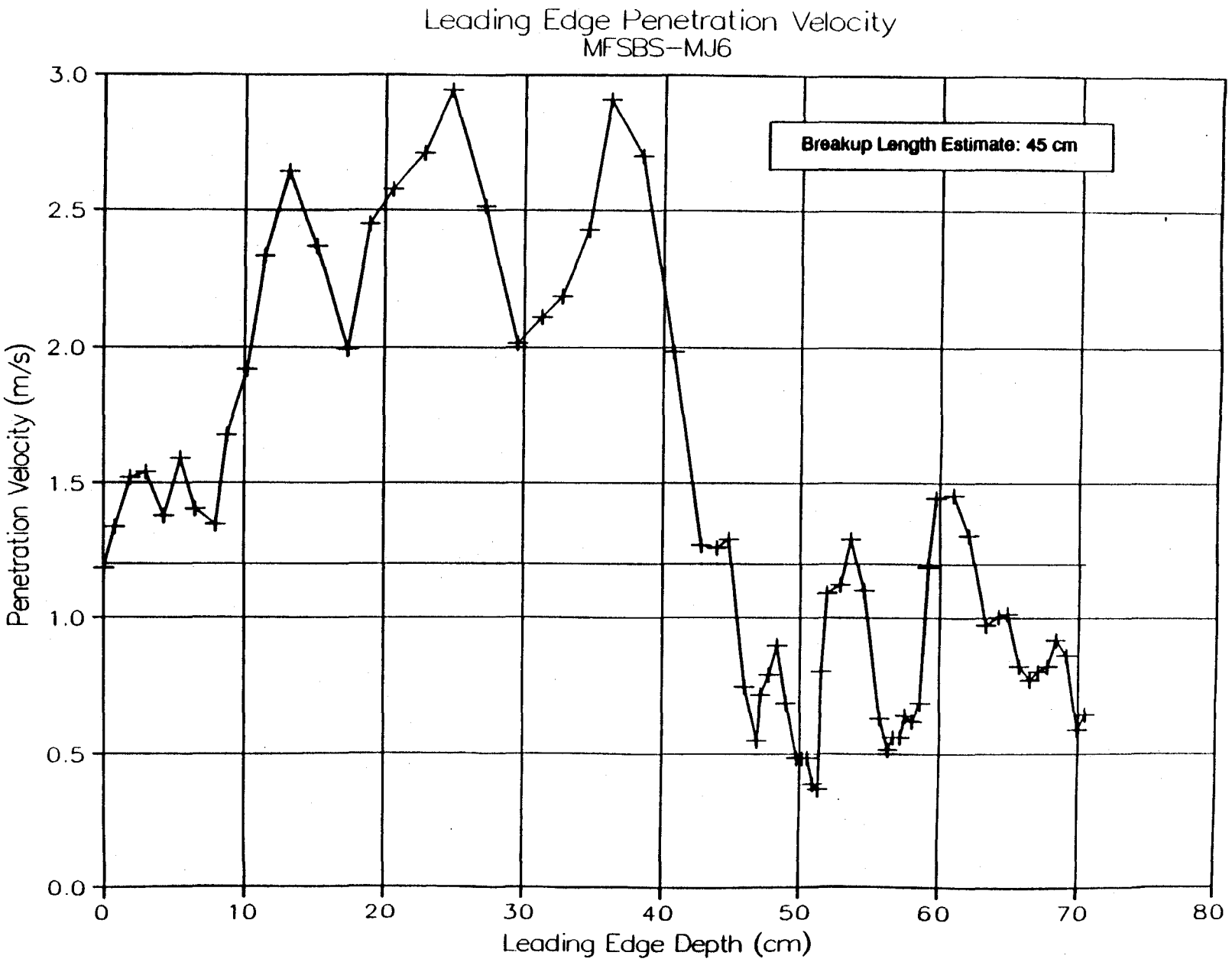
Leading Edge Penetration Velocity
MFSBS-MJ6
Breakup Length Estimate: 45 cm
Penetration Velocity (m/s)
3.0
2.5
2.0
1.5
1.0
0.5
0.0
0
10
20
30
40
50
60
70
80
Leading Edge Depth (cm)

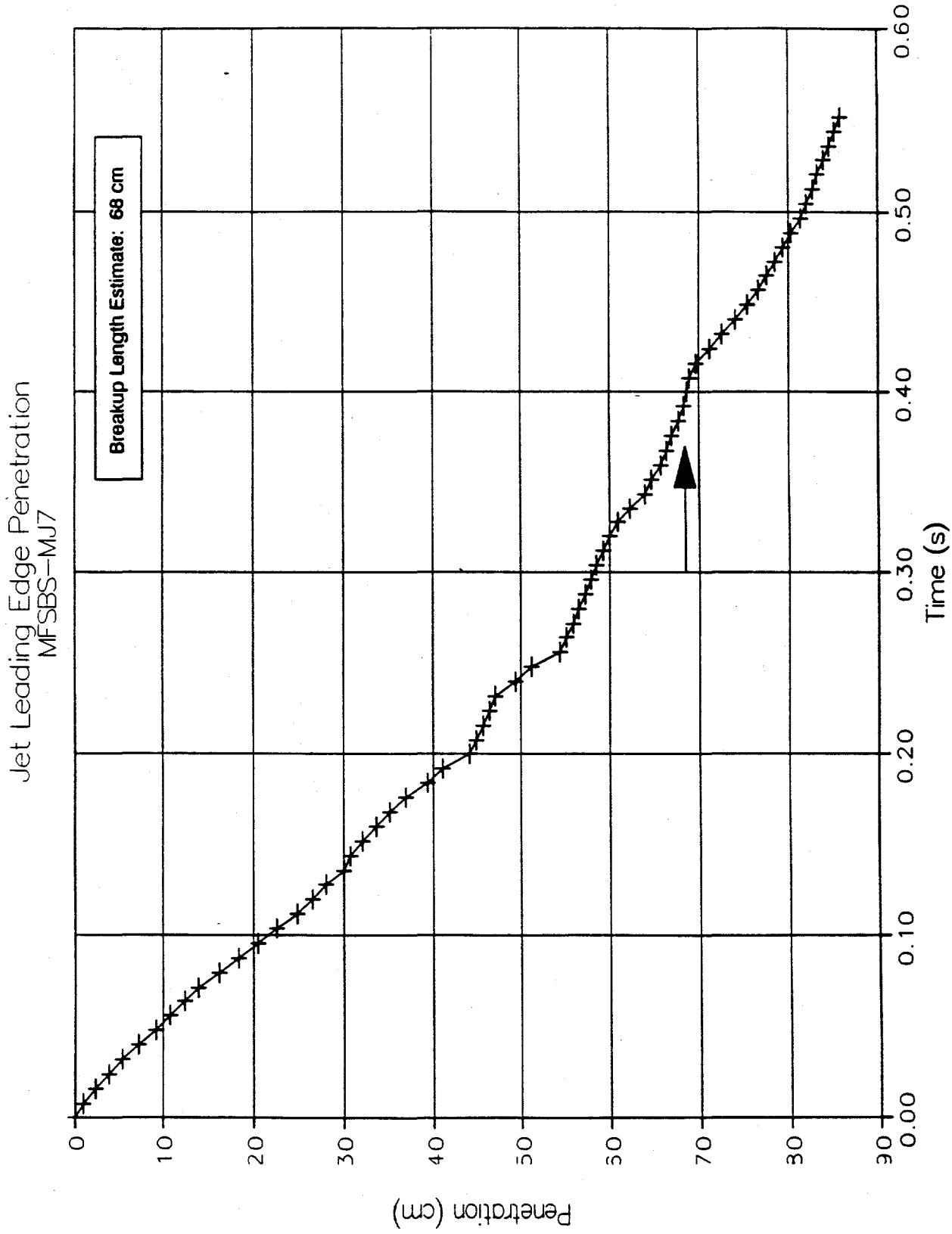
Jet Leading Edge Penetration
MFSBS-MJ7
Breakup Length Estimate: 68 cm
Penetration (cm)
0
10
20
30
40
50
60
70
80
90
Time (s)
0.00
0.10
0.20
0.30
0.40
0.50
0.60

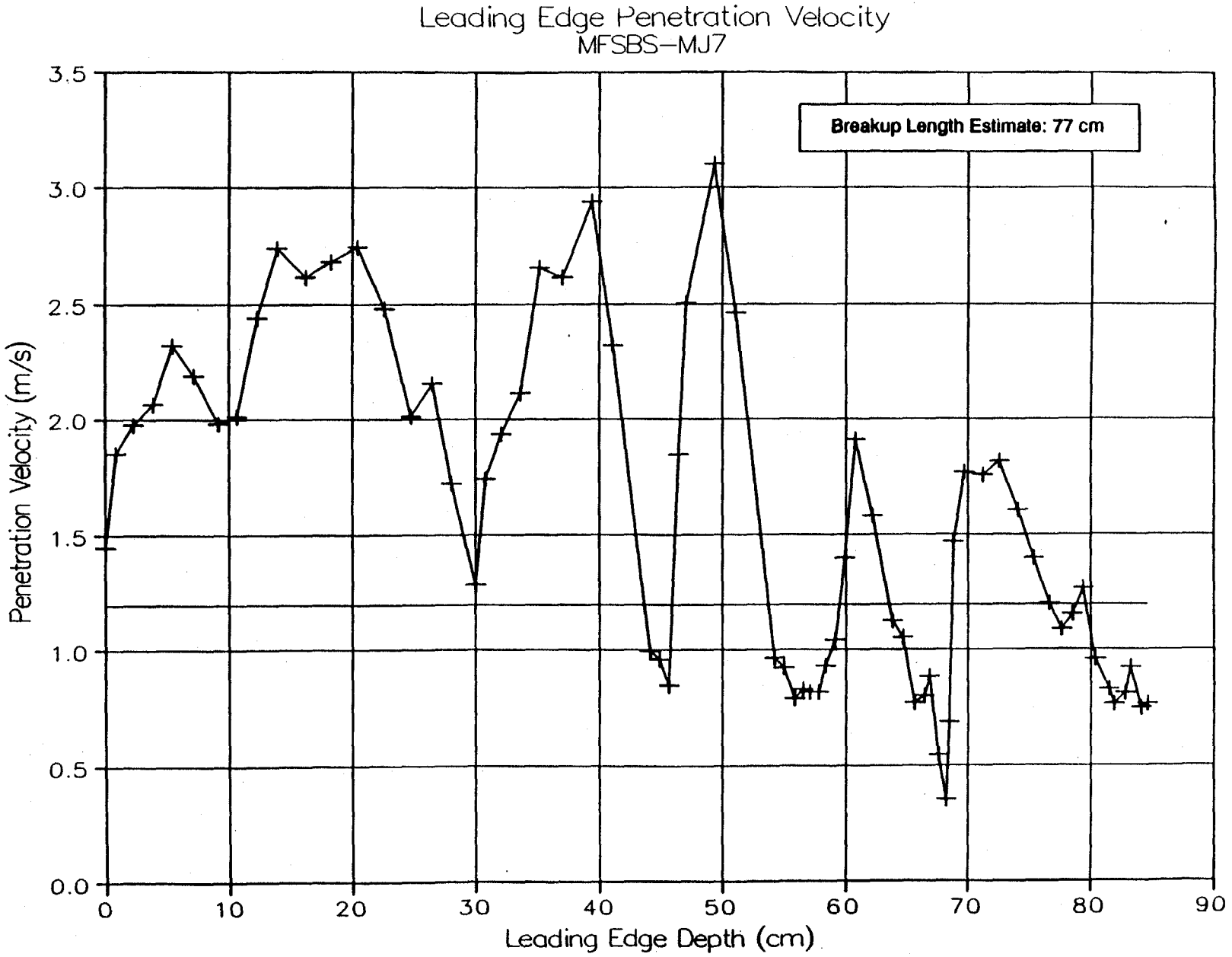
Leading Edge Penetration Velocity
MFSBS–MJ7
Breakup Length Estimate: 77 cm
Penetration Velocity (m/s)
Leading Edge Depth (cm)
0.0
0.5
1.0
1.5
2.0
2.5
3.0
3.5
0
10
20
30
40
50
60
70
80
90

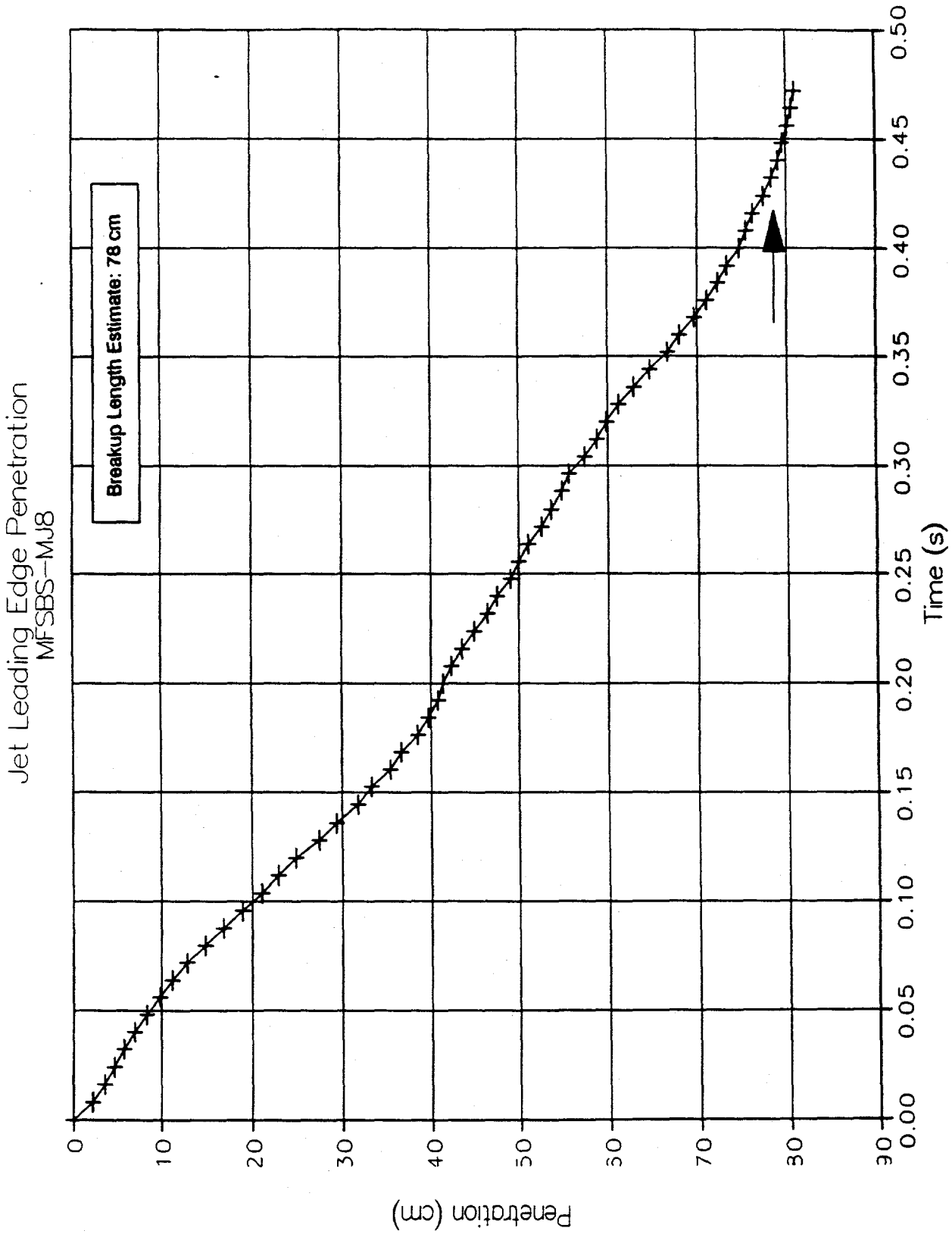
Jet Leading Edge Penetration
MFSBS-MJ8
Breakup Length Estimate: 78 cm
Penetration (cm)
0
10
20
30
40
50
60
70
80
90
Time (s)
0.00
0.05
0.10
0.15
0.20
0.25
0.30
0.35
0.40
0.45
0.50

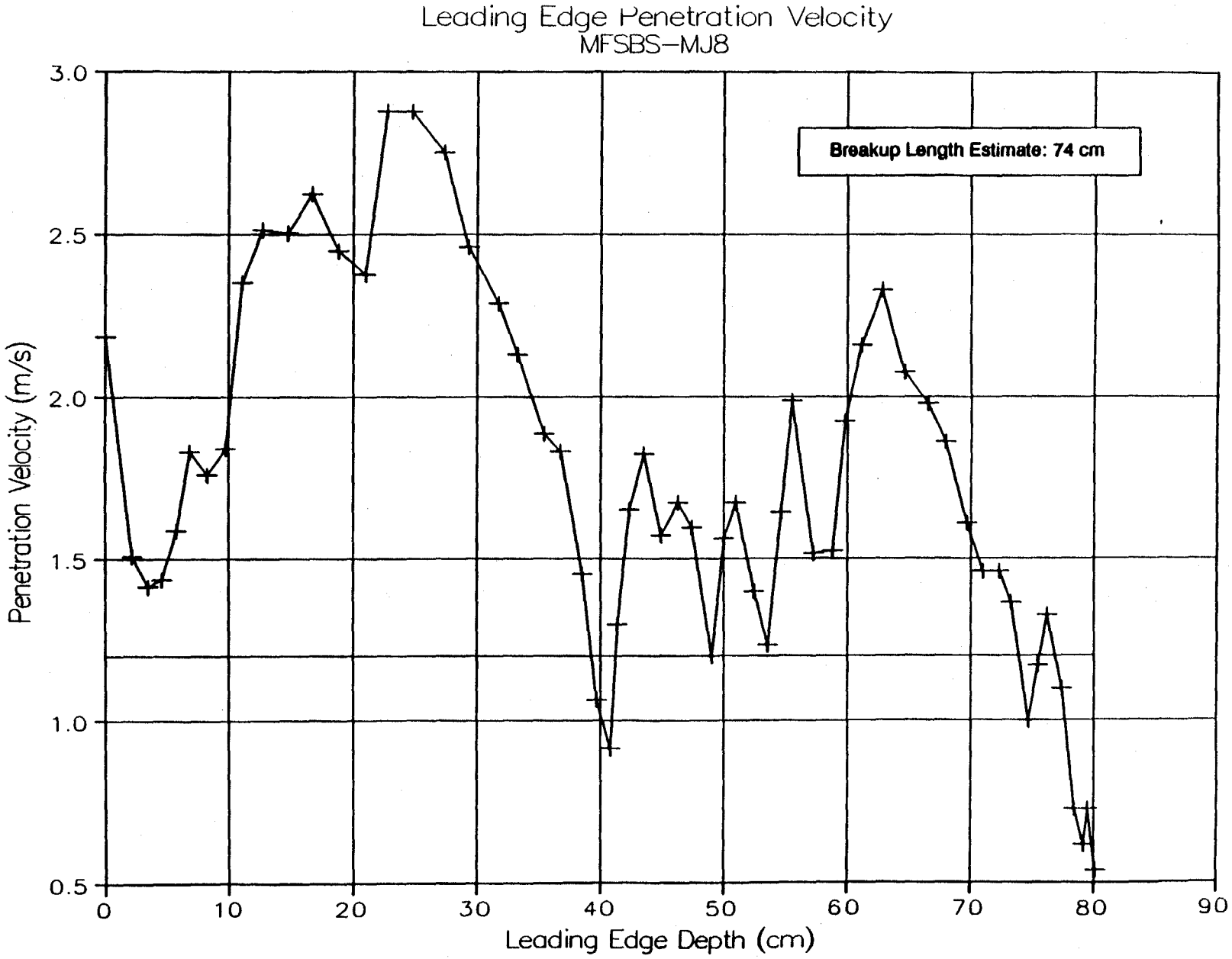
Leading Edge Penetration Velocity
MFSBS–MJ8
Breakup Length Estimate: 74 cm
Penetration Velocity (m/s)
3.0
2.5
2.0
1.5
1.0
0.5
0
10
20
30
40
50
60
70
80
90
Leading Edge Depth (cm)

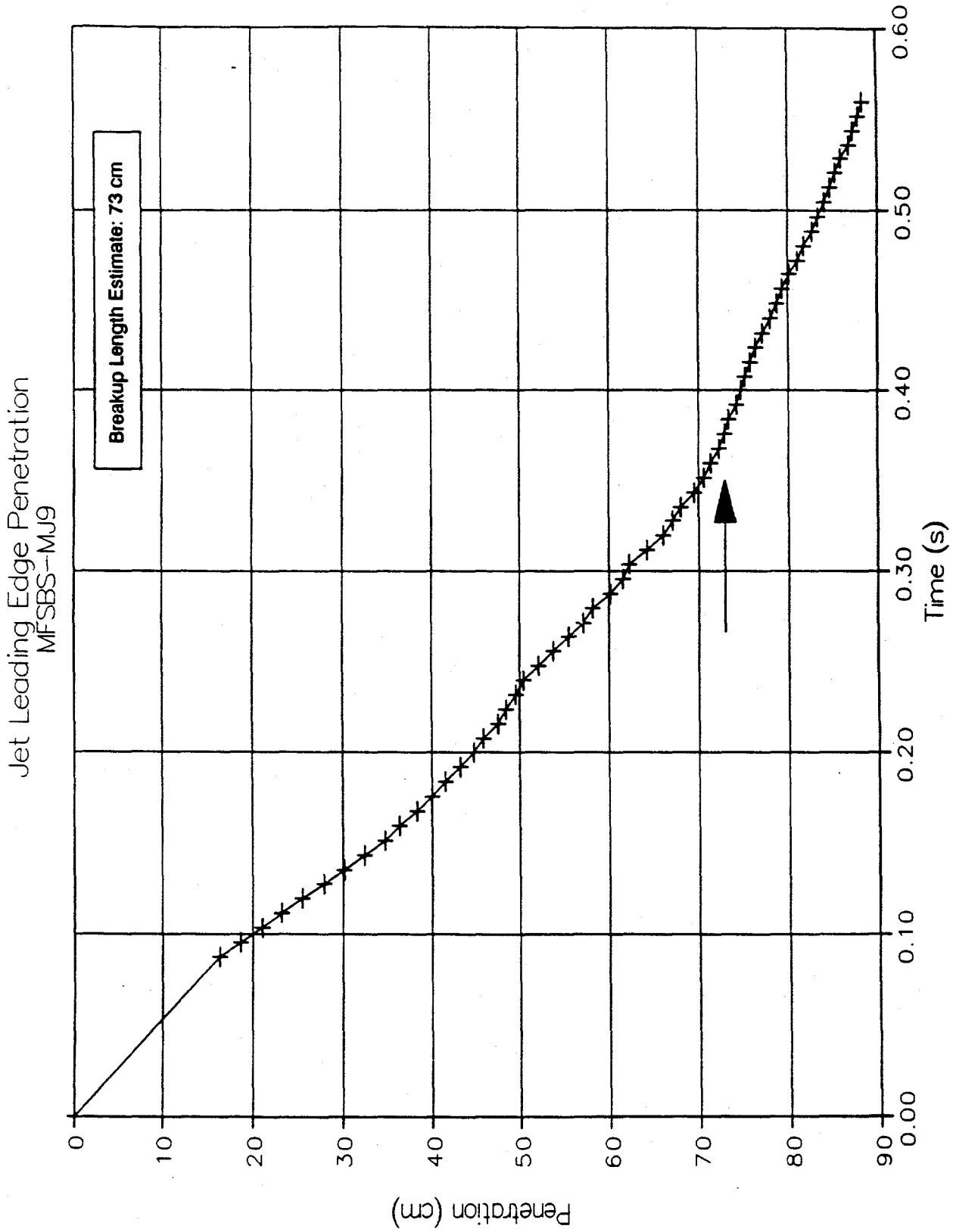
Jet Leading Edge Penetration
MFSBS-MJ9
Breakup Length Estimate: 73 cm
Penetration (cm)
0
10
20
30
40
50
60
70
80
90
Time (s)
0.00
0.10
0.20
0.30
0.40
0.50
0.60

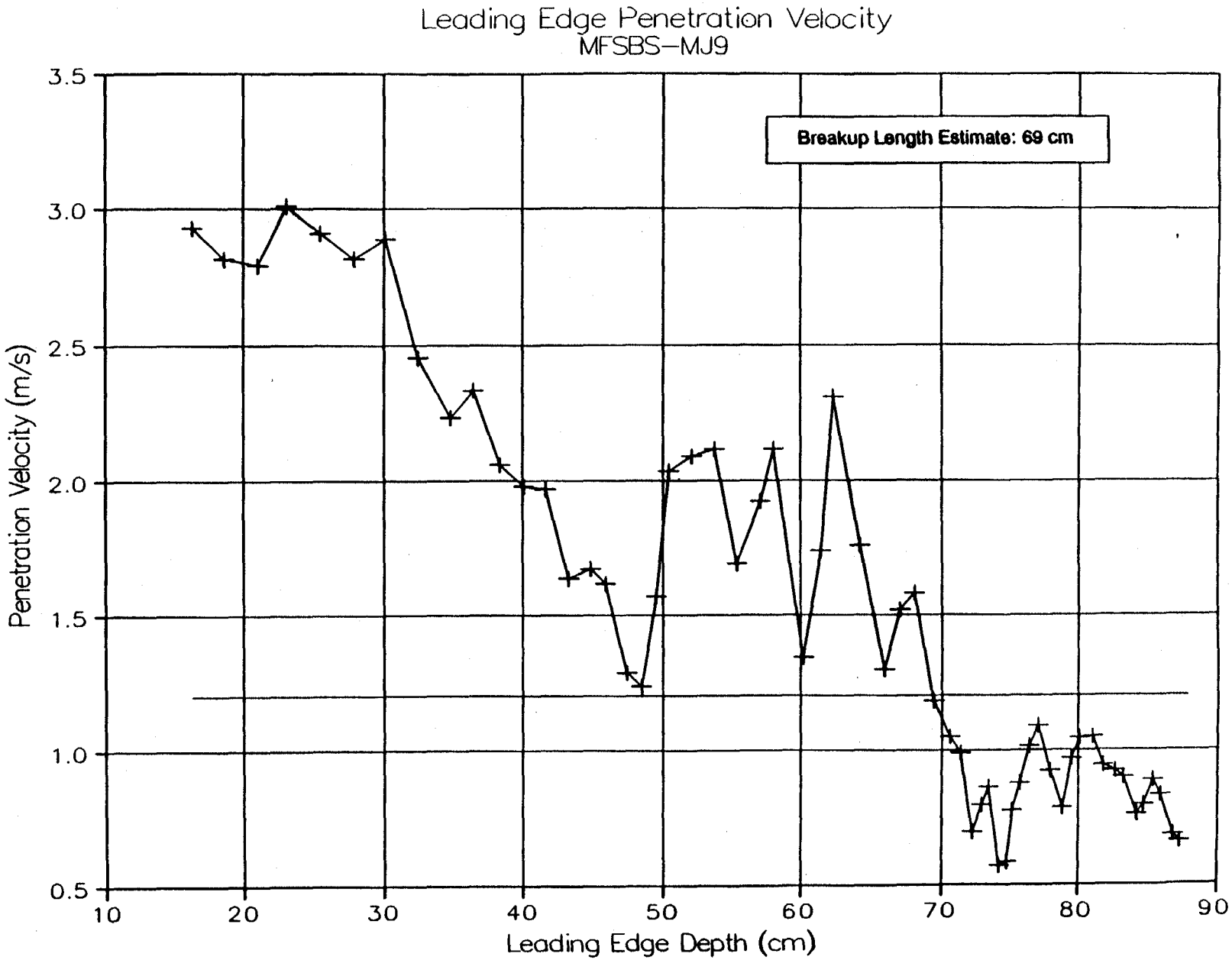
Leading Edge Penetration Velocity
MFSBS–MJ9
Breakup Length Estimate: 69 cm
Penetration Velocity (m/s)
3.5
3.0
2.5
2.0
1.5
1.0
0.5
10
20
30
40
50
60
70
80
90
Leading Edge Depth (cm)

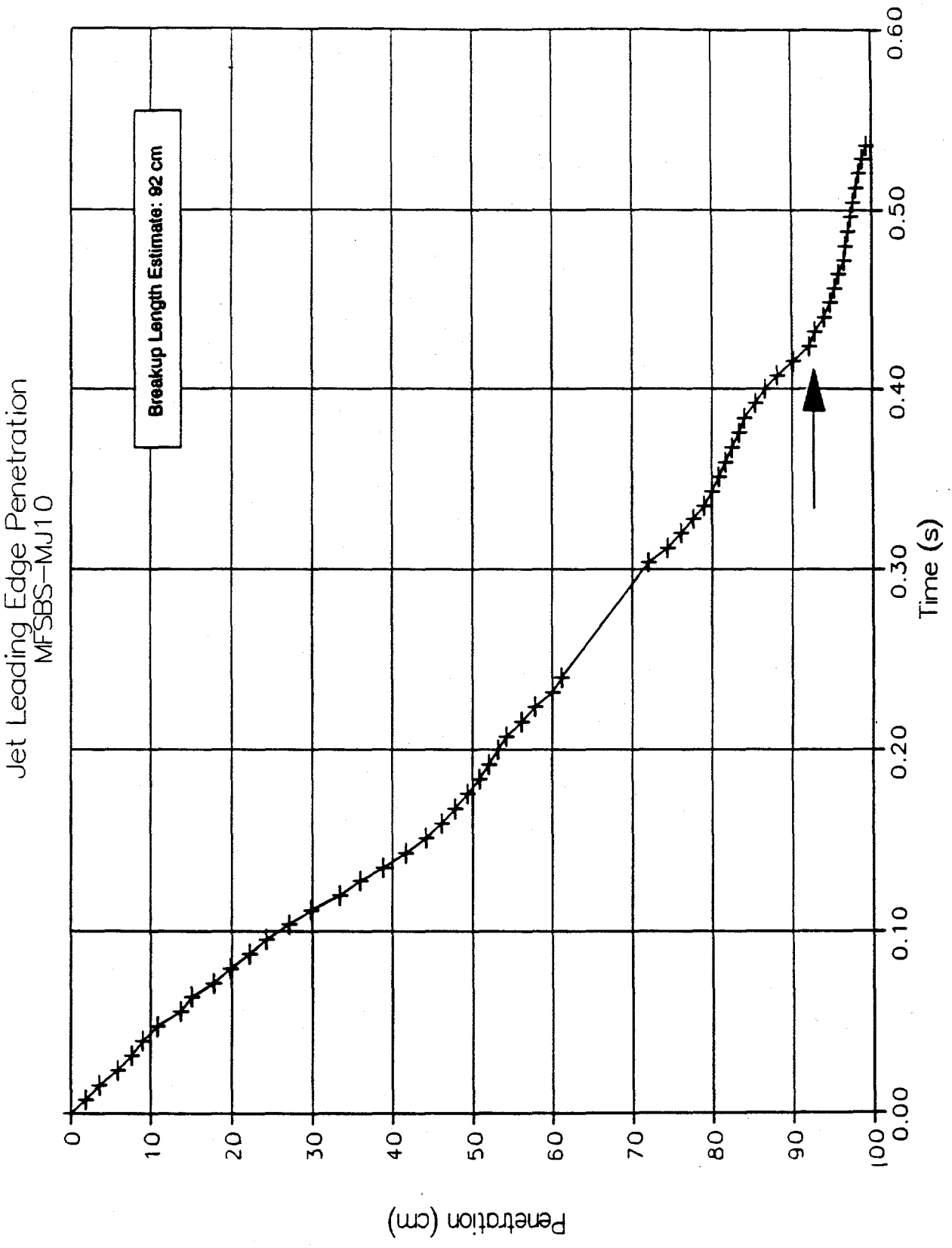
Jet Leading Edge Penetration
MFSBS-MJ10
Breakup Length Estimate: 92 cm
Penetration (cm)
Time (s)
0
10
20
30
40
50
60
70
80
90
100
0.00
0.10
0.20
0.30
0.40
0.50
0.60

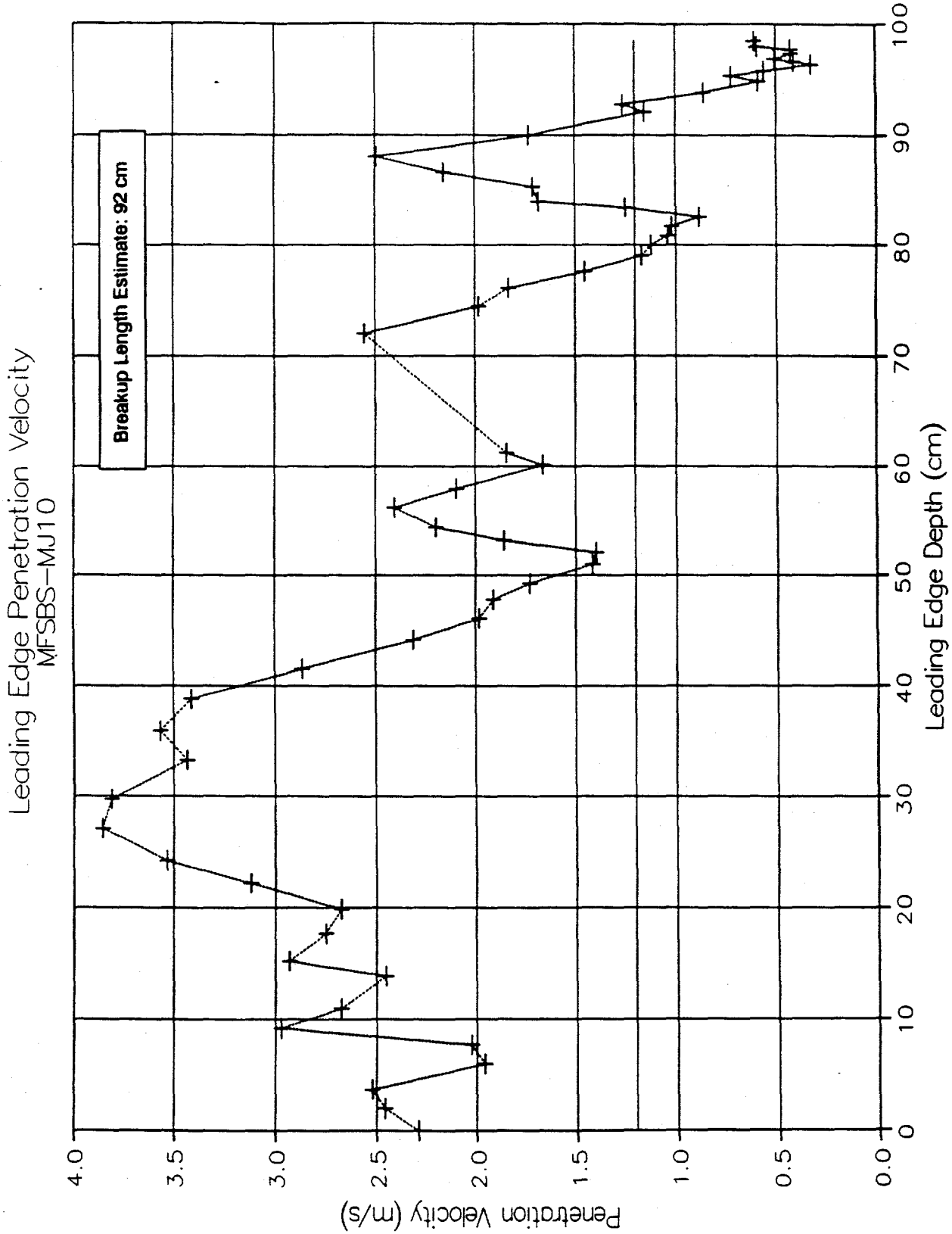
Leading Edge Penetration Velocity
MFSBS-MJ10
Breakup Length Estimate: 92 cm
Penetration Velocity (m/s)
Leading Edge Depth (cm)
0.0
0.5
1.0
1.5
2.0
2.5
3.0
3.5
4.0
0
10
20
30
40
50
60
70
80
90
100

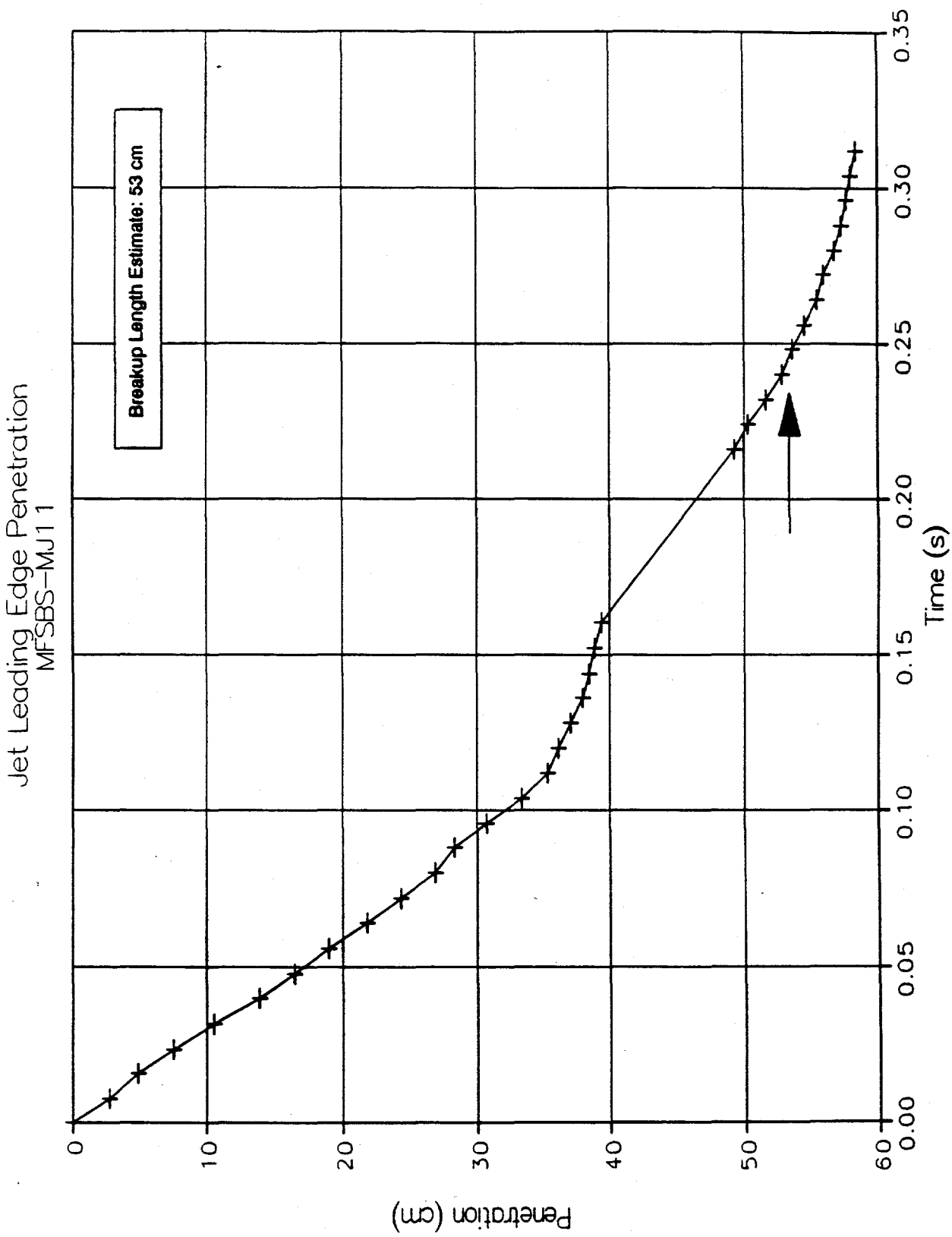
Jet Leading Edge Penetration
MFSBS-MJ11
Breakup Length Estimate: 53 cm
Penetration (cm)
0
10
20
30
40
50
60
Time (s)
0.00
0.05
0.10
0.15
0.20
0.25
0.30
0.35

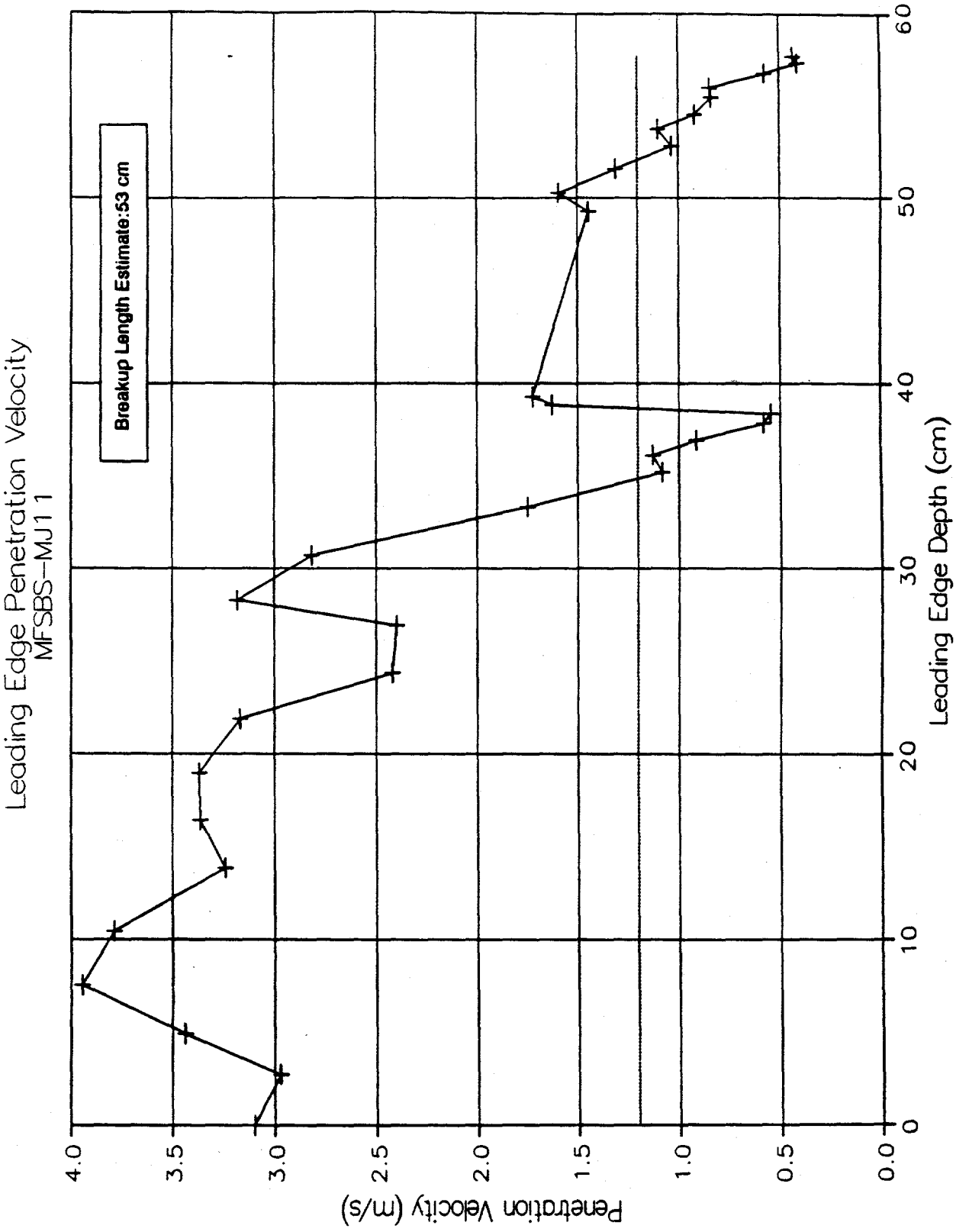
Leading Edge Penetration Velocity
MFSBS-MJ11
Breakup Length Estimate:53 cm
Penetration Velocity (m/s)
Leading Edge Depth (cm)
0.0
0.5
1.0
1.5
2.0
2.5
3.0
3.5
4.0
0
10
20
30
40
50
60

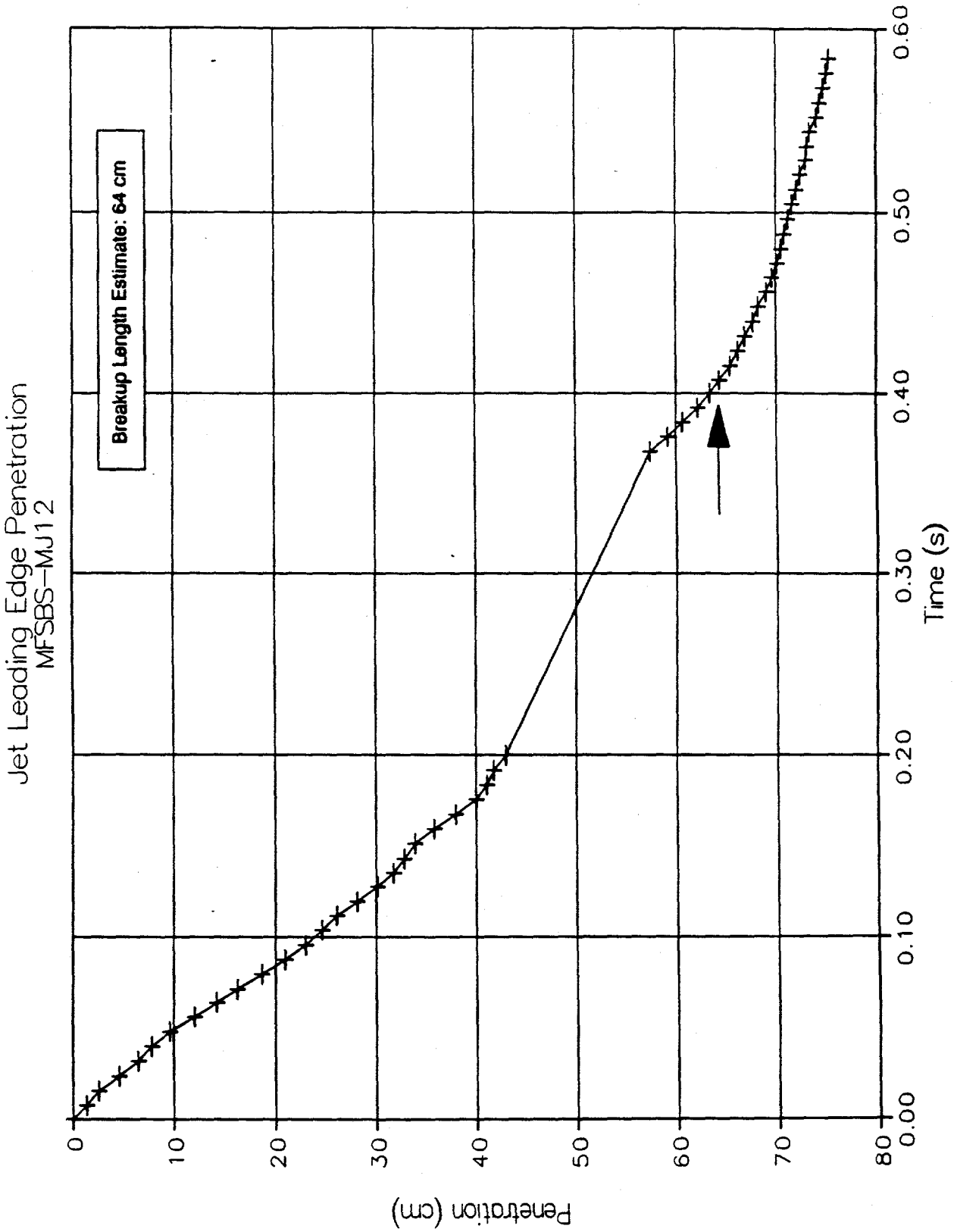
Jet Leading Edge Penetration
MFSBS–MJ12
Breakup Length Estimate: 64 cm
Penetration (cm)
0
10
20
30
40
50
60
70
80
0.00
0.10
0.20
0.30
0.40
0.50
0.60
Time (s)

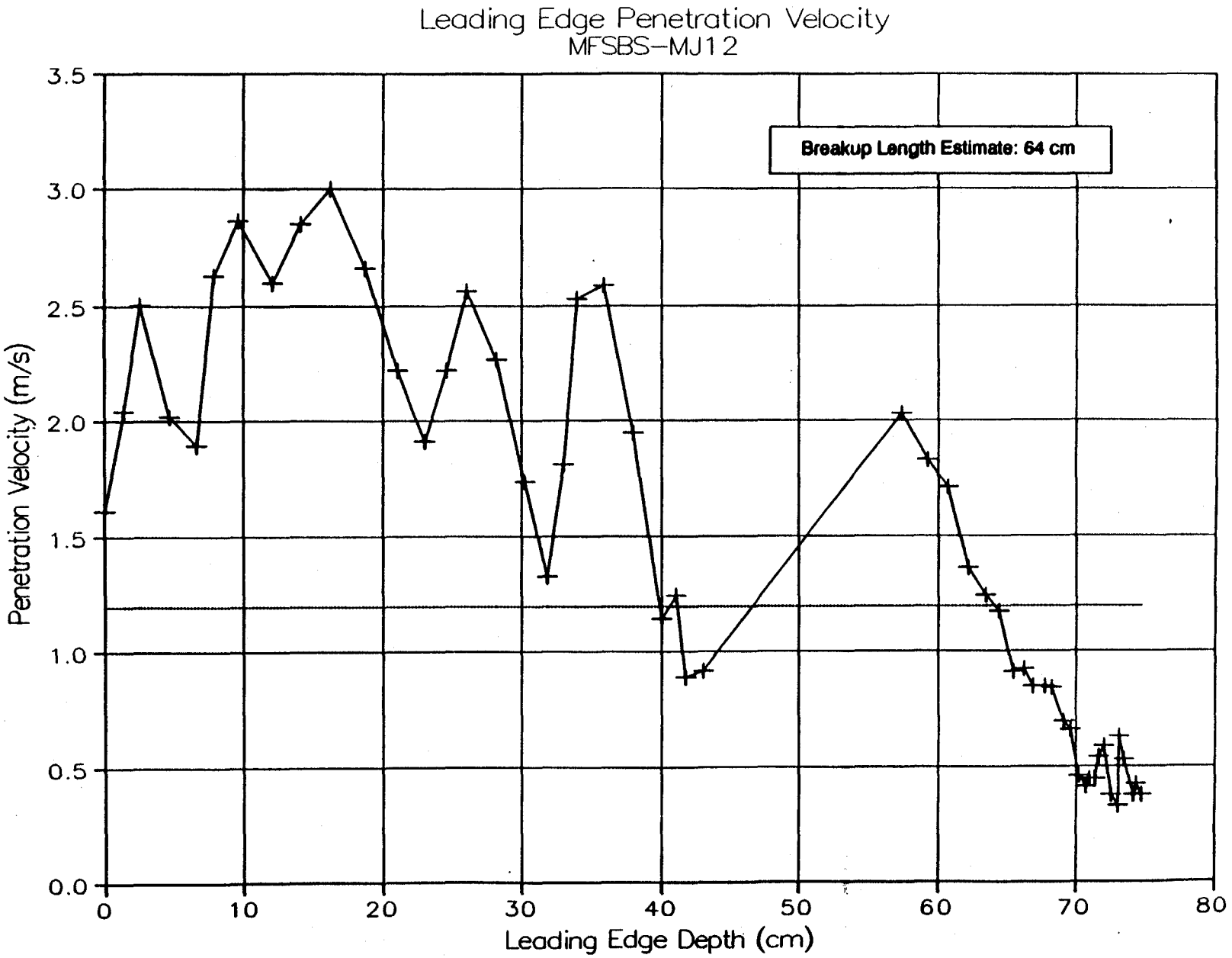
Leading Edge Penetration Velocity
MFSBS–MJ12
Breakup Length Estimate: 64 cm
Penetration Velocity (m/s)
Leading Edge Depth (cm)
0.0
0.5
1.0
1.5
2.0
2.5
3.0
3.5
0
10
20
30
40
50
60
70
80

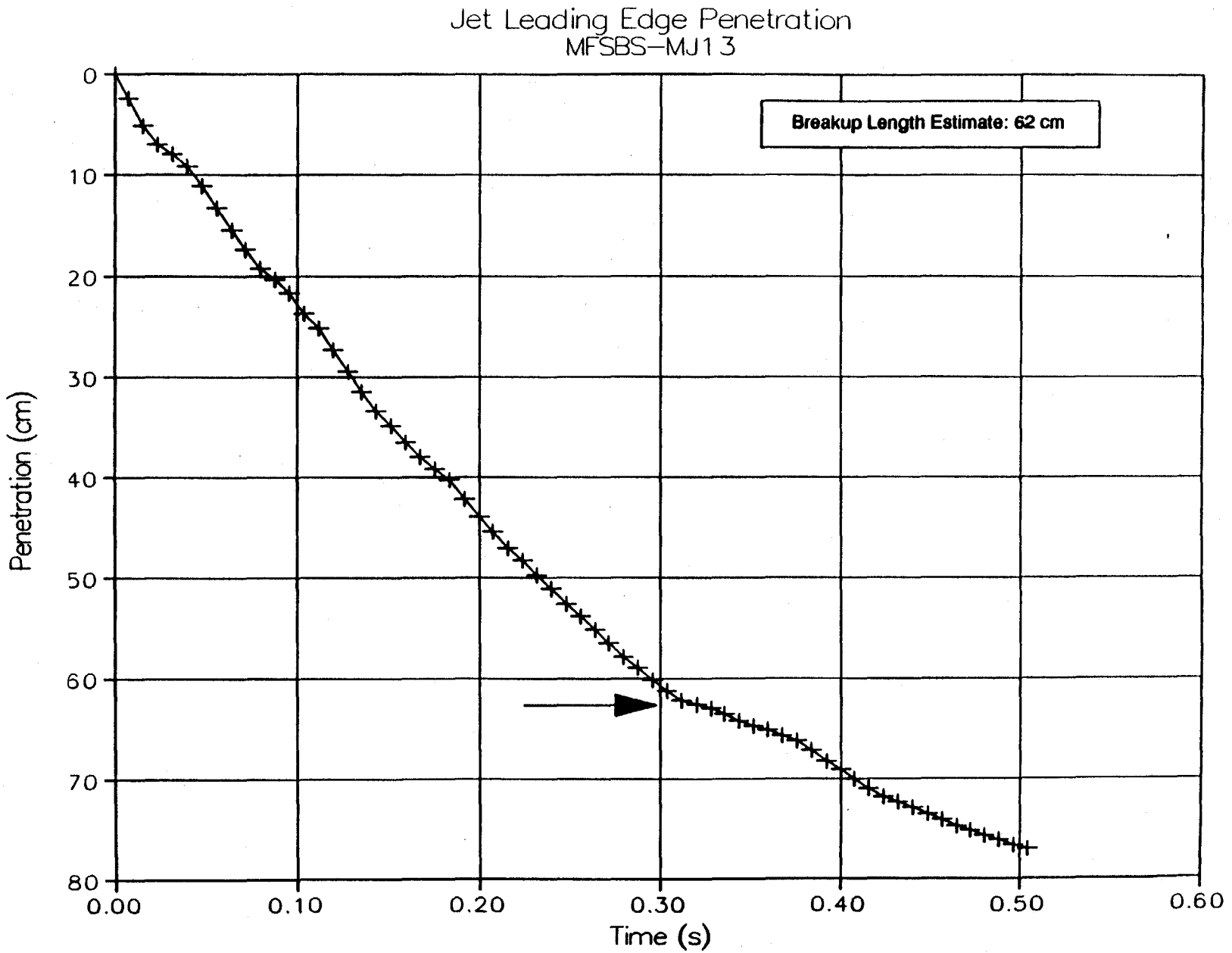
Jet Leading Edge Penetration
MFSBS-MJ13
Breakup Length Estimate: 62 cm
Penetration (cm)
Time (s)
0
10
20
30
40
50
60
70
80
0.00
0.10
0.20
0.30
0.40
0.50
0.60

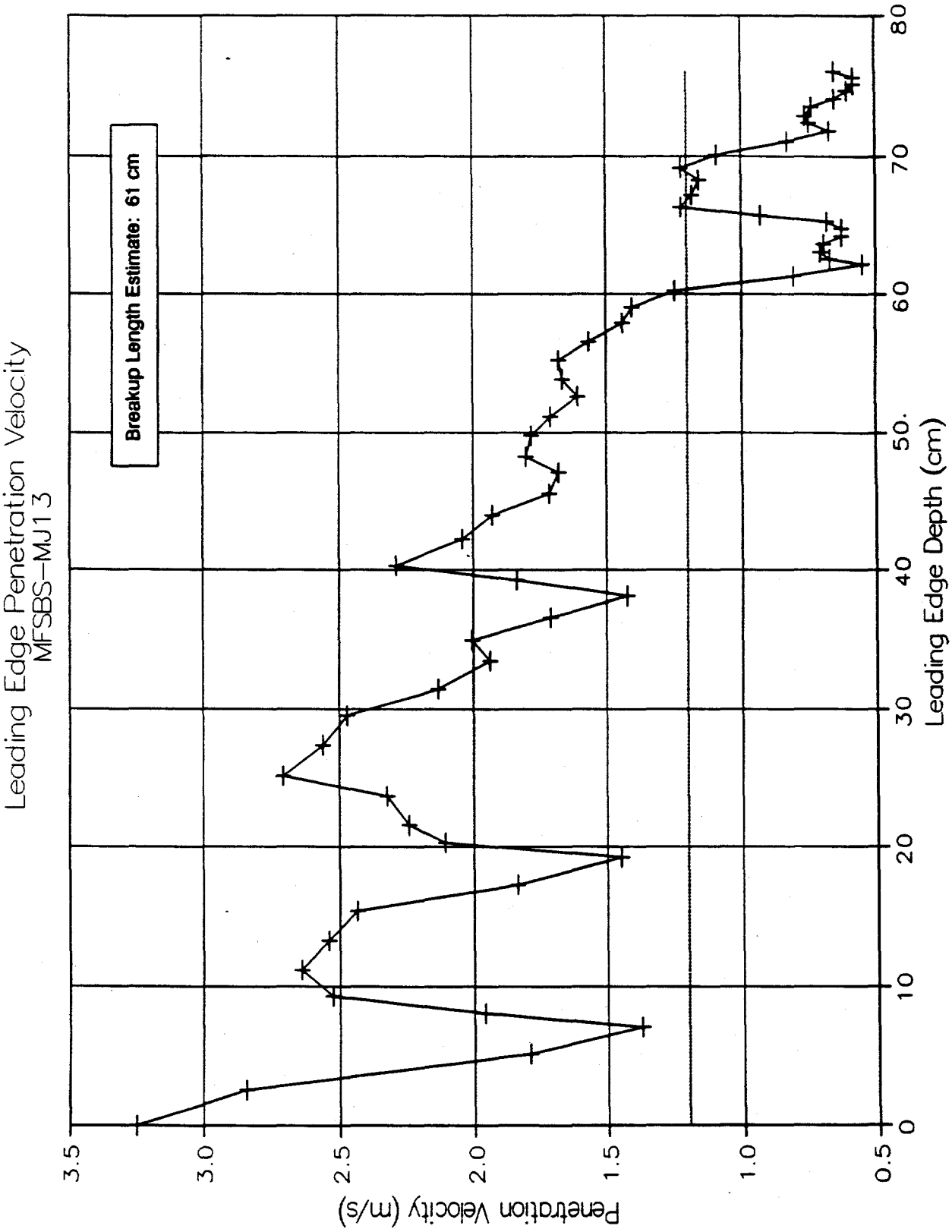
Leading Edge Penetration Velocity
MFSBS–MJ13
Breakup Length Estimate: 61 cm
Penetration Velocity (m/s)
Leading Edge Depth (cm)
3.5
3.0
2.5
2.0
1.5
1.0
0.5
0
10
20
30
40
50.
60
70
80

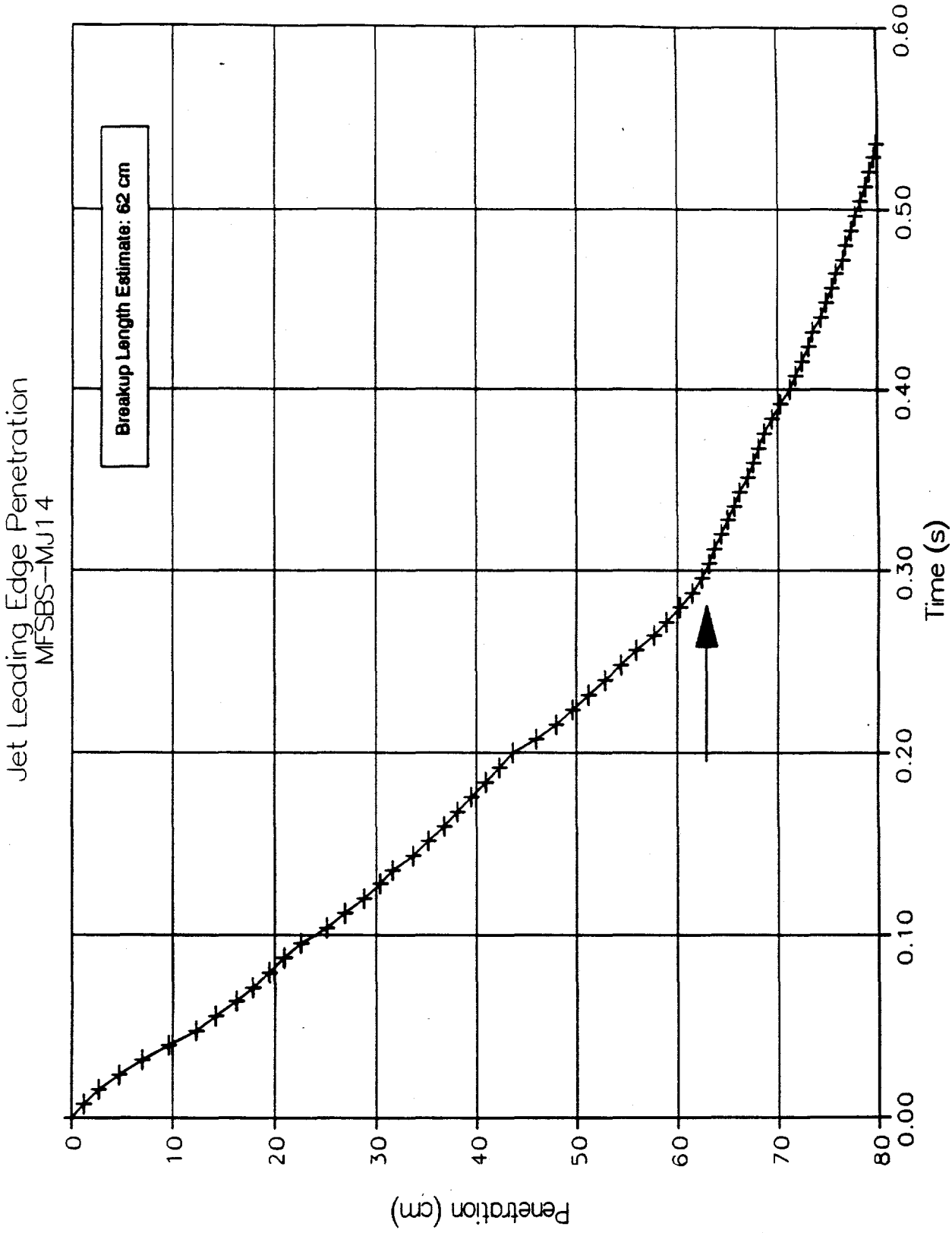
Jet Leading Edge Penetration
MFSBS-MJ14
Breakup Length Estimate: 62 cm
Penetration (cm)
0
10
20
30
40
50
60
70
80
Time (s)
0.00
0.10
0.20
0.30
0.40
0.50
0.60

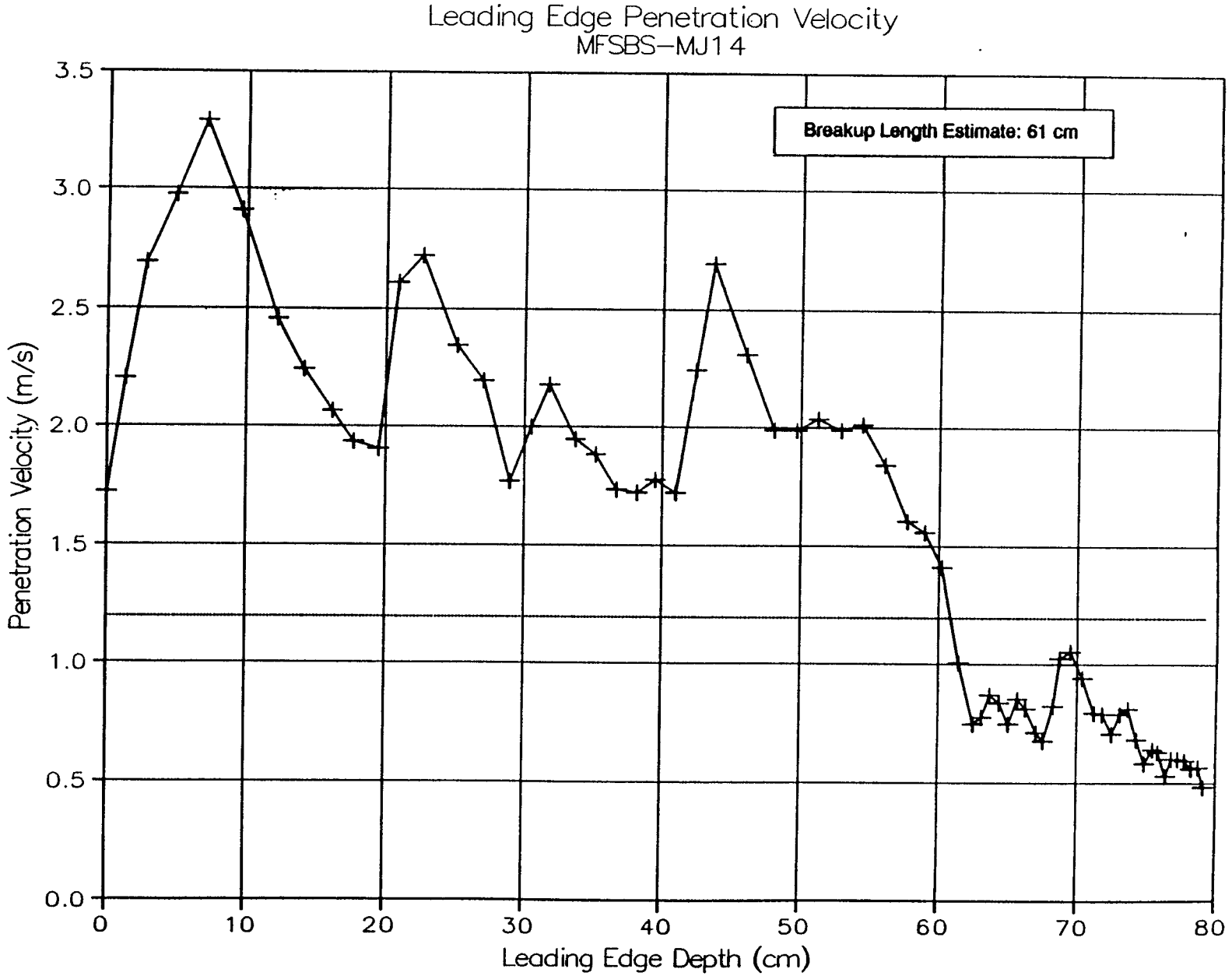
Leading Edge Penetration Velocity
MFSBS–MJ14
Breakup Length Estimate: 61 cm
Penetration Velocity (m/s)
Leading Edge Depth (cm)
0.0
0.5
1.0
1.5
2.0
2.5
3.0
3.5
0
10
20
30
40
50
60
70
80

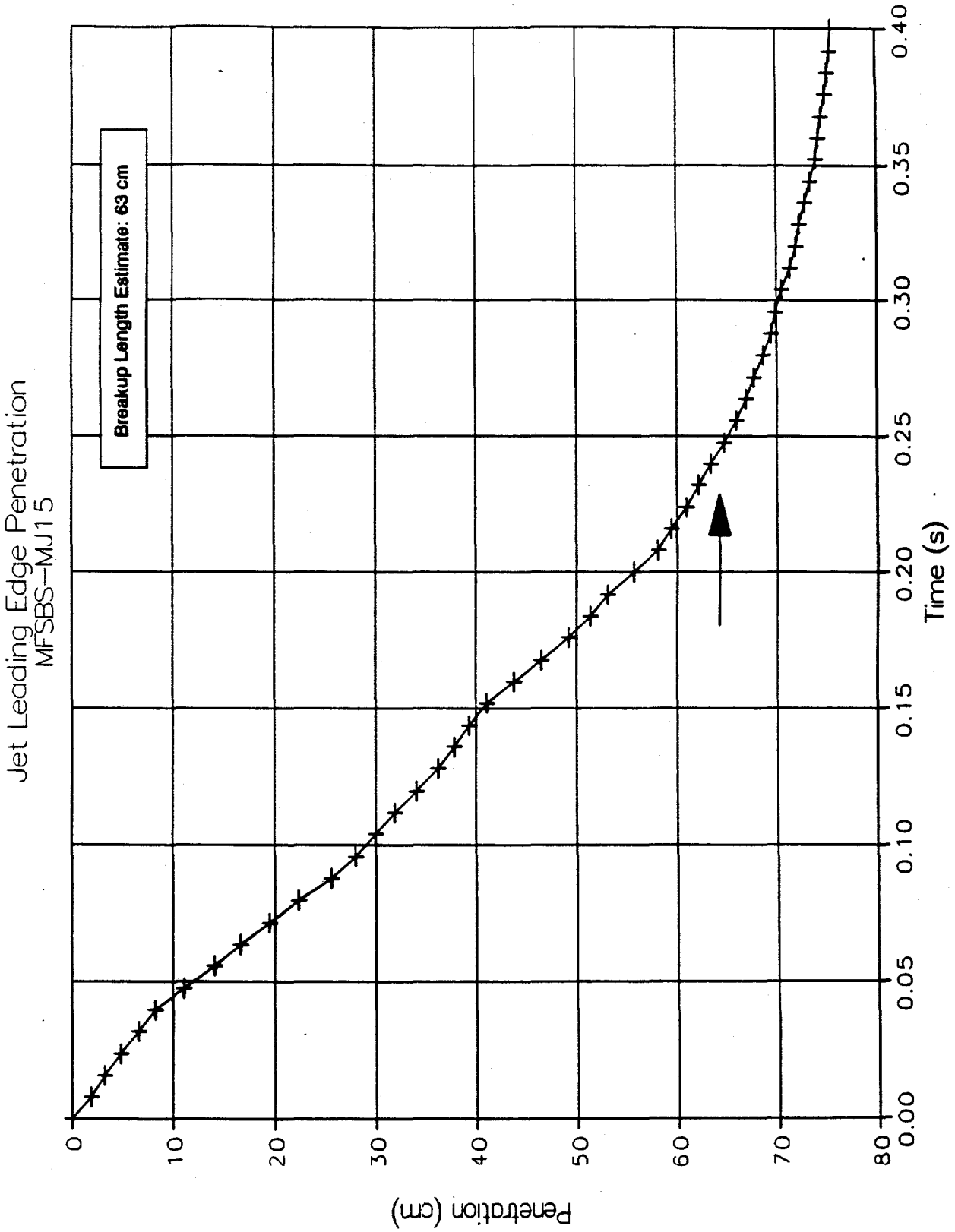
Jet Leading Edge Penetration
MFSBS-MJ15
Breakup Length Estimate: 63 cm
Penetration (cm)
0
10
20
30
40
50
60
70
80
0.00
0.05
0.10
0.15
0.20
0.25
0.30
0.35
0.40
Time (s)

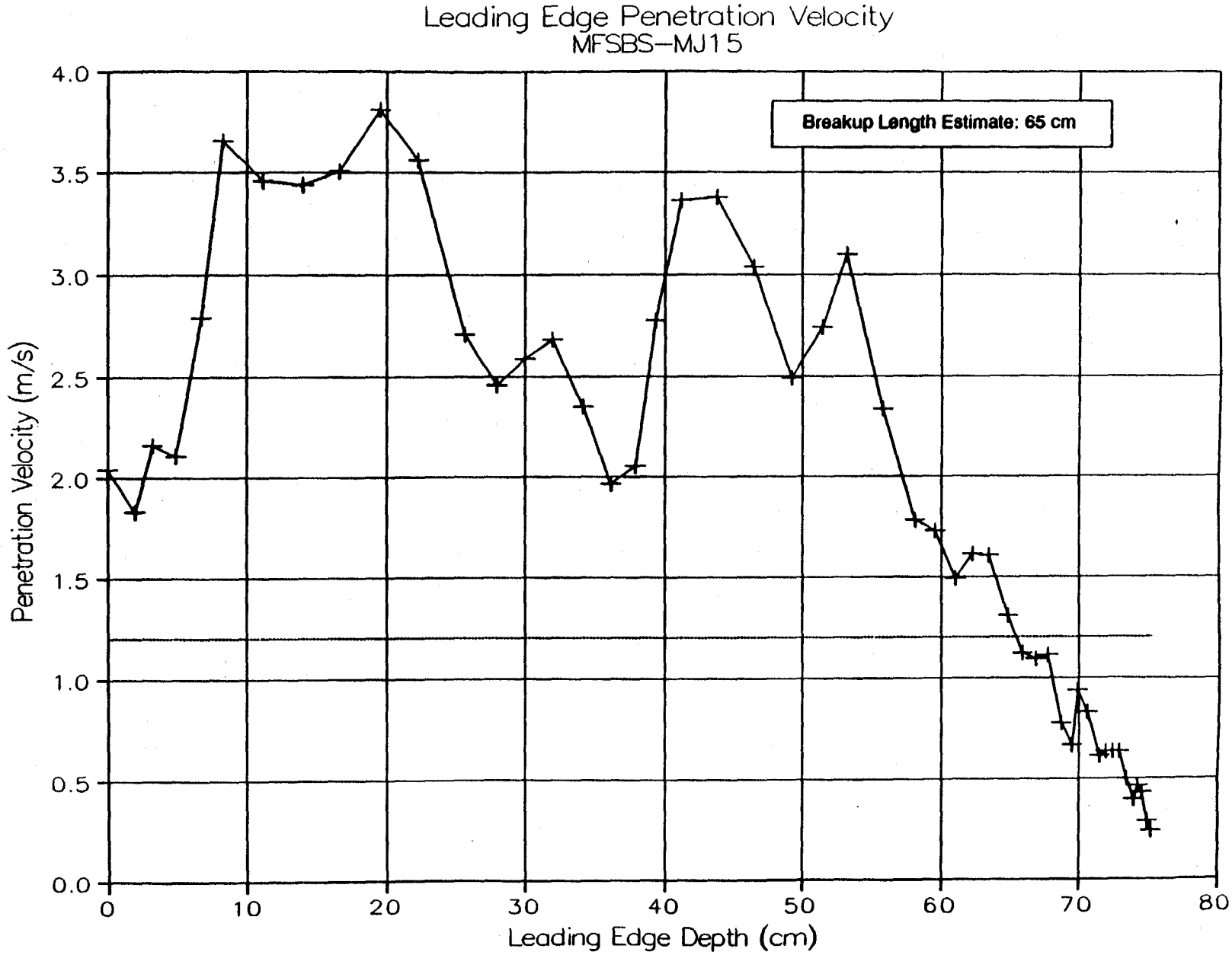
Leading Edge Penetration Velocity
MFSBS–MJ15
Breakup Length Estimate: 65 cm
Penetration Velocity (m/s)
Leading Edge Depth (cm)
4.0
3.5
3.0
2.5
2.0
1.5
1.0
0.5
0.0
0
10
20
30
40
50
60
70
80

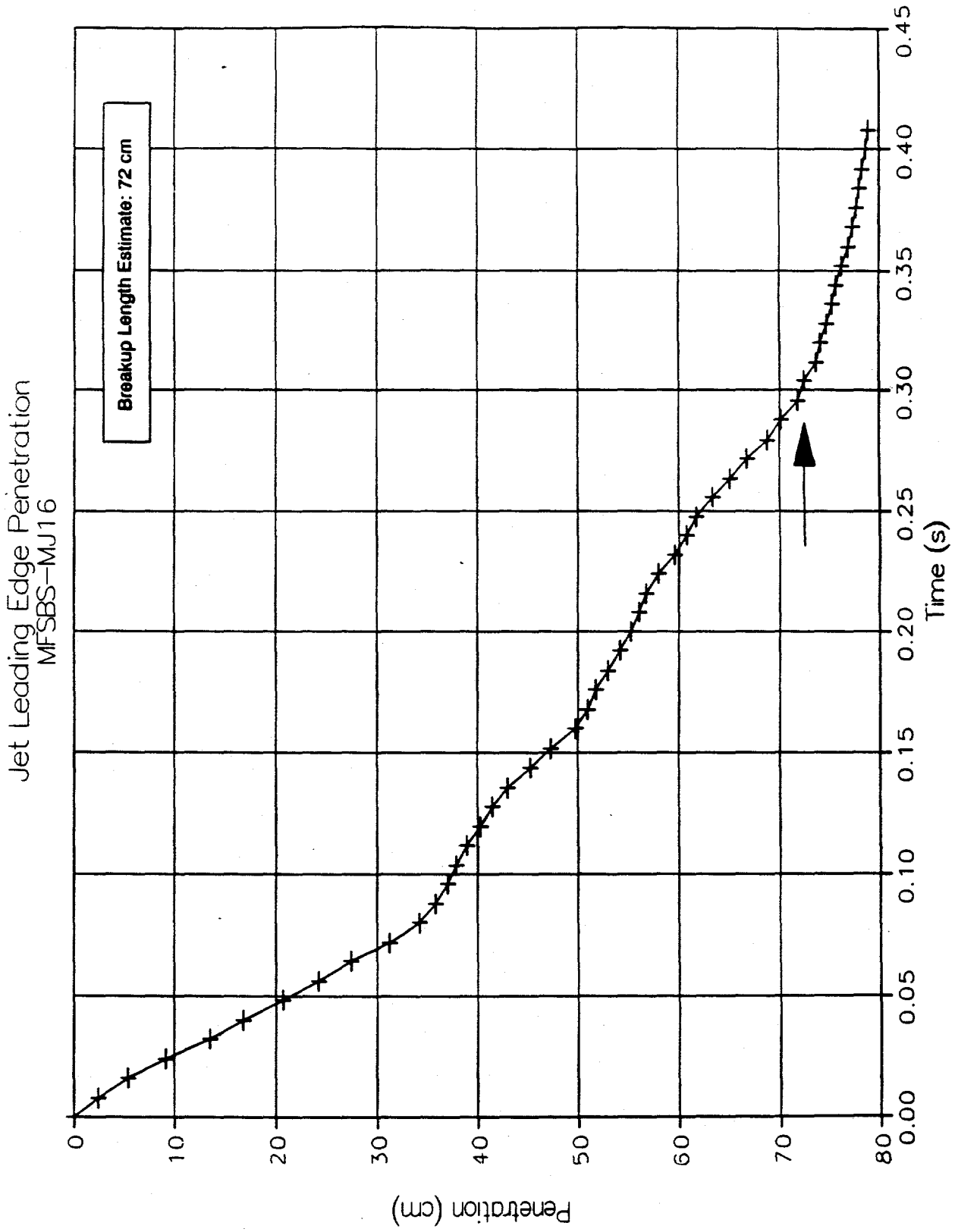
Jet Leading Edge Penetration
MFSBS-MJ16
Breakup Length Estimate: 72 cm
Penetration (cm)
0
10
20
30
40
50
60
70
80
Time (s)
0.00
0.05
0.10
0.15
0.20
0.25
0.30
0.35
0.40
0.45

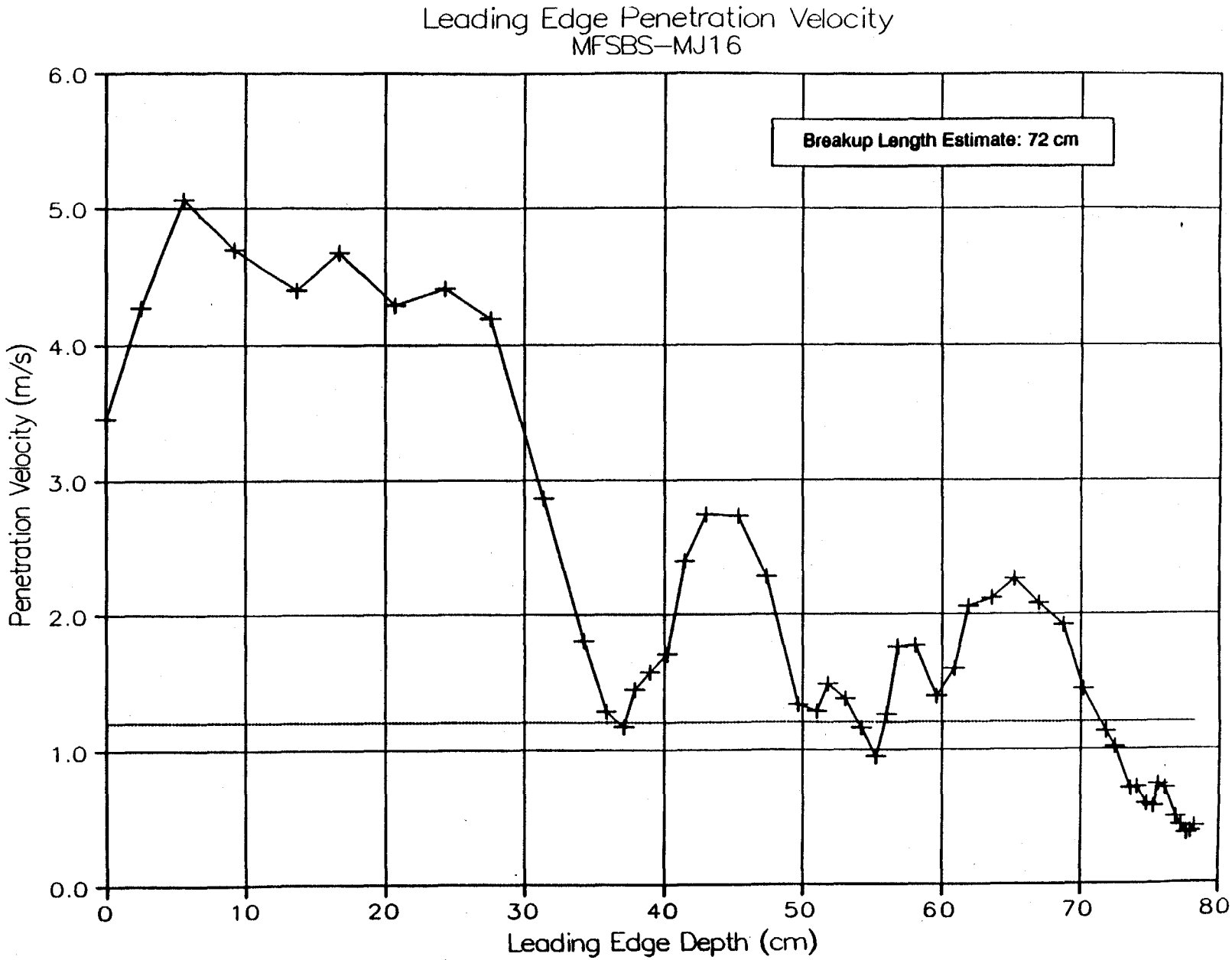
Leading Edge Penetration Velocity
MFSBS–MJ16
Breakup Length Estimate: 72 cm
Penetration Velocity (m/s)
Leading Edge Depth (cm)
6.0
5.0
4.0
3.0
2.0
1.0
0.0
0
10
20
30
40
50
60
70
80

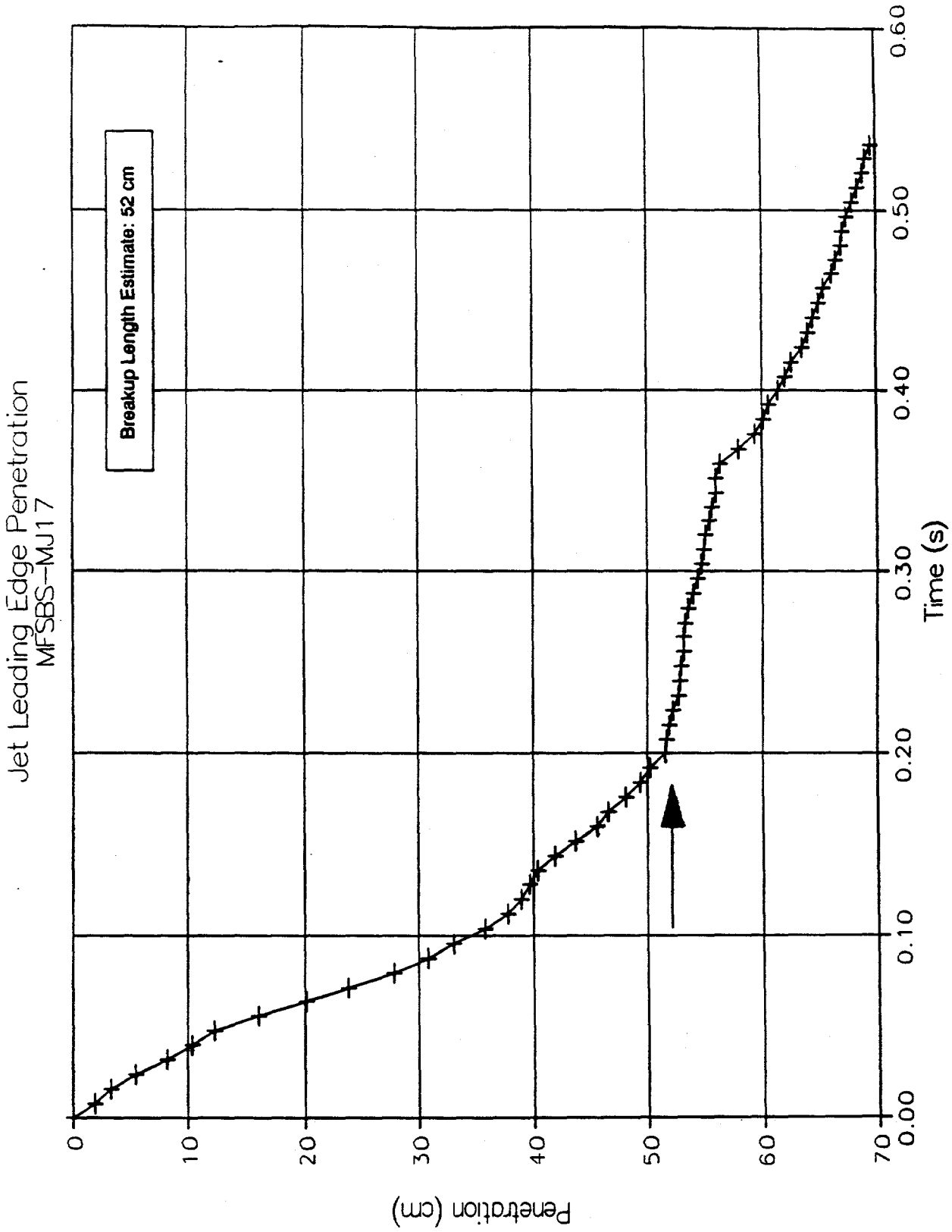
Jet Leading Edge Penetration
MFSBS-MJ17
Breakup Length Estimate: 52 cm
Penetration (cm)
0
10
20
30
40
50
60
70
Time (s)
0.00
0.10
0.20
0.30
0.40
0.50
0.60

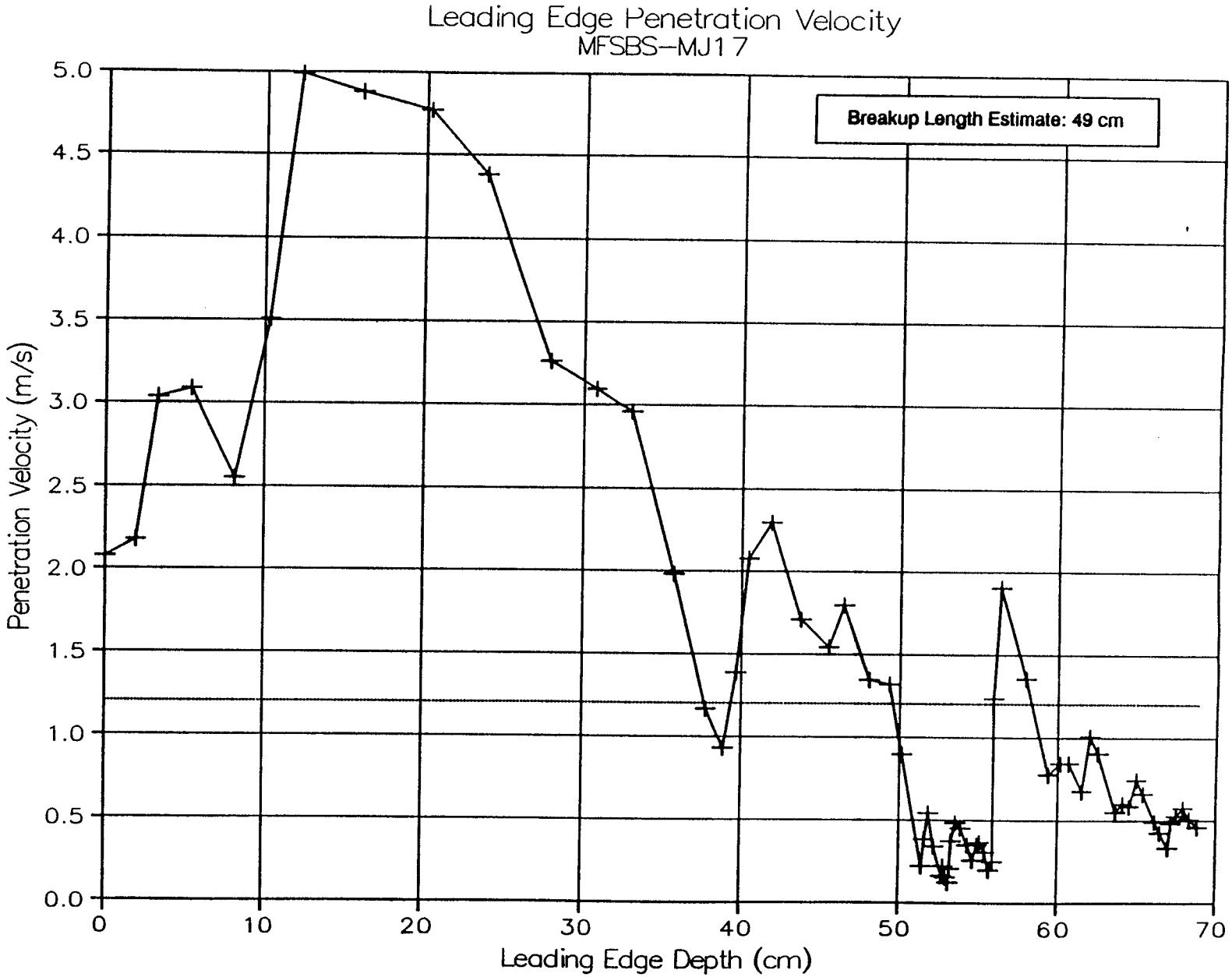
Leading Edge Penetration Velocity
MFSBS–MJ17
Breakup Length Estimate: 49 cm
Penetration Velocity (m/s)
Leading Edge Depth (cm)
5.0
4.5
4.0
3.5
3.0
2.5
2.0
1.5
1.0
0.5
0.0
0
10
20
30
40
50
60
70